Design and Application of Homogeneously Mixed Oxide Composites in Nano-level

By

Hien Thi Thu Nguyen

Student ID Number: 1206003

A dissertation submit to the
Engineering Course, Department of Engineering,
Graduate School of Engineering,
Kochi University of Technology,
Kochi, Japan

for the degree of
Doctor of Philosophy

Assessment Committee:

Supervisor**:** Prof. Kazuya Kobiro
Co-Supervisor: Prof. Ryuichi Sugimoto
Co-Supervisor: Prof. Nagatoshi Nishiwaki
Committee Member: Prof. Hisao Makino
Committee Member: Associate Prof. Masataka Ohtani

March, 2019

ABSTRACT

Homogeneously mixed SiO_2–TiO_2 nanoparticle (NP) assemblies with or without surface modification by *n*-octyl groups were successfully synthesized through a simple, rapid, one-pot, and single-step solvothermal approach. The composite NP assemblies bearing a higher-ordered hollow spherical morphology are synthesized by the reactions of precursor solutions consisting of $Si(OEt)_4$ or *n*-octyl-$Si(OMe)_3$, $Ti(O^iPr)_4$, and *o*-phthalic acid in methanol. An addition of acetic acid or formic acid is needed for yielding the homogeneously mixed SiO_2–TiO_2 NP assemblies with hollow spherical morphology and a high content of Si. Atomic ratios of Si:Ti in the SiO_2–TiO_2 NP composites were easily controlled by adjusting the mole ratio of $Si(OEt)_4$:$Ti(O^iPr)_4$. TiO_2 NPs exhibited a good dispersion in a polar solvent (methanol), likewise a common case, while the *n*-octyl-modified SiO_2–TiO_2 NP composites showed a reversed phenomenon, revealing the change of hydrophobic-lipophilic balance of modified SiO_2–TiO_2 NP assemblies. Thus, the surface of the SiO_2–TiO_2 NP assemblies with hollow spherical morphology was modified directly by *n*-octyl groups through the one-pot and single-step solvothermal approach.

Another homogeneously mixed SiO_2 composites with CeO_2 at nano-level were also fabricated by a similar technique for preparing the SiO_2–TiO_2 NP composites. However, in this case, the SiO_2–CeO_2 NP composites were yielded by the reaction of the precursor solutions of $Si(OEt)_4$ and $Ce(NO_3)_3 \cdot 6H_2O$ in methanol in the presence of *N*,*N*,*N*',*N*'-tetramethylethylenediamine as an additive instead of the acid catalyst. Likewise the synthesis of SiO_2–CeO_2 NP composites, the content of SiO_2 in the NP composites was freely controllable by changing the mole fraction of $Si(OEt)_4$ in the range of 0 to 0.5 in the precursor solutions. Notably, the size of the CeO_2 primary NPs decreased and the specific surface areas of the SiO_2–CeO_2 NP composites significantly increased in proportion to SiO_2 content in the SiO_2–

CeO_2 NP composites. For SiO_2–CeO_2 NP composites yielded from the solution with an equimolar amount of $Si(OEt)_4$:$Ce(NO_3)_3 \cdot 6H_2O$ precursors, the surface area of the composite was over 300 m^2/g. In particular, as expected by mixing the SiO_2 with CeO_2, the SiO_2–CeO_2 NP assemblies exhibited a high heat tolerance through the retention of the small size of CeO_2 crystallites as well as the large specific surface areas, even after calcination at 850 ºC for 3 h or at 700 ºC for 72 h in air.

Taking advantages of high heat tolerance, large specific surface area, and rough surface morphology created by agglomeration of fine primary particles, the prepared CeO_2 aggregates, SiO_2–CeO_2 and TiO_2–CeO_2 nanocomposites are applied to sintering-resistant catalyst supports for highly exothermic reactions. Well-dispersed Ru metal catalysts are deposited on the support surfaces by the precipitation-deposition method. The methanation of CO_2 by H_2, a highly exothermic reaction, is selected as a probe reaction to confirm the sintering-resistant ability of those prepared supports. As expected, low-temperature (150−200 °C) activity of the Ru catalysts on the prepared CeO_2 aggregate and TiO_2–CeO_2 composite yielding CH_4 are better than those on a commercial CeO_2 aggregate. Moreover, long-term stability (400 °C, 24 h and 50−300 °C, 10 cycles) of the catalysts on those prepared supports are also achieved.

TABLE OF CONTENTS

LIST OF TABLES AND FIGURES

LIST OF TABLES

LIST OF FIGURES

LIST OF SCHEMES

CHAPTER I.

General Introduction

1.1. Mixed oxide nanocomposites

Nanometer-sized oxides including single metal oxides and their mixed oxides have been investigated extensively in academic and industrial researches since they exhibit many unique and valuable properties, for expample, large specific surface area, as compared to macro-sized ones. Particularly, the noticeable size-induced effect on the properties such as magnetic, optical, and electronic properties of the nanomaterials is a key factor in the development of the advanced materials. Accordingly, the use of metal oxide nanomaterials has been increasing considerably in most important fields such as biology, medicine, and material science.[1,2]

In the family of the nanostructured oxides, mixed oxides with two or more oxides are the attractive materials constituting extensive researches, especially in the field of catalysis.[3,4] Despite possessing many valuable properties, some critical issues of the single metal oxide nanomaterials still remain due to their poor stability or insufficient chemical and catalytic activity for special applications that require combined properties of several oxides. By mixing the mono-components at a nano level, their synergetic effects are highly expected to solve these drawbacks as well as to enhance properties such as magnetic, electronic, and chemical properties of the resulting mixed materials.[5] For example, changed lattice parameters, surface defects, and redox properties of mixed oxides differed from single-metal oxides can lead to improvement in chemical and catalytic activity of the mixed oxide. Property changes of different mixed oxides, however, are different depending on their crystal structure and chemical compositions. Depending on combinations of several oxides, the composite

nanomaterials with different physical, chemical, and catalytic properties can be achieved. On the other hand, the control over nanostructure distribution and chemical composition, which are determined by synthetic methods, is one of the most critical concerns of the mixed oxide nanomaterials due to its considerable impacts on properties of resulting materials. For that reason, a number of appropriate synthetic routes for reproducible preparation of mixed oxides with controllable compositions have been studied intensively. However, there is still room for more facile and effective synthetic approaches towards controlled mixed oxides.

As one of the most promising metal oxides in industrial applications, a number of researches have studied titania (TiO_2) as a pigment in painting industry; photo-catalyst, self-cleaning, and anti-biofouling materials in environmental purifications; and inorganic filler in cosmetic and nanocomposites,[6,7] where the surface properties such as hydrophilic-lipophilic balance (HLB) are so important. In those cases, surface hydrophobicity (lipophilicity) of TiO_2 is necessary to enhance the dispersibility of TiO_2 in organic media, especially in non-polar ones. Unfortunately, TiO_2 prepared by the chemical methods commonly exhibits a hydrophilic property which results in its weak interaction with organic media. As a consequence, TiO_2 tends to be agglomerated in organic media instead of good dispersion, leading to negative impacts on properties of materials for those applications. Thus, the control of surface properties of TiO_2 is required in order to prevent aggregation of TiO_2. Taking this issue in consideration, the surface functionalization, by which the surface properties are controlled, is considered as a simple and useful way enabling TiO_2 to turn its HLB property.[8] Commonly, conventional routes for surface modification of TiO_2 nanoparticles (NPs) are followed by two-steps involving synthesis of TiO_2 particles and post-functionalization process. In situ surface modification during synthesis of metal oxide particles should be a more attractive route to prepare functionalized TiO_2 NPs due to its simplified reaction process.

Another interesting metal oxide is ceria (CeO_2) which is a valuable rare earth oxide in a variety of applications in the fields of catalysis and material science, etc. Importantly, one of the most interesting properties of CeO_2 nanomaterial is its redox change between the coexisted Ce^{4+} and Ce^{3+} oxidation states in the structure associated with the generation of oxygen vacancies, referred to as oxygen storage capacity.[9,10] By these means, the CeO_2 nanomaterial is a key component in catalytic applications, for example, reforming processes, water-gas shift reaction, and thermochemical water splitting.[11] Notably, depending on the preparation methods, the content of oxygen vacancies and proportion of Ce^{3+}/Ce^{4+} in the structure of CeO_2 can change, leading to different catalytic activities.[12] Accordingly, appropriate synthetic strategies allow controlling the catalytic activity of CeO_2 nanomaterial. Although CeO_2 possesses many advantages, one of its issues is thermal sintering leading to its limited uses for high-temperature processes. As a consequence of its poor heat tolerance, more agglomeration and loss of surface area caused by the migration of CeO_2 are the main reason for CeO_2 activity loss. In order to overcome the critical issues, CeO_2 nanocomposites with other oxide(s) are an effective solution.

Since silica (SiO_2) is one of the promising oxide candidates to be mixed with TiO_2 and CeO_2, a number of researches on SiO_2-based mixed oxides have been carried out and still are intensive in progress. Due to many desired properties of SiO_2, for example, high heat tolerance, high durability, large specific surface area, good mechanical properties, and biocompatibility,[13,14] SiO_2 is highly expected to enhance the properties of TiO_2 and CeO_2 when they are mixed at nano-level. One of the great advantages of SiO_2-based materials is surface functionalization using silane coupling reagents with organo-functional groups.[15] Commonly, silane coupling reagents with an organo-functional group and three hydrolyzable groups are able to form a bridge between organic media and inorganic particles, according to improved dispersibility of metal oxide particles in the organic media. Indeed, the functional

end-groups, for example, alkyl, amino, and carboxylic groups introduced into the particle surface allow the metal oxide NPs to modulate their interactions with organic media.[16,17] Thus, the targeted multifunctional materials with the controlled surface chemistry can be designed.

In spite of numerous attractive advantages of the mixed SiO_2 nanocomposites, these nanocomposites are relatively difficult to prepare due to different hydrolysis rates of silane precursors and other metal oxide precursors in reaction solutions and different crystal structure of SiO_2 and other oxides.[18] Consequently, it is common to obtain the SiO_2 mixed oxides with segregations of the corresponding individual components instead of homogeneous ones through conventional synthesis methods. Some other approaches such as sol-gel and hydrothermal methods are found to be more effective to create homogeneously mixed SiO_2-based composites, their synthetic routes, however, require multi-step pathways and/or long-time reactions.[19–21] Thus, the development of simply synthetic approaches, by which the different hydrolysis processes of the silane reagents and other metal precursors are controlled, remains importantly towards yielding the designed SiO_2-based materials with homogeneously mixed levels.

1.2. Synthetic approaches to metal oxide nanomaterials

The properties of the nano-sized metal oxides are determined by their particle shape, structural morphology, particle size, crystallinity, and chemical compositions, etc. On the other hand, these mentioned factors mainly depend on the preparation processes of the materials. Consequently, the synthetic methods play a key role to control the resulting nanomaterials. To prepare well-controlled metal oxide nanomaterials, a number of studies based on chemical and physical synthetic strategies have been performed. In numerous established synthetic methods yielding metal oxide NPs, for example, co-precipitation method, sol-gel method,

microemulsion method, solvothermal method, and hydrothermal method (Figure 1.1),[22,23] the solvothermal method is one of the most effective synthetic approaches to fabricate metal oxide and mixed oxide nanomaterials with a variety of morphologies. According to a prototype solvothermal preparation, the precursor solution consisting of metal oxide precursors and additives in an appropriate solvent is typically treated at an elevated temperature in a pressurized vessel.[23]

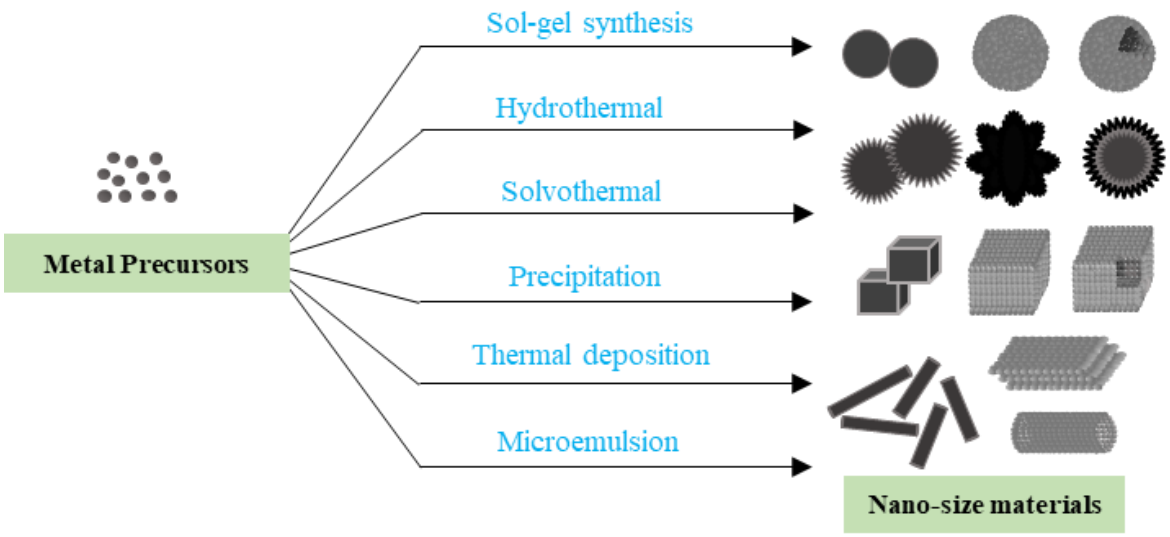

Figure 1.1. Several synthetic methods for creating the nanomaterial.

In comparison with the aqueous-solution routes in which the resulting materials are dramatically influenced by fast hydrolysis processes of precursors and initial pH of the medium, the solvothermal routes in non-aqueous media are easier to control the growth of the particles.[6] For example, the required water for hydrolysis process can be slowly generated during solvothermal reactions from condensation of organic compounds, for example, an esterification of a carboxylic acid with an alcohol, leading to a controlled hydrolysis process. Moreover, it is reported that the organic additives and non-aqueous media can play manifold roles as oxygen supplying sources, capping agents, and/or crystal growth stabilizers driving the nucleation and the crystal growth of particles, accordingly the final NPs with controlled

morphology, high purity, and high crystallinity can be achieved.[24,25] Besides the effects of the chemical factors, the reaction parameters including reaction temperature, reaction time, and heating rate also affect the solubility of the reactants, chemical diffusion, reactivity, and the stability of the intermediate species. By those controlled processes, the targeted nanomaterials can be created in well-defined morphology. An appropriate combination of solvents and additives and a control of reaction temperature, reaction time, and heating rate of solvothermal reactions are extremely important to obtain the desired materials. However, due to the long reaction time of conventional solvothermal routes, which commonly lasts from several hours to several days, much simple solvothermal procedures to yield well-controlled metal oxide and mixed oxide nanomaterials are still required.

1.3. A one-pot and single-step solvothermal approach to metal oxide nanomaterials

In connection with solvothermal synthesis, Wang et al. developed a facile one-pot and single-step strategy to fabricate metal oxide NP assemblies with solid or hollow spherical morphologies, named as **m**icro/**m**eso-porously **a**rchitected **r**oundly **i**ntegrated **m**etal **o**xides (MARIMOs). The approach was applied first to afford TiO_2 NP assemblies through the reaction of the precursor solution of titanium alkoxide and phthalic acid in methanol at 300 °C for 10 minutes.[26]. As a result, the hollow spheres of the crystallized anatase TiO_2 NP assemblies were constructed in a narrow size distribution. The assembly of fine TiO_2 primary particles ca. 5 nm served an ultrafine nano convex/concave surface resulting in a large surface area over 200 m^2/g and even reaching 400 m^2/g. The TiO_2 NP size was controlled by adjusting the reaction temperature while changing the heating rate of the reaction resulted in different shell thickness of the hollow structures.[27] Moreover, the organic additive added to the precursor solution played a critical role in the construction of the TiO_2 structure to control the

morphology of the TiO_2 assemblies.[28] This one-pot and single-step solvothermal approach with a great advantage of short reaction time and easy preparation process is considerably simpler to obtain the controlled nanomaterials than conventional solvothermal routes, where the reactions commonly take place for a long time ranging from several hours to several days.

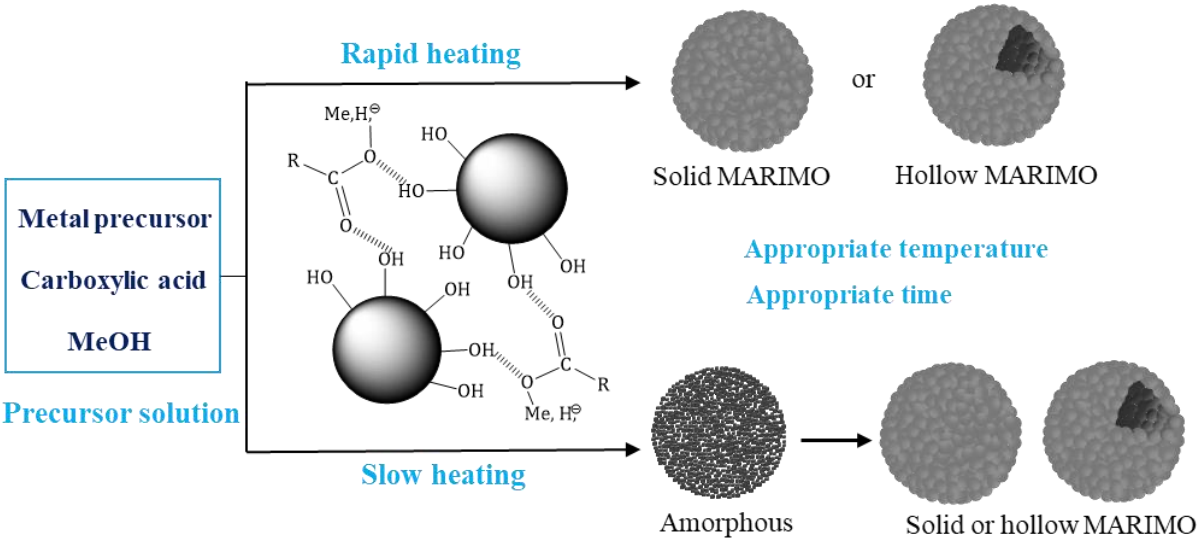

Figure 1.2. A proposed mechanism for the formation of solid or hollow TiO_2 particles in the presence of carboxylic acid.[28]

In addition to the solvothermal preparation of TiO_2 material, morphology control of TiO_2 is also considered in expectation of its innovative applications.[6] Interestingly, the morphology of TiO_2 is adjustable by altering the additives added (Figure 1.3). Indeed, the use of phthalic acid as an additive resulted in the hollow spherical TiO_2 NP assemblies, while TiO_2 assemblies with a cheek-brush morphology were formed by using dimethyl phthalate instead.[26,29] It is suggested that the possible co-ordinations between metal oxide precursors and organic additives could be involved in orienting the nucleation and growth of the TiO_2 NPs. Moreover, solid TiO_2 spheres instead of the hollow ones obtained either by replacing phthalic acid by formic acid in the precursor solutions or by adjusting heating rates.

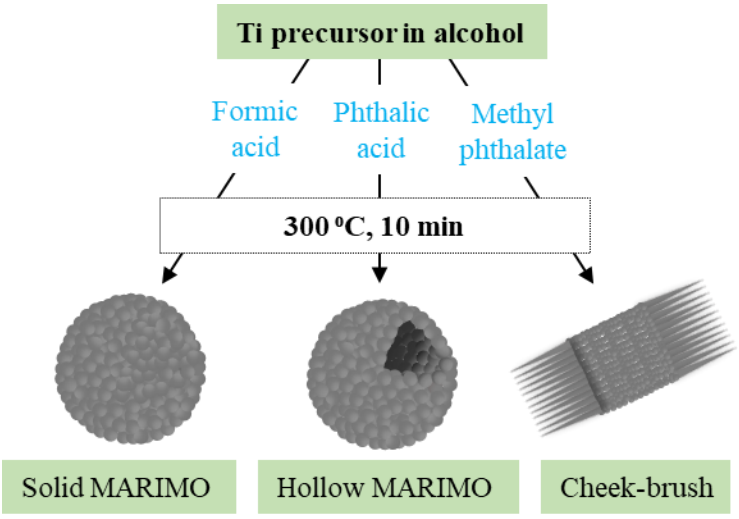

Figure 1.3. Morphological control of TiO_2 NP assemblies by using different additives.

The synthetic approach was quite versatile yielding other metal oxides such as SiO_2, ZrO_2, CeO_2, and ZnO NP assemblies under similar solvothermal conditions in short reaction time. In particular, preparations of oxide composites, for example, Al_2O_3–TiO_2, ZnO–TiO_2, and ZrO_2–CeO_2 with high homogeneity and controlled chemical compositions also were succeeded.[28,30,31] With great advantages of the simple preparation procedure such as the short reaction time, the well-controlled products in morphology, composition, crystallinity, the one-pot, and single-step solvothermal approach is versatile in a wide range of the advanced materials. Therefore, it is a suitable approach aiming at yielding homogeneous SiO_2-based nanocomposites with control of chemical compositions.

1.4. Potential applications of solvothermally prepared nanomaterials in catalysis

A number of studies have been focused on utilizing various kinds of metal oxide and mixed oxide nanomaterials for catalytic processes due to the excellent catalytic activity of these materials.[3,32] In the catalytic systems, active metal NPs dispersed on the oxides or mixed

oxide supports are widely used for a wide variety of reactions, such as biomass conversion, hydrogenation, oxidation, transesterification, and others. However, as a critical issue of the catalysts, a loss of catalytic activity of the catalysts over time occurs certainly for most catalytic processes, which is commonly caused by catalyst poisoning, fouling, thermal degradation, vapor compound formation accompanied by transport, vapor-solid and/or solid-solid reactions, and attrition/crushing, according to catalyst degradation.[33] In order to keep catalysts being efficient and stable for a long time use, prevention of activity loss of catalyst over time is extremely important.

Among those reasons of catalyst activity loss/deactivation, thermal sintering is a critical issue, especially in high-temperature applications. Indeed, the active particles and oxide supports tend to migrate to form larger agglomerates during their catalytic operation, which followed by loss of surface area and catalytic efficiency as a result of the sintering.[34,35] In particular, the sintering of the catalyst becomes more serious as the process temperature increases. For this reason, several anti-sintering strategies, both chemical and physical ones, such as alloying, encapsulation, or ligand-assisted pinning have been investigated in order to prevent the sintering of the supported catalysts (Figure 1.4) .[35] These researches, however, are still in progress. Considering the long-term usability of the supported catalysts, not only the catalytic activity and tolerance of the active metal catalysts but those of the oxide supports should be considered as important factors.

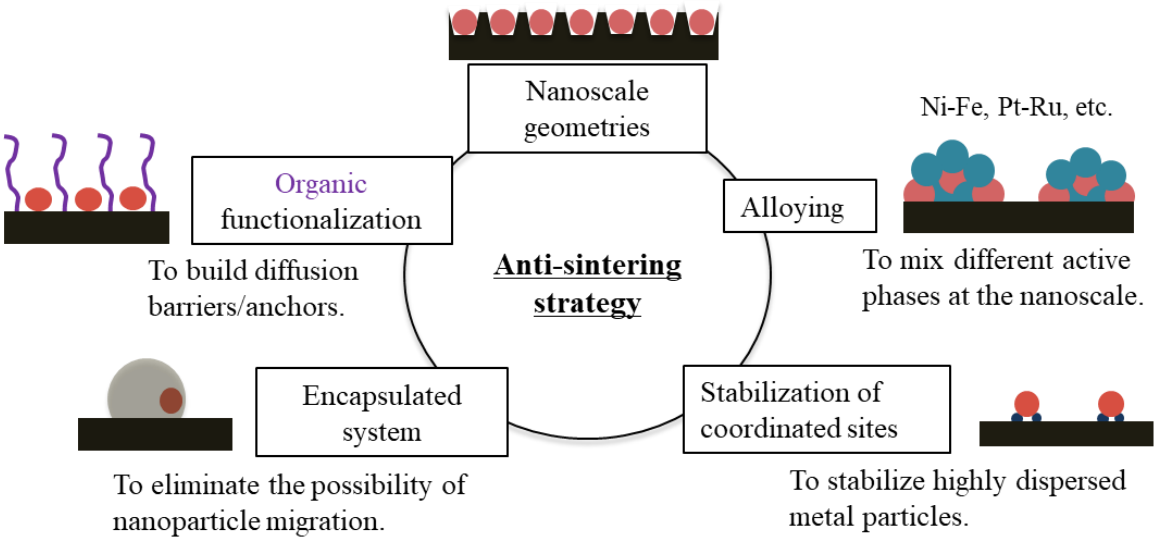

Figure 1.4. Several anti-sintering strategies for supported catalysts.

As previously mentioned, the NP assemblies prepared by the one-pot and single-step solvothermal approach presented the advantages of large surface area and rough surface morphology constructed by very fine primary particles. However, these advantages are yet to be taken well. It is supposed that those solvothermally prepared nanomaterials could be applied as potential catalyst supports in expectation of good dispersion of metal catalysts and sintering prevention of the supported catalyst. Indeed, the nanostructured materials with a rough surface and large surface area could facilitate dispersion of the metal catalysts as well as impede its agglomeration. In addition, the use of high heat-tolerant oxide supports would prevent the collapse of the catalyst support. By those means, well-dispersed metal particles deposited on the support surface could be kept stable through catalytic processes. Taking these above-mentioned issues in consideration, the solvothermally prepared NP assemblies would be excellent candidates to prevent sintering of the supported catalyst.

Dissertation Scope and Outline

For those above-addressed issues, the present study focuses on the fabrication of homogeneously mixed NP assemblies of SiO_2–TiO_2 and SiO_2–CeO_2 with adjustable composition ratios by the one-pot and single-step solvothermal approach. Mono-component TiO_2 and CeO_2 are selected as candidates to be mixed with SiO_2 to yield nanocomposites in expectation of enhanced properties such as adsorption ability, surface area, heat tolerance, and controlled HLB. By mean of the solvothermal reactions, the difficult combination of SiO_2 with other oxides due to different hydrolysis rates of the precursors and different crystal structures of SiO_2 and other oxides can be controlled. The reaction conditions are optimized appropriately to obtain the nanocomposites. The detailed synthesis procedures and discussions are presented in Chapters II and III for SiO_2–TiO_2 and SiO_2–CeO_2, respectively. Similarly, another composite of TiO_2–CeO_2 is also prepared under similar conditions.

Taking advantages of enhanced heat tolerance, huge specific surface area, and rough surface morphology created by agglomeration of very fine primary particles, the synthesized materials including CeO_2, SiO_2–CeO_2, and TiO_2–CeO_2 are applied as the catalyst supports for Ru catalyst in expectation of sintering-resistant ability. An extremely exothermic reaction of methanation of CO_2 by H_2 is selected as a probe reaction to confirm the catalytic efficiency and ability against sintering of those catalysts. Those results are fully shown and discussed in Chapter IV.

Summary of achievements, general conclusion, and outlooks for future studies are given in Chapter V. In addition, the Appendices of additional information, which are not shown in the main Chapter, are presented in the last part of Dissertation.

Reference

[1] M. Fernández-Garcia, A. Martınez-Arias, J. C. Hanson, J. A. Rodriguez, Nanostructured oxides in chemistry: characterization and properties, *Chem. Rev.* **2004**, *104*, 4063–4104.

[2] M. Fernández-Garcia, J. A. Rodriguez, in *Introduction the World of Oxide Nanomaterials* (Eds.: M. Fernández-Garcia, J. A. Rodriguez), Chapter 1, John Wiley & Sons, Inc., **2007,** pp. 1–59.

[3] M. Gawande, R. Pandey, R. Jayaram, Role of mixed metal oxides in catalysis science-versatile applications in organic synthesis, *Catal. Sci. Technol.* **2012**, *2*, 1113–1125.

[4] M. Dahl, Y. Liu, Y. Yin, Composite titanium dioxide nanomaterials, *Chem. Rev.* **2013**, *114*, 9853–9889.

[5] J. Wang, J. Wen, M. Shen, Effect of interaction between $Ce_{0.7}Zr_{0.3}O_2$ and Al_2O_3 on structural characteristics, thermal stability, and oxygen storage capacity, *J. Phys. Chem. C* **2008**, *112*, 5113–5122.

[6] D. Fattakhova-Rohlfing, A. Zaleska, T. Bein, Three-dimensional titanium dioxide nanomaterials, *Chem. Rev.* **2014**, *114*, 9487–9558.

[7] S. Peng, B. Dang, Y. Zhou, J. Hu, J. He, Functionalized TiO_2 nanoparticles tune the aggregation structure and trapping property of polyethylene nanocomposites, *J. Phys. Chem. C* **2016**, *120*, 24754−24761.

[8] S. Takahashi, S. Hotta, A. Watanabe, N. Idota, K. Matsukawa, Y. Sugahara, Modification of tio_2 nanoparticles with oleyl phosphate via phase transfer in the toluene−water system and application of modified nanoparticles to cyclo-olefin-polymer-based organic−inorganic hybrid films exhibiting high refractive indices, *Appl. Mater. Interfaces* **2017**, *9*, 1907–1912.

[9] T. Montini, M. Melchionna, M. Monai, P. Fornasiero, Fundamentals and catalytic

applications of ceo$_2$-based materials, *Chem. Rev.* **2016**, *116*, 5987–6041.

[10] S. Dutta, M. Seehra, Y. Shi, E. M. Eyring, R. Ernst, Concentration of Ce^{3+} and oxygen vacancies in cerium oxide nanoparticles, *Chem. Mater.* **2006**, *18*, 5144–5146.

[11] C. Sun, H. Li, L. Chen, Nanostructured ceria-based materials: synthesis, properties, and applications, *Energy Environ. Sci.* **2012**, *5*, 8475–8505.

[12] A. Trovarelli, J. Llorca, Ceria catalysts at nanoscale: how do crystal shapes shape catalysis?, *ACS Catal.* **2017**, *7*, 4716–4735.

[13] D. Douroumis, I. Onyesom, M. Maniruzzaman, J. Mitchell, Mesoporous silica nanoparticles in nanotechnology, *Crit. Rev. Biotechnol.* **2013**, *33*, 229–245.

[14] A. Liberman, N. Mendez, W. Trogler, A. Kummel, Synthesis and surface functionalization of silica nanoparticles for nanomedicine, *Surf. Sci. Rep.* **2014**, *69*, 132–158.

[15] S. Kango, S. Kalia, A. Celli, J. Njuguna, Y. Habibi, R. Kumar, Surface modification of inorganic nanoparticles for development of organic-inorganic nanocomposites - a review, *Prog. Polym. Sci.* **2013**, *38*, 1232–1261.

[16] J. Huang, S. Li, M. Ge, L. Wang, T. Xing, G. Chen, X. Liu, S. Deyab, K. Zhang, T. Chen, Y. Lai, Robust superhydrophobic TiO_2@fabrics for UV shielding, self-cleaning and oil-water separation, *J. Mater. Chem. A* **2015**, *3*, 2825–2832.

[17] R. Palma, S. Peeters, M. Bael, H. Rul, K. Bonroy, W. Laureyn, J. Mullens, G. Borghs, G. Maes, Silane Ligand Exchange to Make Hydrophobic Superparamagnetic Nanoparticles Water-Dispersible, *Chem. Mater.* **2007**, *19*, 1821–1831.

[18] U. Schubert, in *The Sol-Gel Handbook: Synthesis, Characterization, and Applications, Vol. 1* (Eds.: D. Levy, M. Zayats), Wiley-VCH, Weinheim, **2015**, pp. 1–27.

[19] G. Jeong, H. Lee, J. Kang, H. Lee, C. Kim, J. Lee, J. Kim, S. Kim, ZrO_2−SiO_2 Nanosheets with Ultrasmall WO_3 Nanoparticles and Their Enhanced Pseudocapacitance and Stability, *ACS Appl. Mater. Interfaces* **2014**, *6*, 20171–20178.

[20] K. Akurati, R. Dittmann, A. Vital, U. Klotz, P. Hug, T. Graule, M. Winterer, Silica-based composite and mixed-oxide nanoparticles from atmospheric pressure flame synthesis, *J. Nanopart. Res.* **2006**, *8*, 379–393.

[21] F. Tang, L. Li, D. Chen, Mesoporous silica nanoparticles: synthesis, biocompatibility and drug delivery, *Adv. Mater.* **2012**, *24*, 1504–1534.

[22] P. Cousin, R. Ross, Preparation of mixed oxides: a review, *Mater. Sci. Eng. A*, **1990**, *130*, 119–125.

[23] B. Rao, D. Mukherjee, B. Reddy, in *Nanostructures for Novel Therapy: Synthesis, Characterization and Applications* (Eds.: D. Ficai, A. M. Grumezescu), Elsevier, **2017**, pp. 1–36.

[24] M. Niederberger, G. Garnweitner, Organic reaction pathways in the nonaqueous synthesis of metal oxide nanoparticles, *Chem. Eur. J.* **2006**, *12*, 7282–7302.

[25] R. Deshmukh, M. Niederberger, Mechanistic aspects in the formation, growth and surface functionalization of metal oxide nanoparticles in organic solvents, *Chem. Eur.J.* **2017**, *23*, 8542–8570.

[26] P. Wang, K. Kobiro, Synthetic versatility of nanoparticles: A new, rapid, one-pot, single-step synthetic approach to spherical mesoporous (metal) oxide nanoparticles using supercritical alcohols, *Pure Appl. Chem.* **2014**, *86*, 785–800.

[27] P. Wang, K. Kobiro, Ultimately simple one-pot synthesisof spherical mesoporous TiO_2 nanoparticles in supercritical methanol, *Chem. Lett.* **2012**, *41*, 264–266.

[28] P. Wang, K. Ueno, H. Takigawa, K. Kobiro, Versatility of one-pot, single-step synthetic approach for spherical porous (metal) oxide nanoparticles using supercritical alcohols, *J. Supercrit. Fluid* **2013**, *78*, 124–131.

[29] F. Duriyasart, H. Hamauzu, M. Ohtani, K. Kobiro, Three-dimensionally branched titanium dioxide with cheek-brush morphology: synthesis and its application to polymer

composites, *ChemistrySelect* **2016**, *1*, 5121–5128.

[30] E. K. C. Pradeep, T. Habu, H. Tooriyama, M. Ohtani, K. Kobiro, Ultra-simple synthetic approach to the fabrication of CeO_2–ZrO_2 mixed nanoparticles into homogeneous, domain, and core–shell structures in mesoporous spherical morphologies using supercritical alcohols, *J. Supercrit. Fluid* **2015**, *97*, 217–223.

[31] E. K. C. Pradeep, M. Ohtani, K. Kobiro, A simple synthetic approach to Al_2O_3–TiO_2 and ZnO–TiO_2 mesoporous hollow composite assemblies consisting of homogeneously mixed primary particles at the nano level, *Eur. J. Inorg. Chem.* **2015**, *2015*, 5621–5627.

[32] G. Busca, in *Heterogeneous Catalytic Materials Solid State Chemistry, Surface Chemistry and Catalytic Behaviour*, Vol. Chapter 4, Elsevier, Oxford, **2014**, pp. 37–56 .

[33] C. Bartholomew, Mechanisms of catalyst deactivation, *Appl. Catal., A* **2001**, *212*, 17–60.

[34] T. Hansen, A. Delariva, S. Challa, A. Datye, Sintering of catalytic nanoparticles: particle migration or Ostwald ripening, *Acc. Chem. Res.* **2013**, *46*, 1720–1730.

[35] E. Goodman, J. Schwalbe, M. Cargnello, Mechanistic understanding and the rational design of sinter-resistant heterogeneous catalysts, *ACS Catal.* **2017**, *7*, 7156–7173.

CHAPTER II.

One-step Direct Synthesis of SiO_2–TiO_2 Composite Nanoparticle Assemblies with Hollow Spherical Morphologies

2.1. Introduction

TiO_2 is one of the most promising functional materials with a variety of applications in many fields such as solar cells, photovoltaics, and environmental remediation.[1–12] Moreover, TiO_2 NPs are also used in the preparation of nanocomposites in order to enhance the properties of polymeric materials such as optical, mechanical, electrical, and thermal properties.[13–18] Despite their inherent excellent properties, TiO_2 NPs have several drawbacks such as the tendency to agglomerate and poor interaction with organic materials.[5,19] Indeed, in a number of researches studied TiO_2 as a pigment in painting industry; self-cleaning and anti-biofouling material in environmental purifications; and inorganic filler in cosmetic and nanocomposites, surface hydrophobicity (lipophilicity) of TiO_2 is necessary to enhance the dispersibility of TiO_2 in organic media, especially in non-polar ones. Unfortunately, TiO_2 prepared by the chemical methods commonly exhibits a hydrophilic property which results in its poor interaction with organic media. As a consequence, TiO_2 tends to be agglomerated in organic media instead of a good dispersion, leading to the negative impacts on the properties of materials in those applications. However, these problems of TiO_2 material can be overcome by modifying with SiO_2.

Silica–titania (SiO_2–TiO_2) composite NPs are interesting materials because of their remarkable photocatalytic efficiency, durability,[1,20–23] and scaffold layer in perovskite solar cell[24] as compared to those of TiO_2 NPs since SiO_2 increases the mechanical and thermal

stability, adsorption ability, and the specific surface area of the TiO_2 NPs.[1,21] In addition, surface modification of TiO_2 NP assemblies using alkylsilane reagents can easily control the their dispersibility in media.[19,25–28] Commonly, conventional routes for surface modification of TiO_2 NPs are followed by a two-step process involving the synthesis of TiO_2 particles and the post-functionalization process. In situ surface modification during synthesis of metal oxide particles could be a more attractive route to prepare functionalized TiO_2 NPs due to simplified reaction process (Figure 2.1).

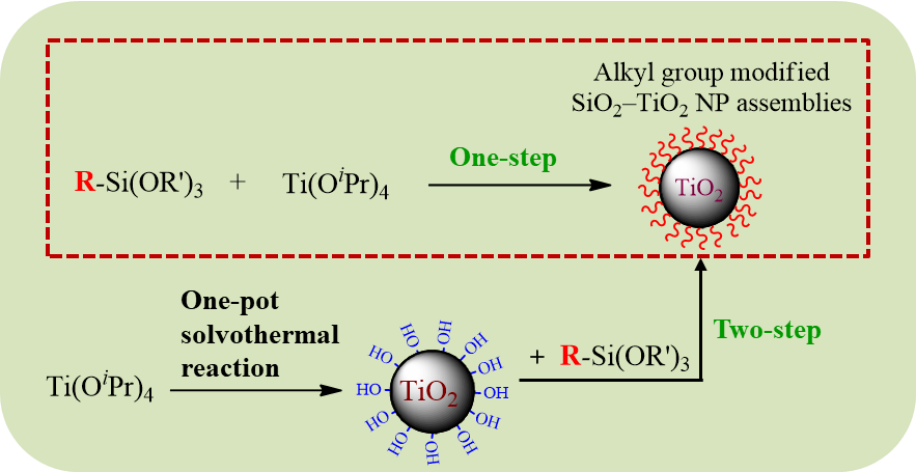

Figure 2.1. Modification routes of TiO_2 NPs.

In spite of numerous attractive advantages of SiO_2 nanocomposites, the homogeneously mixed SiO_2 nanocomposites are relatively difficult to yield due to the different hydrolysis rates of silane precursors and other metal precursors in reaction solutions and different crystal structure of SiO_2 and others. Indeed, the resulting SiO_2 mixed oxides prepared by conventional synthetic methods tend to form as the segregations of the corresponding individual components instead of the homogeneous ones. Some other approaches, for example, sol-gel and hydrothermal methods are more effective to create the homogeneous SiO_2-based composites, their synthetic routes, however, are relatively complicated required multi-step pathways and/or long-time reactions. For example, the synthesis of high-ordered structured

SiO_2-based NP composites commonly required an assistance of the soft/hard templates and a subsequent calcination step. Thus, controlling the hydrolysis processes of the silane reagents and other metal precursors during the synthetic process is a crucial key to achieve the homogeneous SiO_2-based nanocomposites. Moreover, the development of simply synthetic procedures to yield the designed SiO_2-based materials with homogeneous mixing level still remains important.

As mentioned in Chapter I, we have developed the new solvothermal approach to afford metal oxide NP assemblies with solid or hollow spherical morphologies named **m**icro/**m**eso-porously **a**rchitected **r**oundly **i**ntegrated **m**etal **o**xides (MARIMOs).[29–31] Our solvothermal approach is versatile for preparing other oxide NP assemblies such as SiO_2, TiO_2, ZnO, ZrO_2, and CeO_2 and their composites such as TiO_2–ZnO, TiO_2–Al_2O_3, ZrO_2–CeO_2, and In–Ga–Zn oxide as well using a similar technique from precursor solutions consisting of metal alkoxides and/or salts.[30,32] During the solvothermal reaction, the metal oxides were obtained by condensation of metal hydroxides that resulted from the hydrolysis of mixed metal alkoxides or salts. Due to different hydrolysis rate of different metal precursors, the widely different reaction rates of the metal precursors would yield inhomogeneously mixed composite NP assemblies instead of homogeneously mixed ones. However, we succeeded in synthesizing the above-mentioned mixed metal oxide NP assemblies. It is noted that the solvolysis rate of alkoxysilane is slower than that of alkoxytitanium.[33] Thus, our solvothermal approach of using alkoxysilane and alkoxytitanium precursor solutions to yield SiO_2–TiO_2 composite NP assemblies can be anticipated to be ineffective, especially in the case of SiO_2–TiO_2 composite NP assemblies with a higher SiO_2 ratio. Herein, I report a one-pot and single-step solvothermal approach to generate SiO_2–TiO_2 composite NP assemblies with and without alkyl surface modification and bearing a hollow morphology.

2.2. Experimental Section

2.2.1. Materials

Methanol, *o*-phthalic acid, acetic acid, formic acid, titanium tetraisopropoxide, and tetraethyl orthosilicate were supplied by Wako Pure Chemical Industries Co. Ltd. Trimethoxy-*n*-octylsilane was purchased from Tokyo Chemical Industry Co., Ltd. All the reagents were used as received.

2.2.2. Synthesis of MARIMO SiO_2–TiO_2 assemblies

The precursor solutions consisting of $Ti(O^iPr)_4$, $Si(OEt)_4$ or n-$C_8H_{17}Si(OMe)_3$, and *o*-phthalic acid (0.5 mol/L) in methanol were stirred homogeneously. The total concentration of $Ti(O^iPr)_4$ and $Si(OEt)_4$ or n-C_8H_{17}-$Si(OMe)_3$ in methanol (3.5 mL) was 0.1 mol/L. To change the ratio of SiO_2:TiO_2 in the NP composites, the mole ratios of $Si(OEt)_4$:$Ti(O^iPr)_4$ were adjusted correspondingly. The mixed solution was transferred to an SUS-316 stainless steel reactor and sealed by a screw cap equipped with a thermocouple to measure the inside temperature. The reactor was heated up to 300 °C at a heating rate of 5.4 °C/min in an electric oven; the reaction was performed at this temperature for 10 min. Thereafter, the reactor was placed in an ice-water bath to quench the reaction. The obtained white solid products were centrifuged three times at 6600 rpm for 30 min and then dried overnight in a vacuum oven.

2.2.3. Characterization of NPs

Transmission electron microscopy images were taken on a JEOL JEM-2100F microscope. The chemical compositions of the particles were quantified by energy dispersive X-ray spectroscopy using Oxford INCA Energy TEM250 attached to the transmission electron

microscope. The specific surface area of the SiO_2–TiO_2 composite assemblies was calculated based on the nitrogen adsorption-desorption isotherm obtained on a BELSORP-mini II instrument (BEL Japan, Inc). Crystalline structure of the prepared composites were detected by X-Ray diffraction on a Rigaku SmartLab diffractometer with a graphite-monochromated Cu-K_α radiation. Fourier transform infrared spectra were recorded on a JASCO FT-IR-480 Plus spectrometer using the KBr pellet method.

2.3. Results and Discussion

2.3.1. One-pot synthesis of prototype SiO_2–TiO_2 composite NP assemblies

2.3.1a. Synthesis of SiO_2–TiO_2 composite NP assemblies

As a preliminary experiment, our one-pot and one-step approach yielding the MARIMO TiO_2 assemblies[29,32] was applied to the synthesis of prototype SiO_2–TiO_2 composite NP assemblies. The solvothermal reactions of the precursor solutions containing $Si(OEt)_4$, $Ti(O^iPr)_4$, and *o*-phthalic acid in methanol (MeOH) were performed at 300 °C for 10 minutes (Table 2.1 and Scheme 2.1). The reactors was heated at a heating rate of 5 °C/min. For yielding SiO_2–TiO_2 composite NP assemblies, the existence of *o*-phthalic acid and the slow heating are necessary for the fabrication of hollow structure through Ostwald ripening as discussed in a previous work.[32]

Scheme 2.1. Schematic of synthesis of SiO_2–TiO_2 MARIMO NP composite

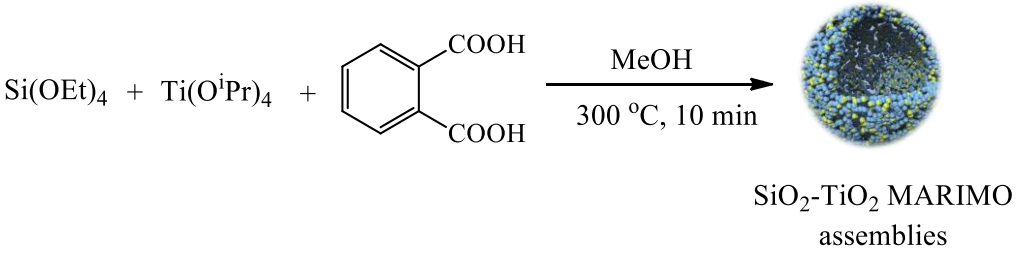

Table 2.1. $Si(OEt)_4$:$Ti(O^iPr)_4$ mole ratio in the precursor solutions and the properties of the formed NP assemblies[a].

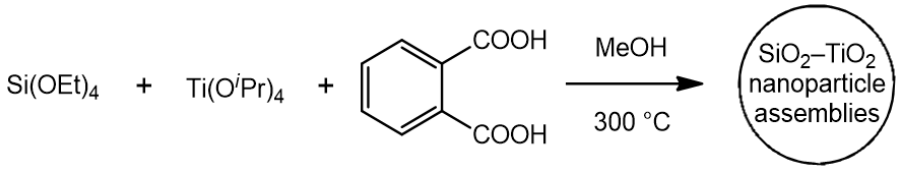

Entry	Precursor solution			SiO_2–TiO_2 composite NP assembly			
	$Si(OEt)_4$ (mol/L)	$Ti(O^iPr)_4$ (mol/L)	Mole fraction of Si[b]	Yield (%)	Atomic % of Si (Si/(Si+Ti)×100)[c]	Specific surface area (m^2/g)	Diameter of assembly (nm)[d]
1	0	0.1	0	89	0	218	700 ± 50
2	0.01	0.09	0.1	98	4.0	276	743 ± 98
3	0.025	0.075	0.25	79	9.1	334	543 ± 83
4	0.05	0.05	0.5	81	33.3	353	602 ± 48
5	0.075	0.025	0.75	40	75	667	1496 ± 288
6	0.1	0	1	trace	100	–[e]	–[f]

[a]Reaction conditions: [*o*-phthalic acid] = 0.5 mol/L, heating rate = 5.4 °C/min, final temperature = 300 °C, and holding time of final temperature = 10 min.

[b]Calculated using formula $Si(OEt)_4/(Si(OEt)_4+Ti(O^iPr)_4)$.

[c]Evaluated by STEM/EDX analysis.

[d]Calculated directly from the TEM images by measuring at least 40 assemblies.

[e]Not measured because of small amount of material.

[f]Agglomerates of nanoparticles.

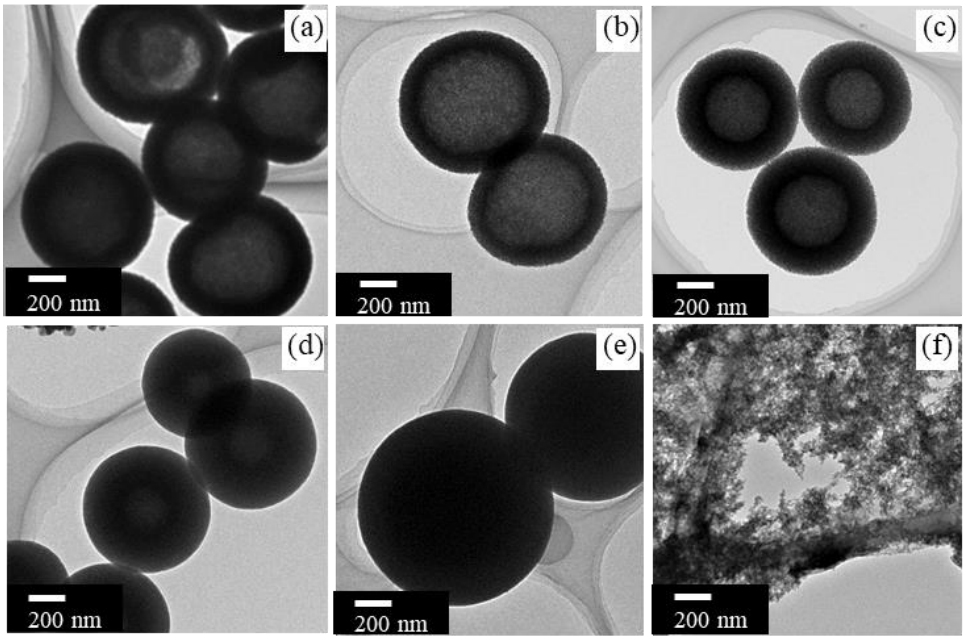

Figure 2.2. TEM images of NP assemblies obtained from precursor solutions with different $Si(OEt)_4/(Si(OEt)_4+Ti(O^iPr)_4)$ mole fractions. (a) 0 (Entry 1 in Table 2.1), (b) 0.1 (Entry 2 in Table 2.1), (c) 0.25 (Entry 3 in Table 2.1), (d) 0.5 (Entry 4 in Table 2.1), (e) 0.75 (Entry 5 in Table 2.1), and (f) 1 (Entry 6 in Table 2.1).

A precursor solution containing an equimolar amount of $Si(OEt)_4$ and $Ti(O^iPr)_4$ yielded NP assemblies with a beautiful hollow spherical morphology as expected (Entry 4 in Table 2.1 and Figure 2.2d). Similar reactions of precursor solutions containing low amounts of $Si(OEt)_4$ also resulted in composite NP assemblies with hollow spherical morphologies (Entries 2 and 3 in Table 2.1 and Figures 2.2b and 2.2c). The TEM images and EDX mappings (Figure 2.3) of the SiO_2–TiO_2 NP assemblies with Si mole fraction of 0.25 (Entry 3 in Table 2.1) confirmed the homogeneous distribution of the obtained composites. However, at higher amounts of $Si(OEt)_4$, a very low product yield was obtained (Entries 5 and 6 in Table 2.1 and Figures 2.2e and 2.2f). In particular, a trace amount of agglomerated SiO_2 NPs was obtained from 100% $Si(OEt)_4$ precursor solution (Entry 6 in Table 2.1 and Figure 2.2f), which could be attributed to the slow hydrolysis rate of $Si(OEt)_4$ at a low reaction temperature of 300 °C.[33] Moreover,

the surface of the obtained composite NP assemblies became smoother (Figures 2.2a-e) and their BET specific surface area and diameters became larger (Entries 1–5 in Table 2.1 and Figures 2.2a–2.2e) with increasing amount of $Si(OEt)_4$ in the precursor solutions.

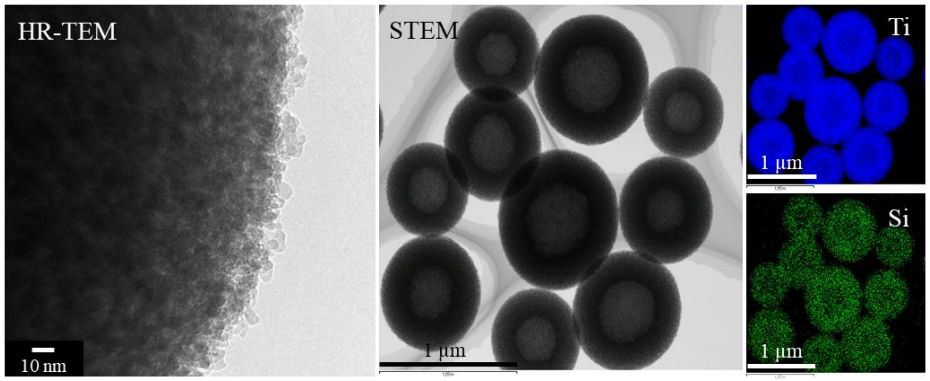

Figure 2.3. HR-TEM image, STEM image, and EDX mappings of SiO_2–TiO_2 NP assemblies obtained from precursor solutions with $Si(OEt)_4/(Si(OEt)_4+Ti(O^iPr)_4)$ mole fraction of 0.25 (Entry 3 in Table 2.1).

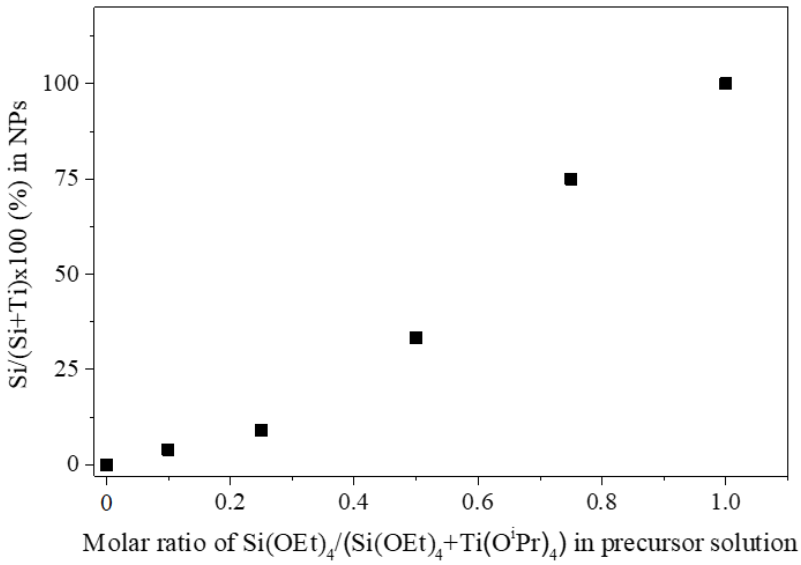

Figure 2.4. The plot of atomic fractions of Si in the SiO_2–TiO_2 composite NP assemblies estimated by EDX against the $Si(OEt)_4/(Si(OEt)_4+Ti(O^iPr)_4)$ mole fractions in the precursor solutions (Table 2.1).

It was noted that an almost linear relationship was observed between the atomic percentage of Si in the obtained composite NP assemblies (agglomerates) and the $Si(OEt)_4$ mole fractions in the precursor solutions (Figure 2.4). This indicates that the Si:Ti ratio in the obtained composite NP assemblies with hollow spherical morphologies can be easily controlled by adjusting the $Si(OEt)_4$:$Ti(O^iPr)_4$ ratio in the corresponding precursor solutions. The X-ray diffraction patterns clearly indicated the existence of anatase TiO_2 nanocrystals in all the NP assemblies (Figure 2.5). The crystalline phase of SiO_2 was not observed in the XRD spectra. However, a broad peak appeared at $2\theta<20$ ° region that corresponded with the amorphous phase of SiO_2.

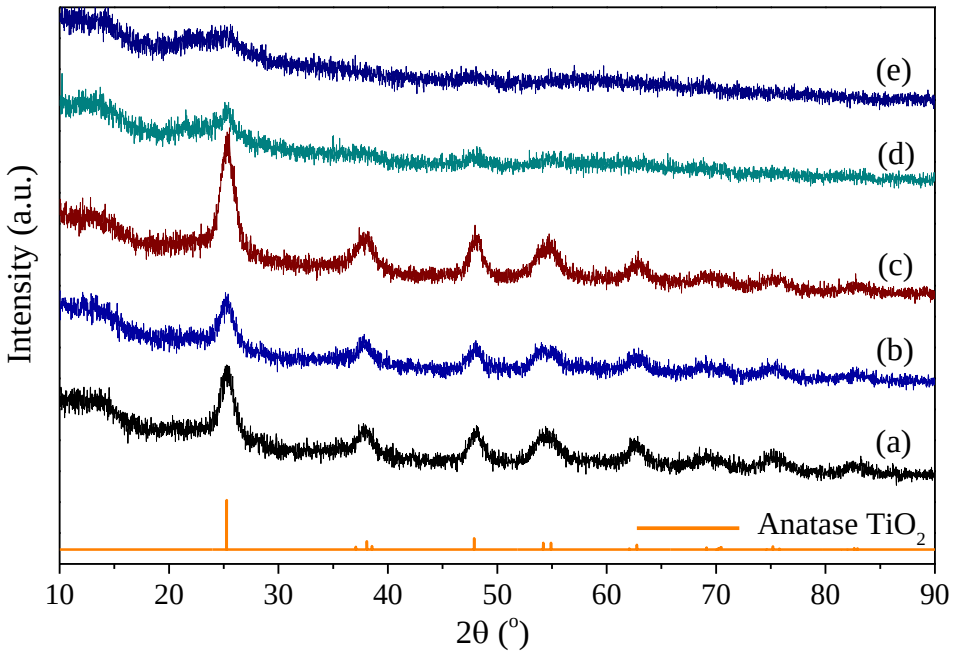

Figure 2.5. XRD patterns of the composite NP assemblies obtained from precursor solutions with different $Si(OEt)_4/(Si(OEt)_4+Ti(O^iPr)_4)$ mole fractions. (a) 0 (Entry 1 in Table 2.1), (b) 0.1 (Entry 2 in Table 2.1), (c) 0.25 (Entry 3 in Table 2.1), (d) 0.5 (Entry 4 in Table 2.1), and (e) 0.75 (Entry 5 in Table 2.1).

2.3.1b. Effect of an addition of a second acid catalyst on the hydrolysis of $Si(OEt)_4$

As discussed in the previous section, the solvothermal treatment of 100% $Si(OEt)_4$ precursor solution resulted in agglomerates of primary SiO_2 NPs (Entry 6 in Table 2.1 and Figure 2.2f) which could relate to the slow hydrolysis rate of $Si(OEt)_4$ under the solvothermal reaction conditions. The concentration of *o*-phthalic acid in the precursor solutions should be increased to accelerate the reaction and to facilitate effective acid-catalyzed hydrolysis of $Si(OEt)_4$. However, in a previous investigation, a higher amount of *o*-phthalic acid could not produce the expected hollow spherical TiO_2 NPs but yielded larger and non-uniform assembiles. In addition, some agglomerates were also observed. Therefore, acetic acid (AcOH) was selected as the second acid catalyst to be mixed in the precursor solutions. The precursor solutions consisting of $Si(OEt)_4$, $Ti(O^iPr)_4$, *o*-phthalic acid, and AcOH in methanol were subjected to similar treatment as described above (Scheme 2.2). The acid concentration and physical properties of the obtained composites were given in Table 2.2.

Scheme 2.2. Schematic of synthesis of SiO_2–TiO_2 MARIMO NP composite with an addition of acetic acid.

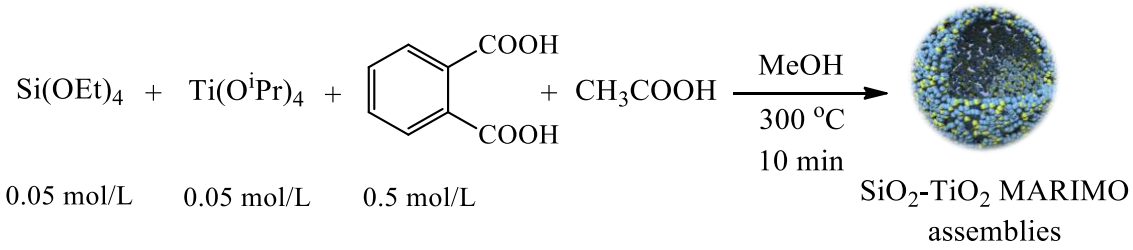

The addition of AcOH increased the yields of the corresponding composite NP assemblies (86%) and induced a higher Si content. The addition of 0.1 mol/L AcOH led to a decrease in the NP assembly size with an increase in the diameter of the inner cavity of the hollow spheres (Entry 2 in Table 2.2 and Figure 2.6b). Interestingly, a higher AcOH (0.25

mol/L) content resulted in the formation of MARIMO NP assemblies with smaller diameters (260 nm, mini MARIMO) as well as larger primary particles (Entry 3 in Table 2.2 and Figure 2.6c). It clearly demonstrated that the addition of the second acid is necessary for yielding the homogeneously mixed SiO_2–TiO_2 MARIMO assemblies.

Table 2.2. Concentration of the acid in the precursor solutions and the physical properties of the obtained NP assemblies[a].

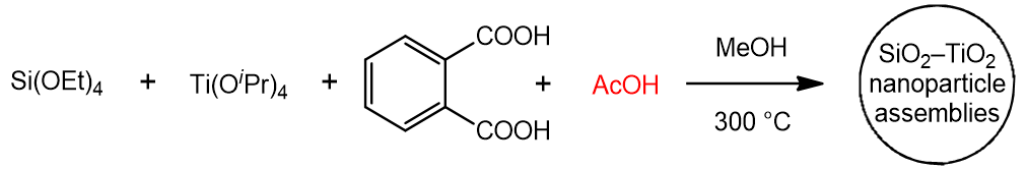

Entry	Precursor solution		SiO_2–TiO_2 composite nanoparticle assembly			
	Concentration of AcOH / *o*-$C_6H_4(COOH)_2$ (mol/L/ mol/L)	Total acid concentration (mol/L)	Yield (%)	Atomic % of Si Si/(Si+Ti)×100[b]	BET specific surface area (m^2/g)	Diameter of assembly (nm)[c]
1[d]	0/0.5	0.5	81	33.3	353	602 ± 48
2	0.1/0.5	0.6	80	33.3	451	468 ± 65
3	0.25/0.5	0.75	86	40.0	471	261 ± 52

[a]Reaction conditions: [$Ti(O^iPr)_4$] = 0.1 mol/L, [*o*-phthalic acid] = 0.5 mol/L, heating rate = 5.4 °C/min, final temperature = 300 °C, and holding time of final temperature = 10 min.

[b]Evaluated by STEM/EDX analysis.

[c]Calculated directly from the TEM images by measuring at least 40 assemblies.

[d]Same data as in Entry 4 in Table 2.1.

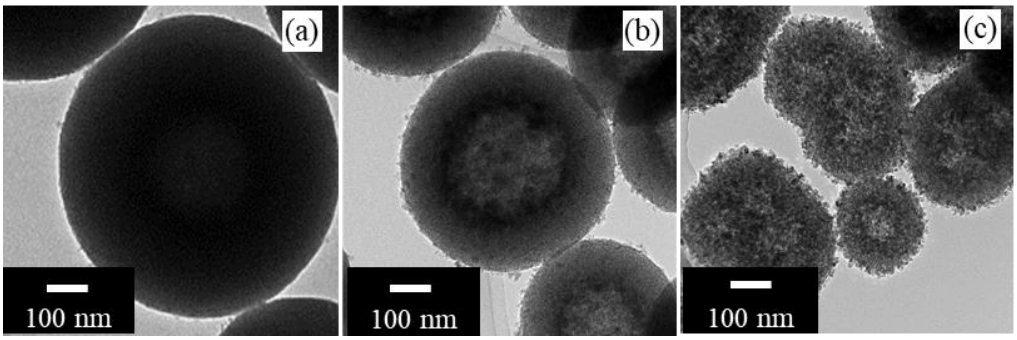

Figure 2.6. TEM images of NP assemblies obtained with different ratios of AcOH/*o*-phthalic acid (mol/L / mol/L): (a) 0/0.5 (Entry 1 in Table 2.2), (b) 0.1/0.5 (Entry 2 in Table 2.2), and (c) 0.25/0.5 (Entry 3 in Table 2.2).

2.3.2. One-pot synthesis of alkyl-modified SiO_2–TiO_2 NP assemblies

2.3.2a. A direct synthesis of alkyl-modified SiO_2–TiO_2 NP assemblies by one-pot and single-step reaction

Despite their inherent excellent properties, TiO_2 NPs have several drawbacks such as the tendency to agglomerate and poor interaction with organic materials. The surface of the primary NPs of the prototype SiO_2–TiO_2 NP assemblies including hydroxyl groups exhibited polar and hydrophilic properties, which can facilitate the dispersion of the NP assemblies in polar media such as water. However, surface hydrophobicity (lipophilicity) is necessary in some applications such as reinforcing agents in polymeric composites,[34,35] hydrophobic organic pollutant treatment,[5,36] corrosion protection of metals,[37,38] anti-biofouling, self-cleaning materials,[39] and oil-water separation.[40,41] Unfortunately, TiO_2 prepared by the chemical methods commonly exhibits a hydrophilic property which results in its weak interaction with organic media. As a consequence, TiO_2 tends to be agglomerated in organic

media instead of good dispersion, leading to negative impacts on properties of the materials for those applications. Thus, controlling HLB is one of the most important surface factors in a number of applications. Commonly, conventional routes for surface modification of TiO_2 NPs are followed by two-steps involving a synthesis of TiO_2 particles and a post-functionalization process. In situ surface modification during the synthesis of the metal oxide particles with a simplified reaction process is more attractive to yield the functionalized TiO_2 NP assemblies. This concern impelled us to investigate a variant of the one-pot and single-step method to produce alkyl-modified SiO_2–TiO_2 NP assemblies.

A similar solvothermal reaction of trimethoxy-*n*-octylsilane (*n*-octyl-Si(OMe)$_3$), instead of Si(OEt)$_4$, and Ti(O^{i}Pr)$_4$ in methanol easily afforded hollow spherical assemblies (Scheme 2.3, Entries 2 and 3 in Table 2.3 and Figures 2.7a and 2.7b).

Scheme 2.3. Schematic of synthesis of alkyl-modified SiO_2–TiO_2 NP assemblies.

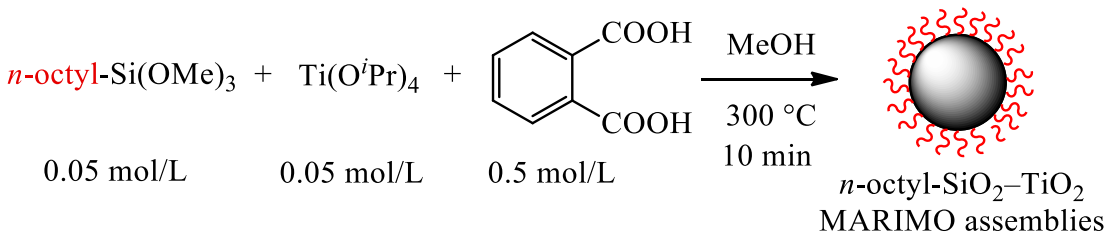

Irrespective of the concentration of *n*-octyl-Si(OMe)$_3$ in the precursor solutions, the atomic percentage of Si in the obtained assemblies was almost similar, while the yields lowered and the diameter of the assemblies became smaller. The presence of alkyl groups in the assemblies was confirmed from the FT-IR spectra (Figure 2.8b). Two C–H stretching vibration modes were clearly observed at around 2900 and 2800 cm^{-1}.[42] The existence of carbon atoms on the assemblies was confirmed by elemental analysis using the STEM/EDX mapping technique equipped in TEM (Figures 2.7a and 2.7b).

Table 2.3. Preparation of *n*-octyl-SiO_2–TiO_2 composite nanoparticle assemblies.[a]

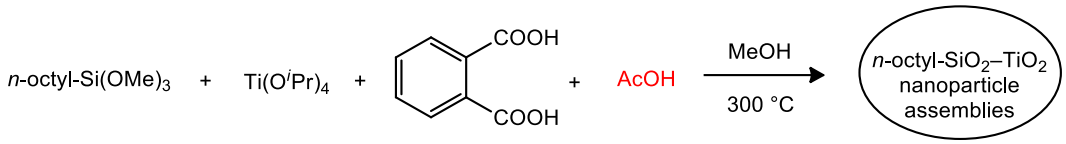

Entry	Precursor solution			Reaction temperature (°C)	SiO_2–TiO_2 composite NP assembly		
	n-octyl-Si(OMe)$_3$ (mol/L)	Ti(O^{i}Pr)$_4$ (mol/L)	AcOH (mol/L)		Yield (%)	Atomic % of Si in composite NP assembly[b]	Diameter of assembly (nm)[c]
1[d]	0	0.05	0	300	89	0	700 ± 50
2	0.025	0.075	0	300	59	4.0	630 ± 106
3	0.05	0.05	0	300	32	3.9	470 ± 76
4	0.05	0.05	0	350	32	6.7	392 ± 48
5	0.05	0.05	0	400[e]	12	16.7	362 ± 45
6[f]	0.05	0.05	0	300	12	–[g]	–[g]
7	0.05	0.05	0.1	300	35	6.7	284 ± 41
8	0.05	0.05	0.1[h]	300	30	5.7	233 ± 45

[a]Reaction conditions: [*o*-phthalic acid] = 0.5 mol/L, heating rate = 5.4 °C/min, final temperature = 300 °C, and holding time of final temperature = 10 min.

[b]Evaluated by STEM/EDX analysis.

[c]Calculated directly from the TEM images by measuring at least 40 assemblies.

[d]Same data as in Entry 1 in Table 2.1.

[e]Reaction mixture smelled like heavy oil, which can be ascribed to the thermal decomposition of alkylsilane at high temperature.

[f]EtOH was used as a solvent.

[g]Two types of structures were found (see main text). [h] Formic acid was used instead of acetic acid.

[h]HCOOH was used instead of AcOH.

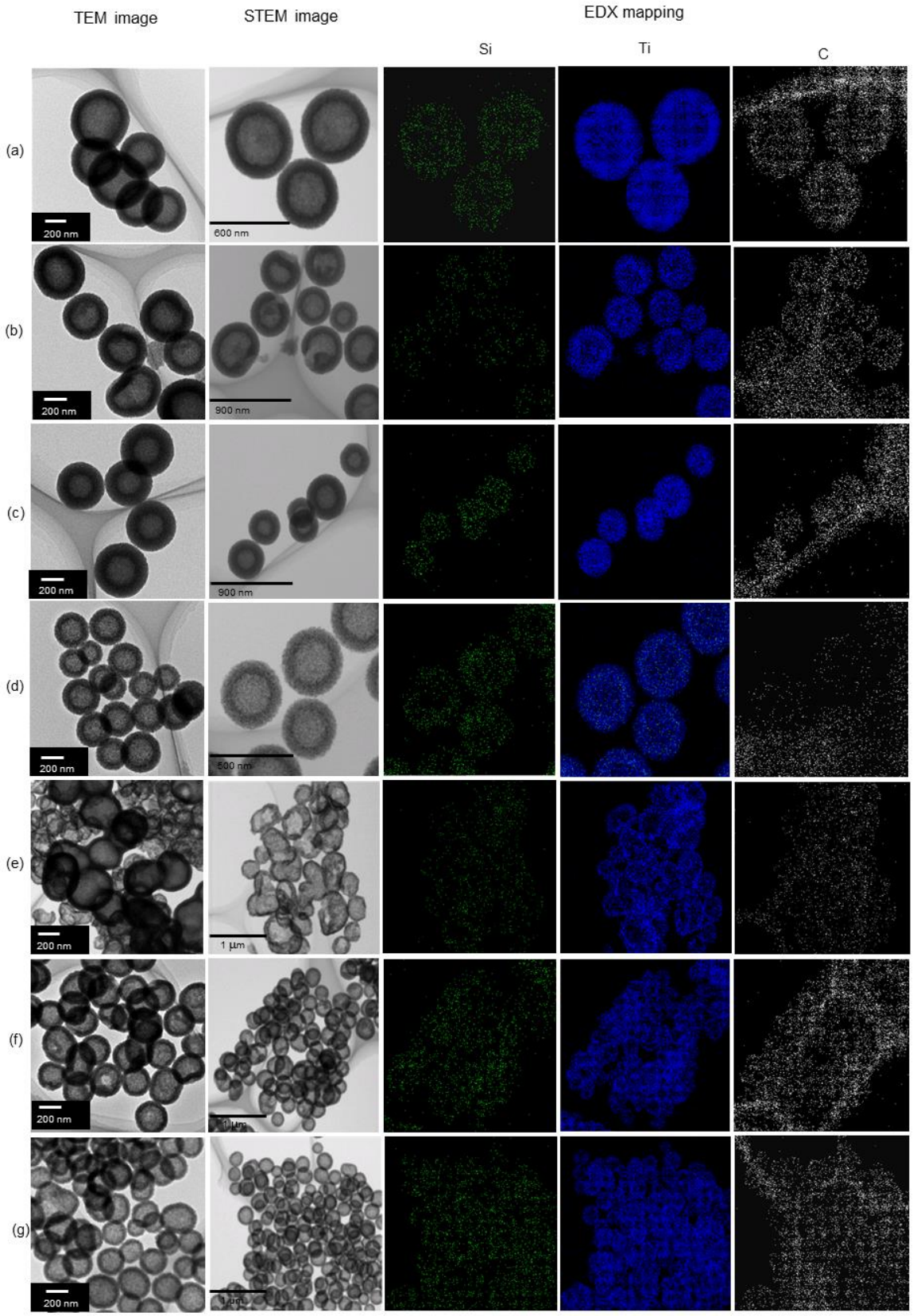

Figure 2.7. TEM images, STEM images, and EDX mapping of *n*-octyl-SiO_2–TiO_2 NP assemblies with compositions corresponding to (a) Entry 2, (b) Entry 3, (c) Entry 4, (d) Entry 5, (e) Entry 6, (f) Entry 7, and (g) Entry 8 in Table 2.3.

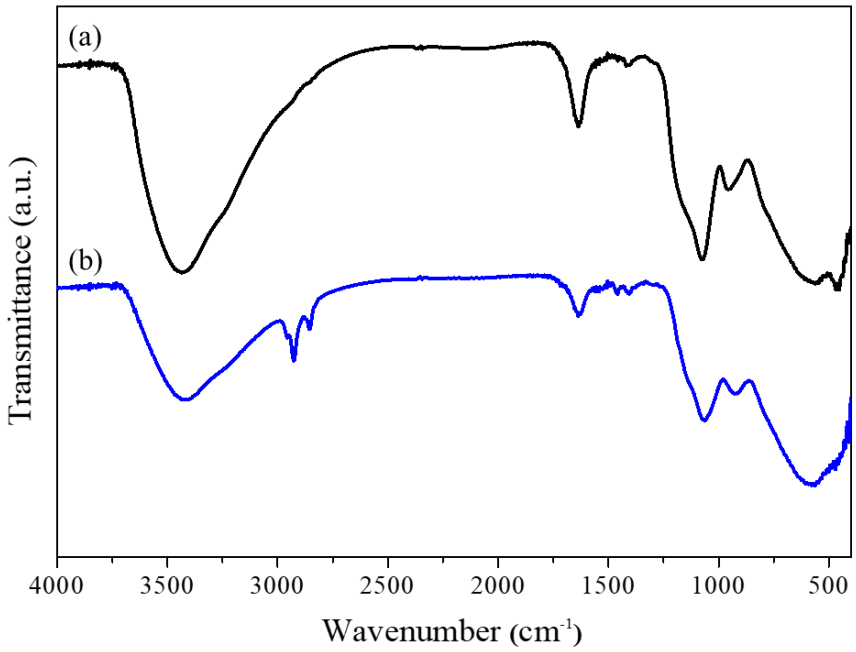

Figure 2.8. FT-IR spectra of (a) TiO_2–SiO_2 NP assembly (Entry 4 in Table 2.1) and (b) *n*-octyl-SiO_2–TiO_2 NP assembly (Entry 3 in Table 2.3).

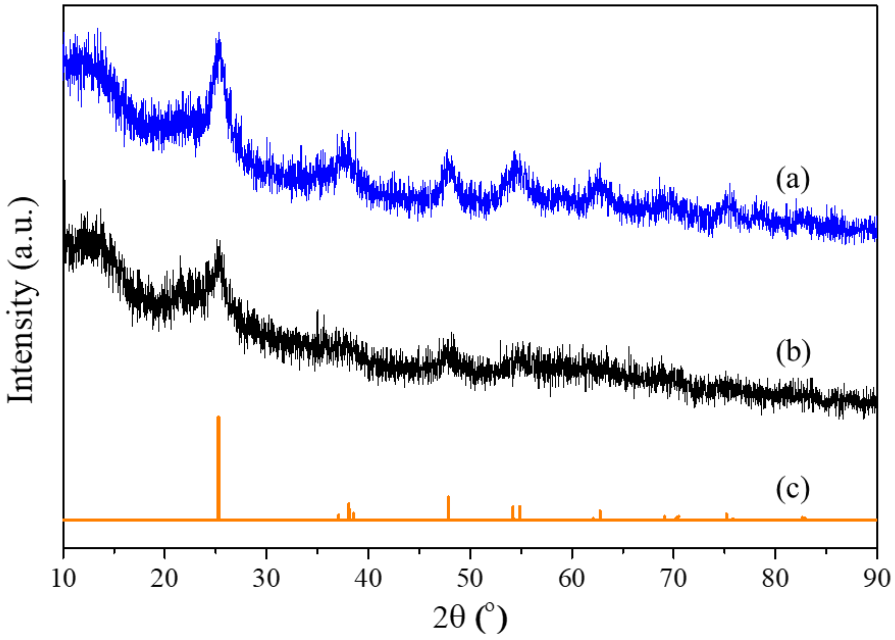

Figure 2.9. XRD patterns of (a) *n*-octyl-SiO_2–TiO_2 NP assembly (Entry 3 in Table 2.3), (b) SiO_2–TiO_2 NP assembly (Entry 4 in Table 2.1), and (c) standard anatase TiO_2 (JCPDS 21-1272).

XRD analysis shows the characteristic peaks of the anatase phase for *n*-octyl-SiO_2–TiO_2 NP assemblies (Figure 2.9a), which are very similar to that of the prototype SiO_2–TiO_2 NP assembly. Again, the crystalline phase of SiO_2 was not observed in the XRD spectra (Figures 2.7); however, a broad peak in the $2\theta<20°$ region indicated the amorphous phase of SiO_2 in both prototype SiO_2–TiO_2 NP assemblies and *n*-octyl-SiO_2–TiO_2 NP assemblies.

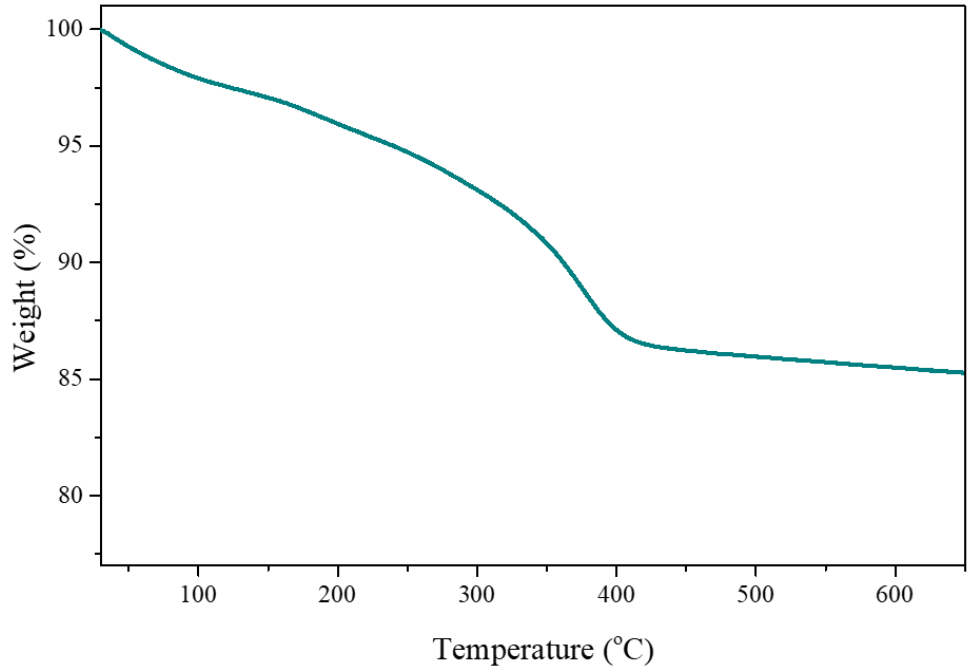

Figure 2.10. Thermogravimetric curve of *n*-octyl-SiO_2–TiO_2 composite NP assemblies fabricated by solvothermal reaction at 300 °C (Entry 3 in Table 2.3).

To evaluate the amount of the modified alkyl group, the thermogravimetric (TG) analysis of the resultant *n*-octyl-SiO_2–TiO_2 NP assemblies was also conducted. As indicated in Figure 2.10, TG analysis curve of the *n*-octyl-SiO_2–TiO_2 NP assemblies resulted in *ca.* 14% loss in weight at 600 °C. However, owing to not only decomposition of *n*-octyl groups but also dehydration of the surface Si–OH and/or Ti–OH on NP assemblies, it is difficult to put forward a quantitative discussion on the amount of alkyl group.

2.3.2b. Effect of the reaction conditions on the obtained alkyl-modified SiO_2–TiO_2 NP assemblies

Effect of the reaction temperature

To accelerate the hydrolysis rate of the precursors, to elevate the reaction temperature is the easiest approach (Entries 3-5 in Table 2.3). TEM observations revealed that the hollow spherical morphology of the obtained NP assemblies remained almost the same when the reaction temperature varied from 300 to 400 °C (Figures 2.7b-d); however a significant difference was observed in the chemical composition of the SiO_2–TiO_2 assemblies, that is, higher amounts of Si resulted from higher reaction temperature, which can be attributed to faster hydrolysis of the silane coupling reagent at such high temperature. Unfortunately, the reaction mixture obtained at 400 °C smelled like heavy oil, which can be ascribed to the thermal decomposition of alkyl-silane at a high reaction temperature of 400 °C.

Effect of the second acid catalyst

As discussed in the section 2.3.1b, the effect of the second acid catalyst in accelerating the hydrolysis rate of the alkylsilane reagents was examined (Entries 7 and 8 in Table 2.3 and Figures 2.7f and 2.7g). The SiO_2–TiO_2 composite NP assemblies with hollow mesoporous morphologies and a higher Si content were obtained by the addition of AcOH. Formic acid (HCOOH) was also effective in yielding the composite NP assemblies with a hollow morphology (Entry 8 in Table 2.3 and Figure 2.7g). In both the cases, the size of the NP assemblies dramatically shrank leading to the formation of "mini MARIMO" NP assemblies.

Effect of the reaction solvent

It has been reported that the reaction medium is a crucial factor that affects the hydrolysis

and condensation processes of metal alkoxides and metal salts.[32,33] Ethanol (EtOH), with lower polarity and higher nucleophilicity, was selected as an alternative solvent. Similar solvothermal treatment of an EtOH solution consisting of equimolar amounts of *n*-octyl-$Si(OMe)_3$ and $Ti(O^iPr)_4$, and *o*-phthalic acid afforded homogeneously mixed SiO_2–TiO_2 composite assemblies (Entry 6 in Table 2.3). However, a mixture of two types of spherical hollow NP assemblies was obtained: larger diameters with thicker shells and smaller diameters with thinner shells (Figure 2.7e). This indicates that solvent polarity is a crucial factor in the formation of hollow spherical structures.

2.3.2c. Dispersibility of *n*-octyl-modified SiO_2–TiO_2 NP assemblies in media

The effect of the alkyl groups attached on the surface of the spherical NP assemblies was assessed by their dispersibility in nonpolar and polar solvents. Toluene and MeOH were selected as representative nonpolar and polar solvents, respectively. Aliquots of NP assemblies with (Entry 7 in Table 2.3) and without *n*-octyl surface modification (TiO_2 MARIMO assembly, Entry 1 in Table 2.3) were dispersed in toluene and methanol (Figure 2.11). In the case of nonpolar solvent (toluene), the dispersibility of *n*-octyl-SiO_2–TiO_2 NP assemblies was better than that of TiO_2 MARIMO assembly, as observed from the turbidity of the corresponding dispersions after 90 min (Figure 2.11). Under laser irradiation, the suspension of *n*-octyl-SiO_2–TiO_2 NP assemblies appeared more turbid because of its high particle density. In contrast, agglomerates of TiO_2 MARIMO NPs were seen to be settled at the bottom of the tube. However, in the case of the polar solvent (MeOH), a reverse phenomenon was observed in which the turbidity of the TiO_2 MARIMO suspension was much denser than that of *n*-octyl-SiO_2–TiO_2 NP assemblies after 90 min. This result clearly indicates the effectiveness of the surface alkyl groups on the dispersibility of *n*-octyl-SiO_2–TiO_2 NPs in nonpolar media.

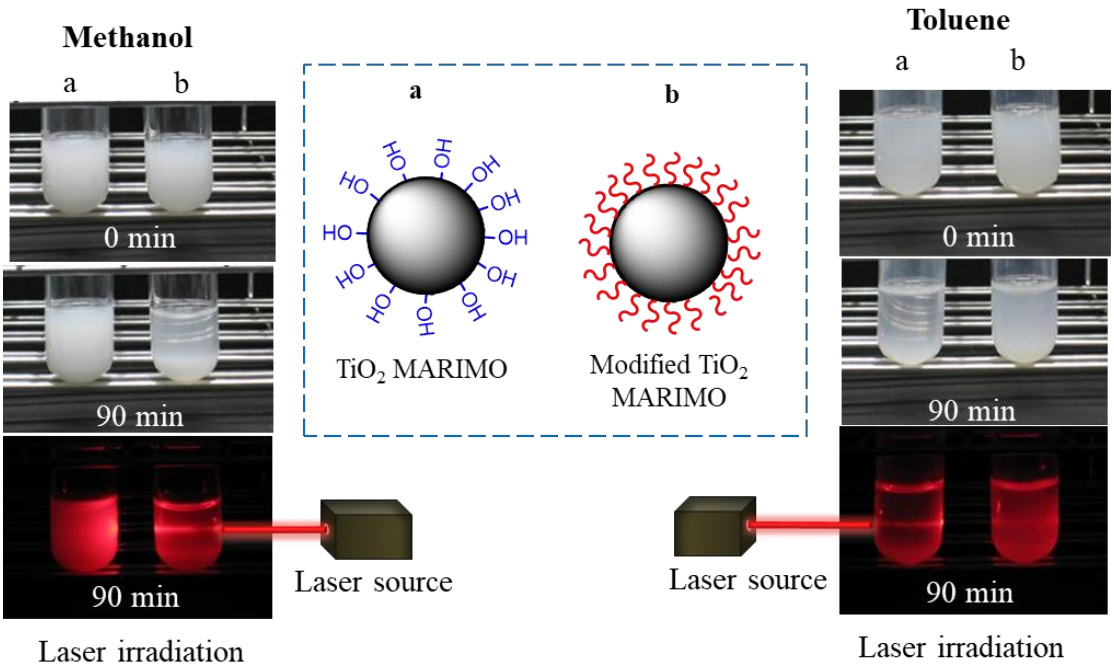

Figure 2.11. Dispersibility test of (a) and (c) TiO_2 MARIMO NP assemblies (Entry 1 in Table 2.3), and (b) and (d) *n-octyl*-TiO_2–SiO_2 NPs assemblies (Entry 7 in Table 2.3) in toluene and methanol.

2.4. Conclusion

We succeeded in applying our simple technique to prepare the SiO_2–TiO_2 composite NP assemblies and *n*-octyl-modified SiO_2–TiO_2 composite NP assemblies through the one-step solvothermal reaction. The hydrolysis rate of the Si precursor was accelerated by the addition of a second acid catalyst and with an increase in the reaction temperature. The atomic ratio of SiO_2:TiO_2 in the NP assemblies was controlled by adjusting the mole ratio of $Si(OEt)_4$:$Ti(O^iPr)_4$ in the precursor solutions. The concentration of the acid catalyst and the reaction temperature were also critical to the determination of Si content in the SiO_2–TiO_2 composite NP assemblies. Although reaction at high temperatures such as 400 °C increased the Si content in the composite NP assemblies, a partial decomposition of the *n*-octyl groups during the reaction should also be considered. A positive effect on

the formation of NP assemblies with a high content Si was observed when acetic acid was added to the precursor solution as a second acid catalyst. A size decrease of the NP assemblies yielding "mini MARIMO" was concomitant with an increase in the Si content in the presence of acetic acid or formic acid. In addition, a mixture of different NP assemblies was obtained when ethanol was used as the solvent for the reaction. The surface modification of the NP assemblies with *n*-octyl groups remarkably changed the dispersibility of the TiO_2 NP assemblies in a nonpolar solvent such as toluene.

Reference

[1] A. Suligoj, U. Stangar, A. Ristic, M. Mazaj, D. Verhovsek, N. Tusar, TiO_2–SiO_2 films from organic-free colloidal TiO_2 anatase nanoparticles as photocatalyst for removal of volatile organic compounds from indoor air, *Appl. Catal. B-Environ.* 2016, *184*, 119–131.

[2] D. Chen, R. Caruso, Recent progress in the synthesis of spherical titania nanostructures and their applications, *Adv. Funct. Mater.* **2013**, *23*, 1356–1374.

[3] M. Cargnello, T. Gordon, C. Murray, Solution-phase synthesis of titanium dioxide nanoparticles and nanocrystals, *Chem. Rev.* **2014**, *114*, 9319–9345.

[4] L. Sang, Y. Zhao, C. Burda, TiO_2 nanoparticles as functional building blocks, *Chem. Rev.* **2014**, *114*, 9283–9318.

[5] H. Dong, G. Zeng, L. Tang, C. Fan, C. Zhang, X. He, Y. He, An overview on limitations of TiO_2-based particles for photocatalytic degradation of organic pollutants and the corresponding countermeasures, *Water Res.* **2015**, *79*, 128–146.

[6] Y. Kondo, H. Yoshikawa, K. Awaga, M. Murayama, T. Mori, K. Sunada, S. Bandow, S. Iijima, Preparation, photocatalytic activities, and dye-sensitized solar-cell performance of submicron-scale TiO_2 hollow spheres, *Langmuir* **2008**, *24*, 547–550.

[7] P. Roy, S. Berger, P. Schmuki, TiO_2 nanotubes: synthesis and applications, *Angew. Chem.*

Int. Ed. **2011**, *50*, 2904–2939.

[8] E. Gultepe, D. Nagesha, S. Sridhar, M. Amiji, Nanoporous inorganic membranes or coatings for sustained drug delivery in implantable devices, *Adv. Drug Deliv. Rev.* **2010**, *62* 305–315.

[9] H. Park, Y. Park, W. Kim, W. Choi, Surface modification of TiO_2 photocatalyst for environmental applications, *J. Photochem. Photobiol. C* **2013**, *15*, 1–20.

[10] Y. Ma, X. Wang, Y. Jia, X. Chen, H. Han, C. Li, Titanium dioxide-based nanomaterials for photocatalytic fuel generations, *Chem. Rev.* **2014**, *114*, 9987–10043.

[11] B. Guan, L. Yu, J. Li, X. Lou, A universal cooperative assembly-directed method for coating of mesoporous TiO_2 nanoshells with enhanced lithium storage properties, *Sci. Adv.* **2016**, *2*, e1501554, 1–8.

[12] L. Yu, H. Hu, H. B. Wu, X. Lou, Complex hollow nanostructures: synthesis and energy - related applications, *Adv. Mater.* **2017**, *29*, 1–39.

[13] Q. Xu, Y. Liu, F. Lin, B. Mondal, A. Lyons, Superhydrophobic TiO_2–polymer nanocomposite surface with UV-induced reversible wettability and self-cleaning properties, *Appl. Mater. Interfaces* **2013**, *5*, 8915–8924.

[14] T. Radoman, J. Dzunuzovic, K. Trifkovic, T. Palija, A. Marinkovic, B. Bugarski, E. Dzunuzovic, Effect of surface modified TiO_2 nanoparticles on thermal, barrier and mechanical properties of long oil alkyd resin-based coatings*, Express Polym. Lett.* **2015**, *9*, 916–931.

[15] L. Yao, Z. Pan, S. Liu, J. Zhai, H. Chen, Significantly enhanced energy density in nanocomposite capacitors combining the TiO_2 nanorod array with poly(vinylidene fluoride), *Appl. Mater. Interfaces* **2016**, *8*, 26343–26351.

[16] J. Li, S. Seok, B. Chu, F. Dogan, Q. Zhang, Q. Wang, Nanocomposites of ferroelectric polymers with tio_2 nanoparticles exhibiting significantly enhanced electrical energy

density, *Adv. Mater.* **2009**, *21*, 217–221.

[17] C. Sciancalepore, T. Cassano, M. Curri, D. Mecerreyes, Valentini, A. Agostiano, R. Tommasi, M. Striccoli, TiO_2 nanorods/PMMA co-polymer based nanocomposites: highly homogeneous linear and non linear optical material, *Nanotechnology* **2008**, *19*, 205705–205713.

[18] M. Vona, E. Sgreccia, A. Donnadio, M. Casciola, J. Chailan, G. Auer, P. Knauth, Composite polymer electrolytes of sulfonated poly-ether-ether-ketone (SPEEK) with organically functionalized TiO_2, *J. Membr. Sci.* **2011**, *369*, 536–544.

[19] S. Kango, S. Kalia, A. Celli, J. Njuguna, Y. Habibi, R. Kumar, Surface modification of inorganic nanoparticles for development of organic–inorganic nanocomposites: a review, *Prog. Polym. Sci.* **2013**, *38*, 1232–1261.

[20] N. Guo, Y. Liang, S. Lan, L. Liu, G. Ji, S. Gan, H. Zou, X. Xu, Uniform TiO_2–SiO_2 hollow nanospheres: synthesis, characterization and enhanced adsorption–photodegradation of azo dyes and phenol, *Appl. Surf. Sci.* **2014**, *305*, 562–574.

[21] X. Gao, I.E. Wachs, Titania–silica as catalysts: molecular structural characteristics and physico-chemical properties, *Catal. Today* **1999**, *51*, 233–254.

[22] Š. Paušová, J. Krysa, J. Jirkovsky, V. Prevot, G. Mailhot, Preparation of TiO_2–SiO_2 composite photocatalysts for environmental applications, *J. Chem. Technol. Biotechnol.* **2014**, *89*, 1129–1135.

[23] S. Ullah, E.P. Ferreira-Neto, A. Pasa, C. Alcântara, J. Acũna, S. Bilmes, M. Ricci, R. Landers, T. Fermino, U. Rodrigues-Filho, Enhanced photocatalytic properties of core@shell SiO_2@TiO_2 nanoparticles, *Appl. Catal. B-Environ.* **2015**, *179*, 333–343.

[24] J. Yun, J. Ryu, J. Lee, H. Yu, J. Jang, SiO_2/TiO_2 based hollow nanostructures as scaffold layers and Al-doping in the electron transfer layer for efficient perovskite solar cells, *J. Mater. Chem.* A **2016**, *4*, 1306–1311.

[25] S. Sen, V. Govindarajan, C. Pelliccione, J. Wang, D. Miller, E. Timofeeva, Surface modification approach to TiO_2 nanofluids with high particle concentration, low viscosity, and electrochemical activity, *Appl. Mater. Interfaces* **2015**, *7*, 20538–20547.

[26] C. García-González, J. Saurina, J. Ayllón, C. Domingo, Preparation and characterization of surface silanized TiO_2 nanoparticles under compressed CO_2: reaction kinetics, *J. Phys. Chem. C* **2009**, *113*, 13780–13786.

[27] C. Wang, H. Mao, C. Wang, S. Fu, Dispersibility and hydrophobicity analysis of titanium dioxide nanoparticles grafted with silane coupling agent, *Ind. Eng. Chem. Res.* **2011**, *50*, 11930–11934.

[28] I. Joni, A. Purwanto, F. Iskandar, K. Okuyama, Dispersion stability enhancement of titania nanoparticles in organic solvent using a bead mill process, *Ind. Eng. Chem. Res.* **2009**, *48*, 6916–6922.

[29] P. Wang, K. Ueno, H. Takigawa, K. Kobiro, Versatility of one-pot, single-step synthetic approach for spherical porous (metal) oxide nanoparticles using supercritical alcohols, *J. Supercrit. Fluid* **2013**, *78*, 124–131.

[30] P. Wang, K. Yokoyama, T. Konishi, N. Nishiwaki, K. Kobiro, Ultimately simple one-pot single-step synthesis of rare earth doped spherical mesoporous metal oxide nanospheres with upconversion emission ability in supercritical methanol, *J. Supercrit. Fluid* **2013**, *80*, 71–77.

[31] E.K.C. Pradeep, M. Ohtani, K. Kobiro, A simple synthetic approach to Al_2O_3–TiO_2 and ZnO–TiO_2 mesoporous hollow composite assemblies consisting of homogeneously mixed primary particles at the nano level, *Eur. J. Inorg. Chem.* **2015**, *2015*, 5621–5627.

[32] P. Wang, K. Kobiro, Synthetic versatility of nanoparticles: a new, rapid, one-pot, single-step synthetic approach to spherical mesoporous (metal) oxide nanoparticles using supercritical alcohols, *Pure Appl. Chem.* **2014**, *86*, 785–800.

[33] U. Schubert, Sol–Gel Chemistry and Methods in *The Sol–Gel Handbook: Synthesis, Characterization, and Applications*, (Eds.: D. Levy, M. Zayats), Wiley-VCH, Weinheim, **2015**, pp. 1–27.

[34] S. Peng, B. Dang, Y. Zhou, J. Hu, J. He, Functionalized TiO_2 nanoparticles tune the aggregation structure and trapping property of polyethylene nanocomposites, *J. Phys. Chem. C* **2016**, *120*, 24754–24761.

[35] D. Koziej, F. Fischer, N. Kranzlin, W.R. Caseri, M. Niederberger, Nonaqueous TiO_2 nanoparticle synthesis: a versatile basis for the fabrication of self-supporting, transparent, and UV-absorbing composite films, *Appl. Mater. Interfaces* **2009**, *1*, 1097–1104.

[36] K. Shimizu, H. Murayama, A. Nagai, A. Shimada, T. Hatamachi, T. Kodama, Y. Kitayama, Degradation of hydrophobic organic pollutants by titania pillared fluorine mica as a substrate specific photocatalyst, *Appl. Catal. B-Environ.* **2005**, *55*, 141–148.

[37] G. Shen, Y. Chen, L. Lin, C. Lin, D. Scantlebury, Study on a hydrophobic nano-TiO_2 coating and its properties for corrosion protection of metals, *Electrochim. Acta* **2005**, *50*, 5083–5089.

[38] Y. Hu, S. Huang, S. Liu, W. Pan, A corrosion-resistance superhydrophobic TiO_2 film, *Appl. Surf. Sci.* **2012**, *258*, 7460–7464.

[39] S.Wooh, N.Encinas, D.Vollmer, H. Butt, Stable hydrophobic metal-oxide photocatalysts via grafting polydimethylsiloxane brush, *Adv. Mater.* **2017**, *1604637*, 1–7.

[40] J. Huang, S. Li, M. Ge, L. Wang, T. Xing, G. Chen, X. Liu, S. Al-Deyab, K. Zhang, T. Chen, Y. Lai, Robust superhydrophobic TiO_2@fabrics for UV shielding, self-cleaning and oil–water separation, *J. Mater. Chem. A* **2015**, *3*, 2825–2832.

[41] E. Cho, C. Chang-Jian, Y. Hsiao, K. Lee, J. Huang, Interfacial engineering of melamine sponges using hydrophobic TiO_2 nanoparticles for effective oil/water separation, *J.*

Taiwan Inst. Chem. Eng. **2016**, *67*, 476–483.

[42] D. Lin-Vien, N.B. Colthup, W.G. Fateley, J.G. Grasselli, Alkanes in *The Handbook of Infrared and Raman Characteristic Frequencies of Organic Molecules*, Academic Press Limited London, **1991**, pp. 9–28.

CHAPTER III

One-pot synthesis of SiO_2–CeO_2 nanoparticle composites with enhanced heat tolerance

3.1. Introduction

Nano-scale CeO_2 is a well-known material often used in fuel cells, biomedicine, and catalysis. Commonly, CeO_2 can be used both as a catalyst and a support for noble metal catalysts.[1–9] Importantly, one of the most interesting properties of CeO_2 nanomaterial is its redox change between the coexisted Ce^{4+} and Ce^{3+} oxidation states in the structure associated with the generation of oxygen vacancies, referred to as oxygen storage capacity.[10–14] By these means, the CeO_2 nanomaterial is a key material in catalytic applications, for example, reforming processes, water-gas shift reaction, and thermochemical water splitting. Notably, depending on the preparation methods, the content of oxygen vacancies and proportion of Ce^{3+}/Ce^{4+} in the structure of CeO_2 can change, leading to different catalytic activities. Therefore, the appropriate synthetic strategies allow to control the catalytic activity of CeO_2 nanomaterials.

Despite the numerous advantages of CeO_2, its poor heat tolerance is a serious drawback that limits its use in high-temperature processes.[15] During operation under high-temperature conditions, the mobile CeO_2 particles tend to migrate and grow resulting in large agglomerates, following by loss of surface area of the material (Figure 3.1). As the consequence of CeO_2 sintering, the activity of the CeO_2 nanomaterial is decreased and even deactivated. Preventing or suppressing these sintering processes of CeO_2 nanomaterials under effect of heat is required importantly to keep the CeO_2 nanomaterials stable for a long-time use.

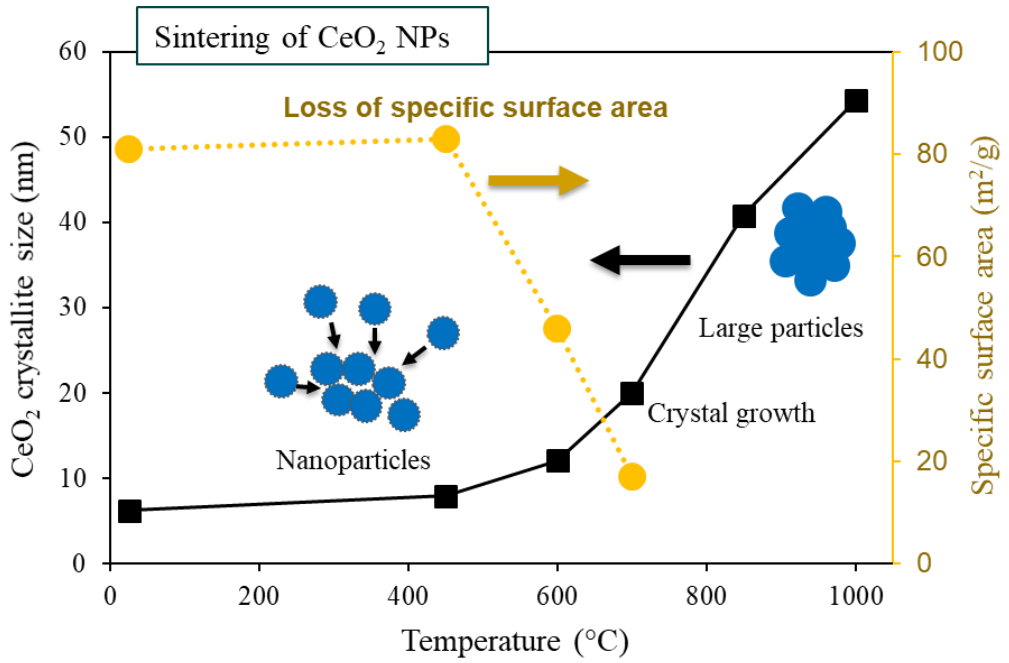

Figure 3.1. Sintering of CeO_2 NPs during heating to high temperature.

Indeed, when the catalysts are used for exothermic or high-temperature reactions, the heat tolerance of CeO_2 catalysts or catalyst supports are important for long catalyst life.[16–19] However, under those high-temperature conditions, CeO_2 NPs are often sintered due to migration of NPs to larger particles, which leads to loss of the surface area and the catalytic activity.[20–22]

As mentioned previously, metal oxide NP assemblies such as SiO_2, TiO_2, ZrO_2, and CeO_2 and their composite assemblies were successfully prepared by the one-pot, single-step solvothermal processes.[23–27] Also, we succeeded in yielding the SiO_2–TiO_2 composite MARIMO assemblies with the controllable Si:Ti atomic ratios by the solvothermal reaction of a precursor solution consisting of $Si(OEt)_4$, $Ti(O^iPr)_4$, and acid additives in methanol, which was discussed in chapter II.[28] Importantly, the key to obtain the homogeneously mixed composite SiO_2–TiO_2 NP assemblies is to accelerate the hydrolysis rate of $Si(OEt)_4$ by the addition of second acid such as formic acid, because the hydrolysis of $Si(OEt)_4$ in the precursor

solution is much slower than that of $Ti(O^iPr)_4$. The SiO_2–TiO_2 composite MARIMO assemblies generated consist of a homogeneously mixed, nano-sized anatase TiO_2 phase and an amorphous SiO_2 phase.

As a member of the SiO_2 composites, SiO_2–CeO_2 composites are intriguing materials, since they exhibit higher heat tolerance than that of prototype mono-component CeO_2 NP aggregates.[29–33] By mixing at nano-level, the SiO_2–CeO_2 composites are highly expected to overcome the drawback of poor heat tolerance of mono-component CeO_2. In the SiO_2–CeO_2 NP composites, the small crystallite size of CeO_2 and large NP surface area are retained even under high-temperature conditions, because nano-sized CeO_2 primary crystals get encapsulated in amorphous SiO_2, suppressing the sintering of CeO_2 NPs (Figure 3.2).

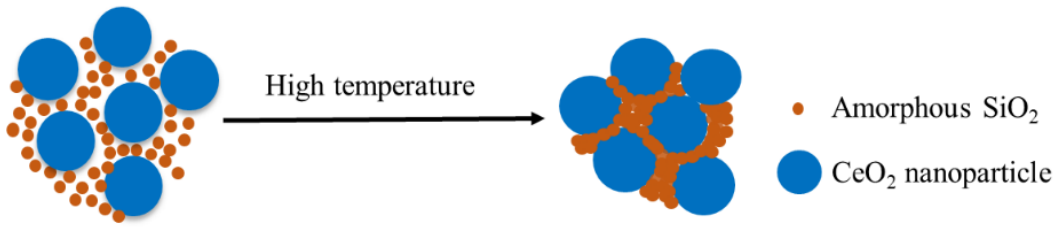

Figure 3.2. Strategy for sintering suppression of CeO_2 NPs in SiO_2–CeO_2 NP composites.

However, synthesis of these SiO_2–CeO_2 NP composites has been relatively complicated and sometimes required multi-step processes. For example, a surfactant-aided interesting synthetic procedure was reported.[29] However, a calcination process was necessary to remove organic additives from the composites. In this Chapter, I applied our simple technique to synthesize the homogeneously mixed SiO_2–CeO_2 NP composites through one-pot and single-step solvothermal reaction. The enhanced heat tolerance of CeO_2 NPs embedded in amorphous SiO_2 is also discussed.

3.2. Experimental section

3.2.1. Materials

Methanol, cerium nitrate hexahydrate [$Ce(NO_3)_3 \cdot 6H_2O$], tetraethyl orthosilicate [$Si(OEt)_4$], and *N*,*N*,*N*',*N*'-tetramethylethylenediamine [$(CH_3)_2NCH_2CH_2N(CH_3)_2$] were provided by Wako Pure Chemical Industries Co. Ltd. All chemicals were used as received, without further purification.

3.2.2. Synthesis of SiO_2–CeO_2 NP composites

SiO_2–CeO_2 NP composites were synthesized by a one-pot, single-step solvothermal reaction of methanol solutions consisting of $Si(OEt)_4$, $Ce(NO_3)_3 \cdot 6H_2O$, and $(CH_3)_2NCH_2CH_2N(CH_3)_2$. In a typical procedure, a methanol solution of the amine was added dropwise to a homogeneous methanol solution containing $Si(OEt)_4$ and $Ce(NO_3)_3 \cdot 6H_2O$. The solution became turbid after the addition of the amine. The turbid mixture was transferred into an SUS 316 stainless steel batch-type reactor. To perform the reaction, the reactor was heated up to 300 ºC at a heating rate of 5.4 °C/min and the temperature was maintained for 10 min. Then, the reactor was put into an ice-water bath to quench the reaction. The obtained reaction mixture was centrifuged, and the solid product was washed with methanol several times prior to drying *in vacuo*.

3.2.3. Characterization

Crystalline phases of the resultant NP composites were identified by X-Ray diffractometry (XRD) on a Rigaku SmartLab diffractometer using graphite-monochromated

Cu-K_α radiation. The crystallite sizes of CeO_2 were determined by the Scherrer equation as given below.[21,34,35]

$$D = \frac{K\lambda}{\beta(\cos\theta)}$$

Where D is the mean size of the crystallite domains (nm). K is a dimensionless shape factor with value of 0.9 used in this study. λ is wavelength of X-ray (nm). β is the line broadening at half the maximum intensity (Full Width at Half Maximum, FWHM) using a peak at 2θ = 28.6 º in the XRD patterns and θ is the diffraction angle.

Transmission electron microscopy (TEM) images were taken on a JEOL JEM-2100F microscope. The elemental compositions of the composites were quantified by energy dispersive X-ray (EDX) spectroscopy using an Oxford INCA X-max 80 EDX spectrometer, attached to the TEM instrument. The specific surface area and pore size distribution of the SiO_2–CeO_2 NP composites were calculated using the Brunauer–Emmett–Teller (BET) method and Barrett-Joyner-Halenda (BJH) method, respectively, based on the nitrogen adsorption/desorption isotherm obtained on a BELSORP-mini II instrument (MicrotracBEL Corp).

To evaluate oxygen adsorption ability for commercial CeO_2, as-prepared CeO_2, and as-prepared 0.5/SiO_2–CeO_2 composite, temperature-programmed desorption of oxygen (O_2-TPD) was carried out in a flow-type reactor (BELCAT II, MicrotracBEL Corp.). The samples were pretreated in He for 1 h at 300 °C prior to O_2 adsorption (20 mL/min) at 35 °C for 30 min. Then, He was purged for 30 min to completely remove physically adsorbed O_2 before the O_2-TPD experiment was run from 35 °C to 600 °C at a ramping rate of 5 °C/min for the desorption.

3.3. Results and discussion

3.3.1. Synthesis of CeO_2 NP aggregates and SiO_2–CeO_2 NP composites under basic conditions

As mentioned previously, we have developed a novel approach for obtaining SiO_2–TiO_2 composite MARIMO assemblies by solvothermal reactions of precursor solutions consisting of $Si(OEt)_4$, $Ti(O^iPr)_4$, and *o*-phthalic acid in methanol.[28] Since the hydrolysis rate of $Si(OEt)_4$ was slower than that of $Ti(O^iPr)_4$, formic acid was added to the precursor solution as an acid catalyst to accelerate the hydrolysis of $Si(OEt)_4$. The homogeneous SiO_2–CeO_2 MARIMO composites was expected to be prepared by a similar method, using formic acid as a catalyst to accelerate the hydrolysis of $Si(OEt)_4$.

Scheme 3.2. Schematic of synthesis of the SiO_2–TiO_2 MARIMO NP assemblies in the presence of phthalic acid and formic acid.

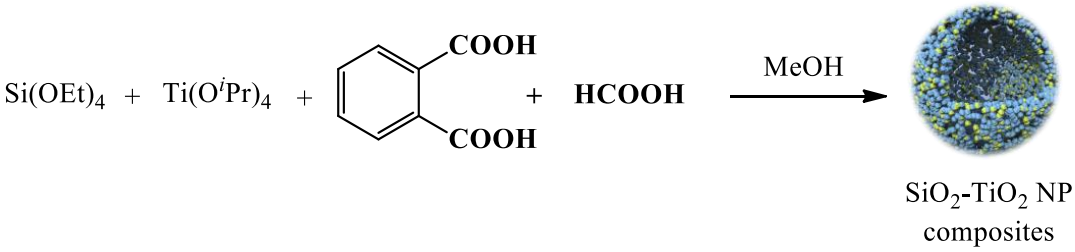

However, a large amount of formic acid with $Ce(NO_3)_3{\cdot}6H_2O$ in methanol in the solvothermal reaction led to the formation of cerium formate [$Ce(OCHO)_3$] instead of CeO_2. Therefore, herein I used basic conditions, using $(CH_3)_2NCH_2CH_2N(CH_3)_2$ (TMEDA) to accelerate the hydrolysis of $Si(OEt)_4$ in methanol (Scheme 3.2).

Scheme 3.2. Schematic of synthesis of SiO_2–CeO_2 NP composites in a basic condition.

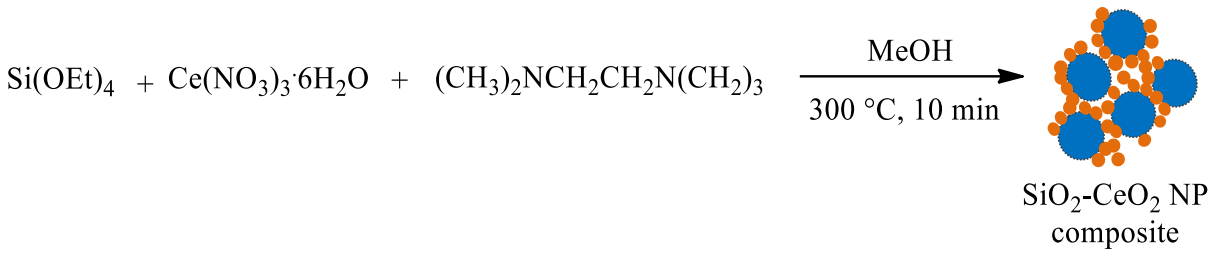

A precursor solution containing $Si(OEt)_4$ (0.1 mol/L), $Ce(NO_3)_3 \cdot 6H_2O$ (0.1 mol/L), and TMEDA (0.2 mol/L) in methanol (3.5 mL) was treated under solvothermal conditions at 300 ºC to yield a powdery product of 0.5/SiO_2–CeO_2, where the number 0.5 denotes the atomic fraction of Si to the total number of Si and Ce atoms in the precursor solution. TEM images and STEM/ EDX mappings clearly show that the 0.5/SiO_2–CeO_2 NP composites contained ultrafine primary NPs, in which Si and Ce atoms were homogeneously mixed within the resolution limitation of our TEM (Figures 3.3a-d). The XRD pattern showed that the 0.5/SiO_2–CeO_2 was comprised of cubic CeO_2 and, surprisingly, its crystallite size was as small as 2.2 nm, estimated by the Scherrer equation (Table 3.1, Figure 3.3e). On the other hand, diffraction peaks of SiO_2 were not observed, clearly indicating that SiO_2 exists as an amorphous phase.

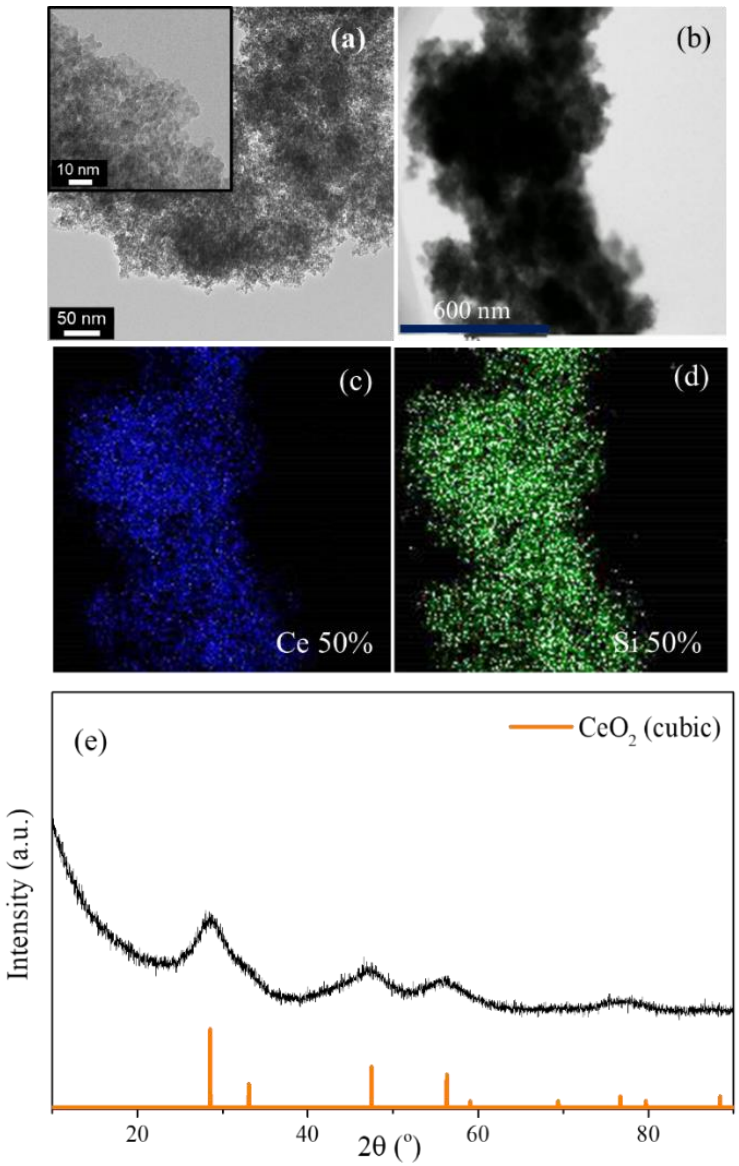

Figure 3.3. TEM image (a), STEM image (b), EDX mappings of Ce (c) and Si (d), and XRD pattern (e) of 0.5/SiO_2–CeO_2 NP composites. The reference peaks of JCPDS 00-004-0593 for CeO_2 are shown by the orange line.

Similar reactions using precursor solutions with different $Si(OEt)_4$:$Ce(NO_3)_3$ mole ratios also yielded the homogeneously mixed SiO_2–CeO_2 NP composites (Table 3.1, Figure 3.4). An almost linear correlation was observed between Si mole fraction in the precursor solutions and those in the obtained NP composites (Figure 3.5). The CeO_2 crystallite size dramatically

decreased in proportion to SiO_2 content in the SiO_2–CeO_2 NP composites (Figure 3.6). Consequently, the specific surface area of the obtained SiO_2–CeO_2 NP composites drastically increased with increased Si content (101–314 m^2/g, Table 3.1).

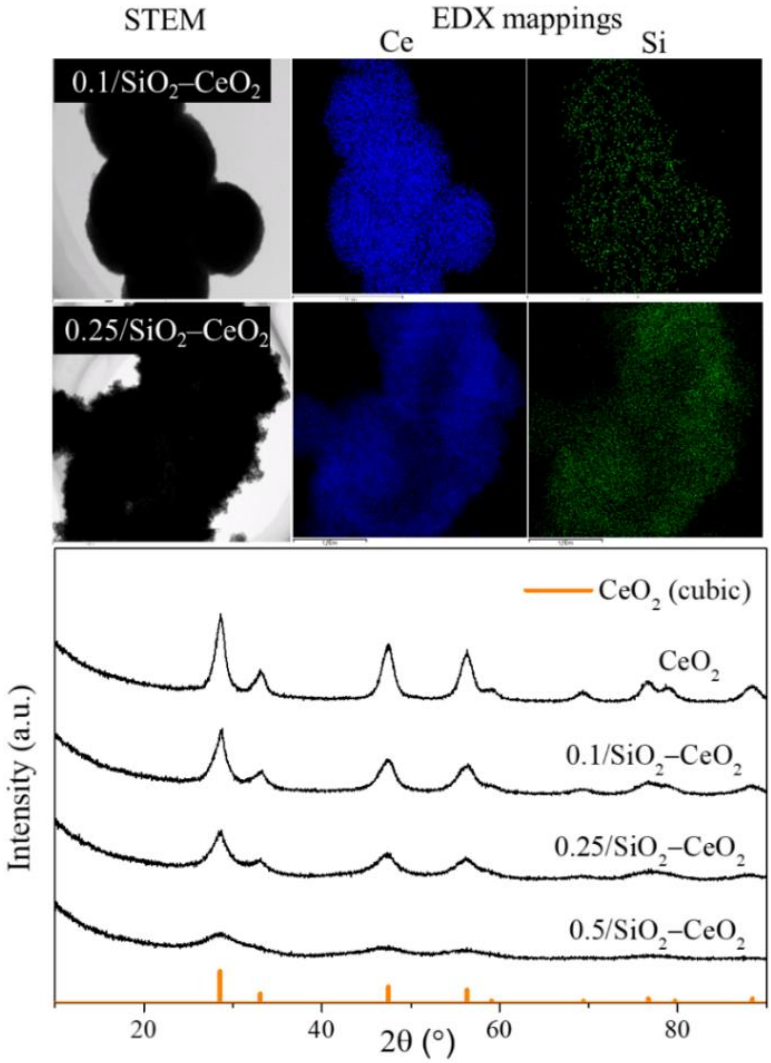

Figure 3.4. STEM images, EDX mappings of Ce and Si, and XRD patterns of 0.1/SiO_2–CeO_2 and 0.25/SiO_2–CeO_2 NP composites. The reference peaks of JCPDS 00-004-0593 for CeO_2 are shown by the orange line.

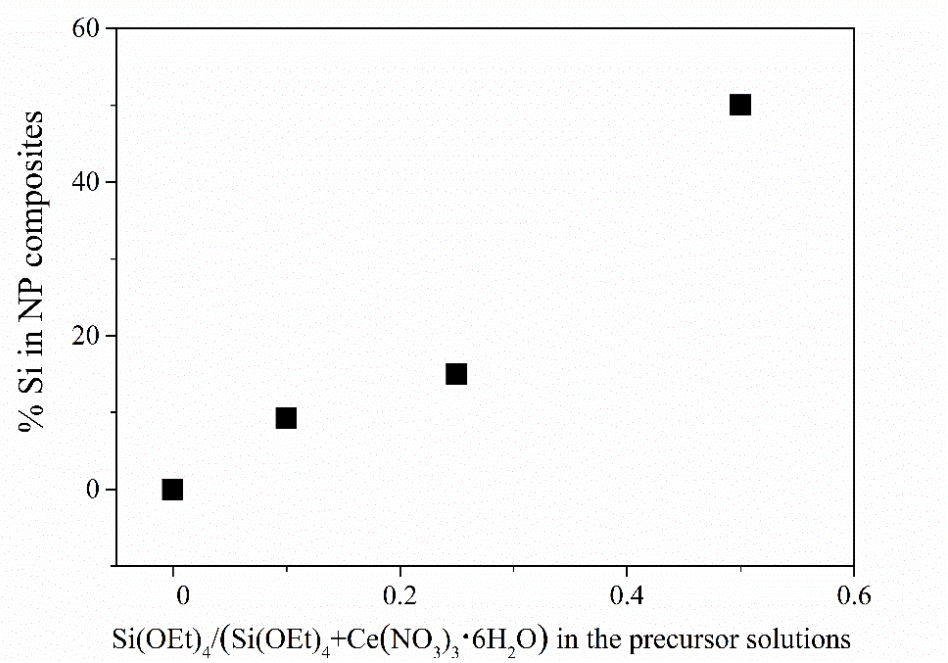

Figure 3.5. Plot of atomic fractions of Si in the SiO_2–CeO_2 composite NP assemblies estimated by EDX against the $Si(OEt)_4/(Si(OEt)_4 + Ce(NO_3)_3 \cdot 6H_2O)$ mole fractions in the precursor solutions (Table 3.1).

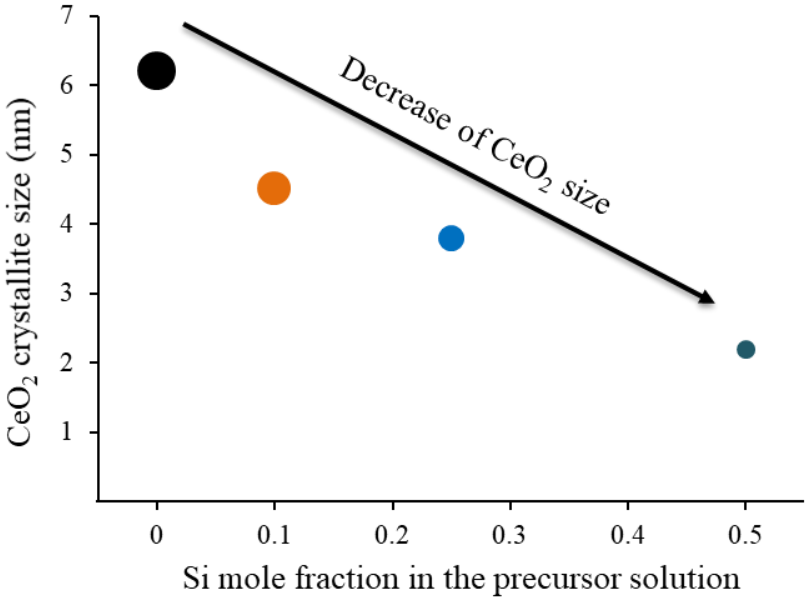

Figure 3.6. Dependence of the CeO_2 crystallite size on SiO_2 content in the SiO_2–CeO_2 NP composites.

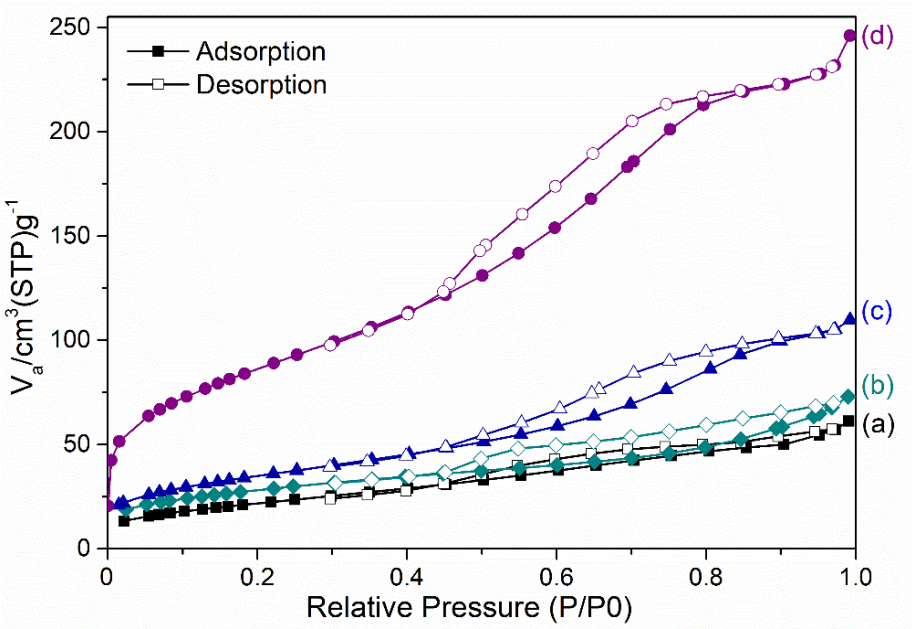

Figure 3.7. Nitrogen adsorption (closed symbols)/ desorption (open symbols) isotherms of the as-prepared composites: (a) CeO_2, (b) 0.1/SiO_2–CeO_2, (c) 0.25/SiO_2–CeO_2, and (d) 0.5/SiO_2–CeO_2.

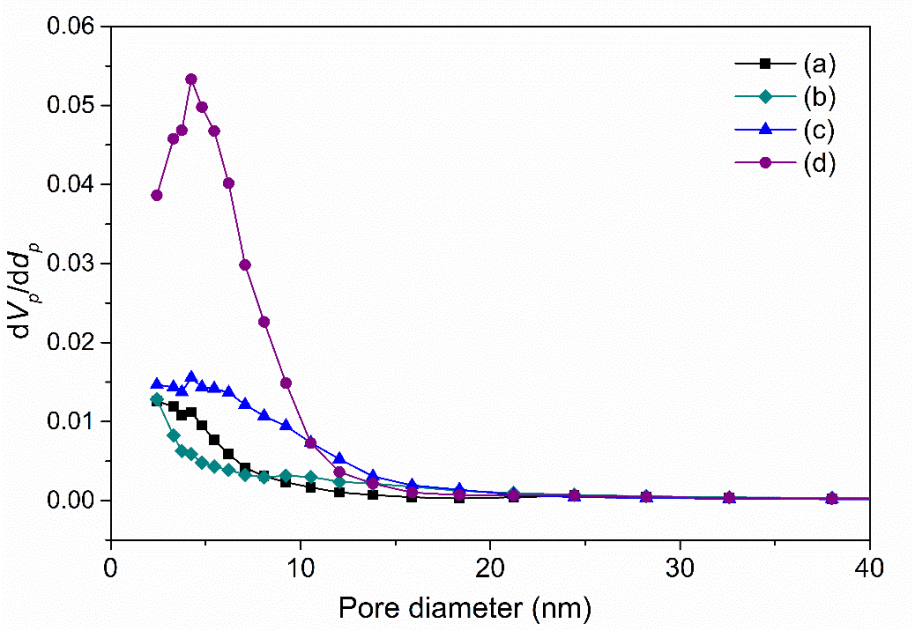

Figure 3.8. Barrett-Joyner-Halenda (BJH) pore size distribution plot of the as-prepared composites: (a) CeO_2, (b) 0.1/SiO_2–CeO_2, (c) 0.25/SiO_2–CeO_2, and (d) 0.5/SiO_2–CeO_2.

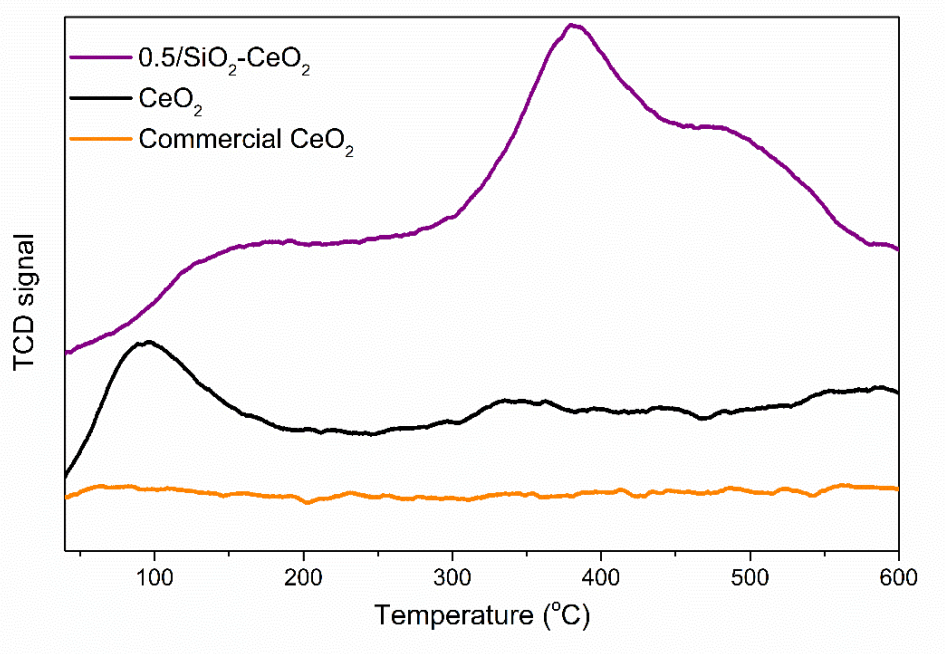

Figure 3.9. O_2-TPD profiles of the as-prepared SiO_2–CeO_2 (purple line), CeO_2 (black line), and commercial CeO_2 samples (orange line).

The nitrogen adsorption/desorption isotherms and pore size distributions shown in Figures 3.7 and 3.8, respectively, indicate mesoporous structure of the as-prepared SiO_2–CeO_2 composites with type IV isotherms. Small CeO_2 crystallite size [29,33] and large specific surface area[29,31,32] of SiO_2–CeO_2 composites, and a similar trend of decreasing CeO_2 crystallite size with increasing SiO_2 concentration[36] are also reported. However our synthetic procedure is so simple as compared with theirs, and, in our case, a large-scale synthesis would be possible by using autoclaves with larger volume or continuous reactors. In addition, preliminary experiments of O_2-TPD patterns of the prepared CeO_2 and 0.5/SiO_2–CeO_2 composites are so different (Figure 3.9), which could be ascribed to the effect of the SiO_2 domains in the SiO_2–CeO_2 composites.

Table 3.1. Yield, atomic% of Si, the crystallite size of CeO_2, specific surface area, and pore diameter of the as-prepared SiO_2–CeO_2 NP composites.

Sample[a]	Yield (%)	Atomic% of Si[b] Si/(Si+Ce)×100 (%)	CeO_2 crystallite size[c] (nm)	Specific surface area[d] (m^2/g)	Pore diameter[e] (nm)
CeO_2	73	0	6.2	81	<2.4[f]
0.1/SiO_2–CeO_2	91	9.2	4.5	101	<2.4[f]
0.25/SiO_2–CeO_2	95	15	3.8	127	4.2
0.5/SiO_2–CeO_2	82	49	2.2	314	4.2

[a]The numbers of 0.1, 0.25, and 0.5 denote the atomic fraction of Si to the total number of Si and Ce atoms in the precursor solutions.

[b]Evaluated by STEM/EDX analysis on TEM.

[c]The Scherrer equation was used to estimates crystallite size.

[d]The BET method was used.

[e]The BJH method was used.

[f]Too small to be estimated on the basis of the BJH method.

3.3.2. High heat tolerance of SiO_2–CeO_2 NP composites

Thermal stability of NPs is one of the most important properties for many applications, such as catalysis under high-temperature conditions. The obtained SiO_2–CeO_2 NP composites were calcined at an elevated temperature to evaluate their thermal stabilities. CeO_2 crystallite sizes were estimated by the Scherrer equation (Table 3.2, Figures 3.10 and 3.11). In the case of the prototype CeO_2 NP aggregates, the broad peaks changed to sharp ones as the calcination temperature was increased (Figure 3.10a), and the estimated crystallite size of 6.2 nm (as-prepared) became as large as 54 nm (1000 ºC) (Table 3.2). However, with increased SiO_2 content in the composites, the shapes of diffraction peaks remained broad, even after

calcination at high temperature (Figures 3.10b-d). It is worthwhile to mention that CeO_2 crystallite size in the 0.5/SiO_2–CeO_2 NP composites maintained a nanometer-order size of 4.4 nm, even after calcination at a temperature of 850 ºC for 3 h, indicating that the heat tolerance of the CeO_2 NPs in 0.5/SiO_2–CeO_2 NP composites was greatly improved.

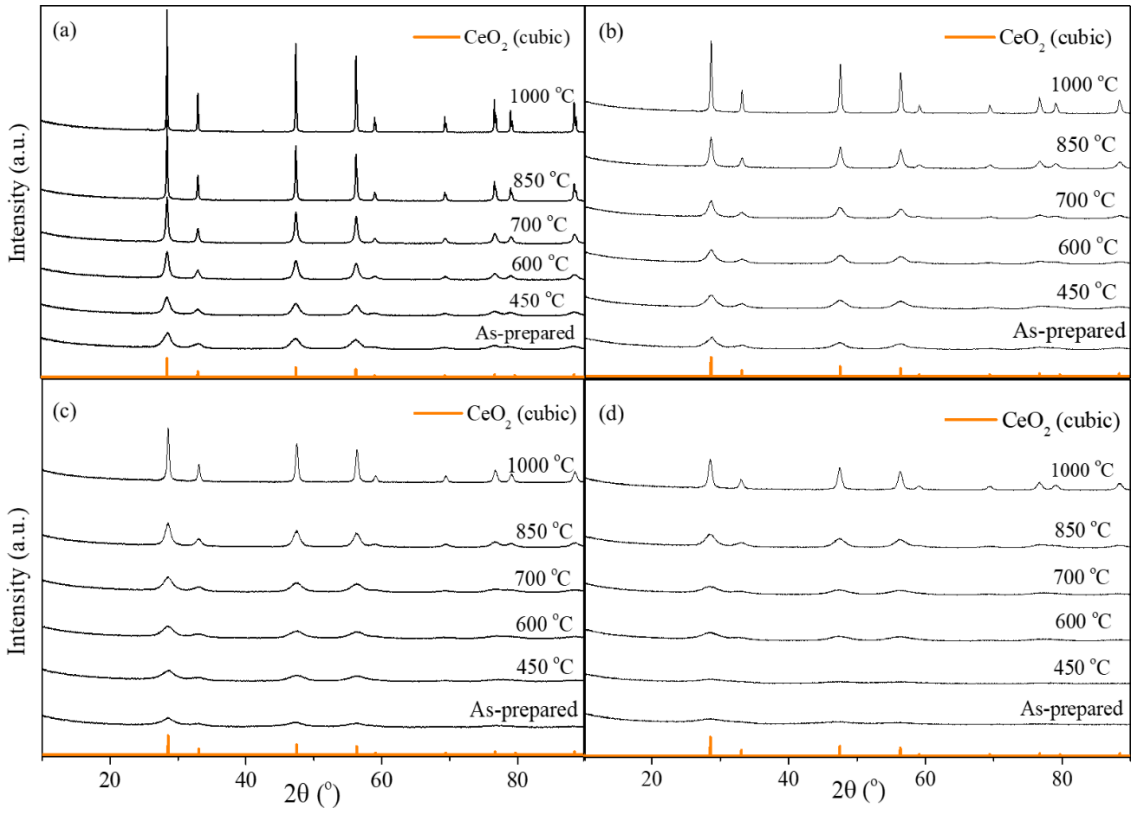

Figure 3.10. XRD patterns of (a) CeO_2, (b) 0.1/SiO_2–CeO_2, (c) 0.25/SiO_2–CeO_2, and (d) 0.5/SiO_2–CeO_2 calcined at different temperature for 3 h. The reference peaks of CeO_2 JCPDS 00-004-0593 are shown by the orange lines.

Interestingly, no XRD peak related to SiO_2 was observed, even after calcination at 1000 ºC for 3 h, suggesting that the SiO_2 present was purely amorphous in all the SiO_2–CeO_2 NP composites. Figure 3.11 summarizes the heat-tolerance enhancement of the primary CeO_2 NPs in the SiO_2–CeO_2 NP composites due to SiO_2 content. In particular, the primary CeO_2 NPs in the 0.5/SiO_2–CeO_2 NP composite exhibited excellent heat tolerance up to 850 ºC for 3 h

calcination.

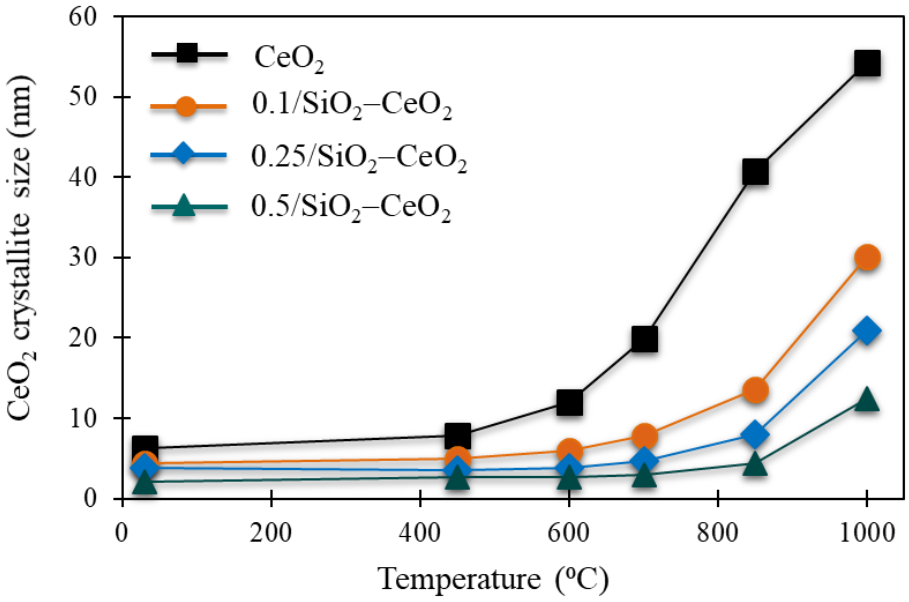

Figure 3.11. CeO_2 crystallite size change of SiO_2–CeO_2 NP composites as a function of calcination temperatures. Those values were calculated by using the Scherrer equation and were shown in Table 3.2. The samples were calcined for 3 h at different temperatures.

Table 3.2. Crystallite size of CeO_2 in SiO_2–CeO_2 NP composites calcined for 3 h at different temperatures.

Sample	**CeO_2 crystallite size[a] (nm)**					
	As-prepared	Calcined at 450 ºC	Calcined at 600 ºC	Calcined at 700 ºC	Calcined at 850 ºC	Calcined at 1000 ºC
CeO_2	6.2 (5.7 ± 1.1)	7.9 (5.5 ± 1.5)	12 (11.0 ± 1.9)	20 (–)	41 (–)	54 (–)
0.1/SiO_2–CeO_2	4.5 (4.9 ± 1.3)	5.0 (4.2 ± 0.7)	6.0 (6.2 ± 1.0)	7.9 (8.0 ± 1.9)	13.7 (15 ± 5)	30 (42 ± 13)
0.25/SiO_2–CeO_2	3.8 (4.3 ± 0.7)	3.6 (3.8 ± 0.8)	3.9 (4.4 ± 0.9)	4.7 (5.2 ± 0.9)	8.1 (8.0 ± 1.7)	21 (21 ± 5)
0.5/SiO_2–CeO_2	2.2 (2.7 ± 0.6)	2.0 (4.0 ± 0.9)	2.7 (3.0 ± 0.7)	3.1 (4.0 ± 0.8)	4.4 (4.7 ± 0.7)	13 (9.5 ± 1.4)

[a]The Scherrer equation was used to estimate crystallite size.

Mean values from TEM images of at least 40 primary particles are given in the parentheses.

The sintering phenomena of the SiO_2–CeO_2 NP composites were also directly checked by TEM observations (Figure 3.12). Particle sizes of CeO_2 in the CeO_2 aggregates and SiO_2–CeO_2 NP assemblies estimated directly from TEM images shown in parentheses in Table 3.2 are well consistent with CeO_2 crystallite sizes estimated by Scherrer equation using XRD patterns.

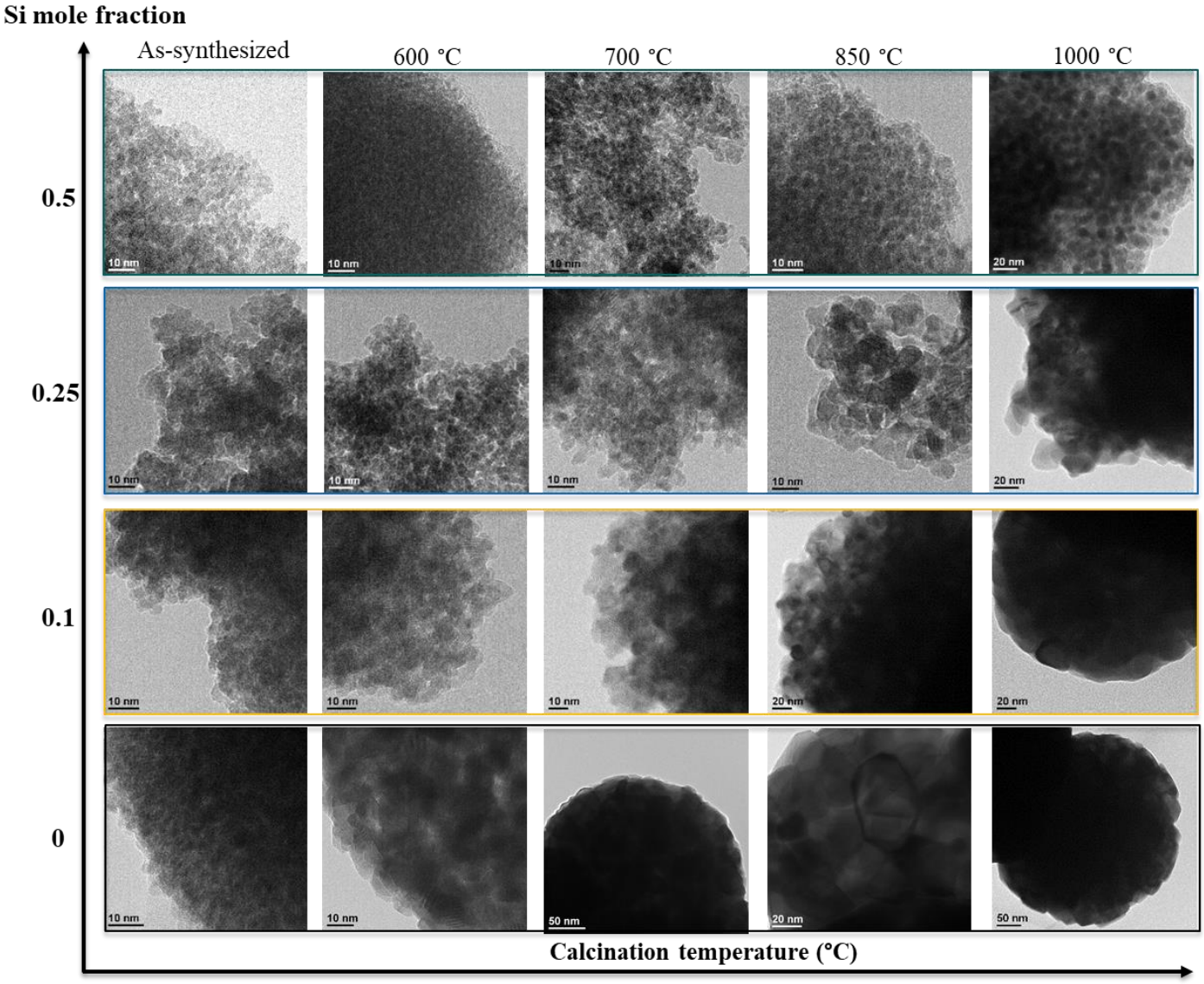

Figure 3.12. TEM images of the SiO_2–CeO_2 NP composites calcined at different temperatures for 3 h.

Table 3.3. Specific surface area of as-prepared and 3 h calcined CeO_2 NP aggregates and SiO_2–CeO_2 NP composites at different temperatures.

Sample	Specific surface area[a] (m^2/g)				
	As-prepared[b]	Calcined at 450 ºC	Calcined at 600 ºC	Calcined at 700 ºC	Calcined at 850 ºC
CeO_2	81	83	46	17	–[c]
0.1/SiO_2–CeO_2	101	104	69	44	17
0.25/SiO_2–CeO_2	127	130	118	94	49
0.5/SiO_2–CeO_2	314	182	149	161	49

[a]Evaluated by BET method.

[b]Same values to Table 1.

[c]Too small to be calculated.

High specific surface area of NP assemblies is also an essential property in many practical applications. Retention of high specific surface area of CeO_2 NPs, even under harsh high-temperature conditions, is an important problem to be solved. To determine the calcination temperature dependence of specific surface area, CeO_2 NP aggregates and SiO_2–CeO_2 NP composites were calcined (Table 3.3). When prototype CeO_2 NP aggregates were calcined, the specific surface area drastically decreased. This result is in sharp contrast to the SiO_2–CeO_2 NP composites, where the decrease of specific surface area was retarded by increasing the SiO_2 content in the SiO_2–CeO_2 NP composites. In the case of 0.5/SiO_2–CeO_2 NP composites, a large decrease of specific surface area was observed for calcination at 450 ºC, while only a small decrease was observed at higher temperatures up to 700 ºC, as expected. However, calcination at 850 ºC for 3 h decreased specific surface area to 49 m^2/g, indicating

that the conditions are too severe for 0.5/SiO_2–CeO_2 to maintain its porous structure. Thus, enhanced heat tolerance of 0.5/SiO_2–CeO_2 NP composites up to 700 ºC was also confirmed by means of the specific surface area changes.

3.3.3. Long-term heat tolerance of 0.5/SiO_2–CeO_2 NP composites

Besides the heat resistance of the material against deformation/sintering at high temperature, long-term thermal stability of the materials is also an important requirement, especially for the applications involving the high-temperature reactions. As discussed in the part 3.3.2, the 0.5/SiO_2–CeO_2 NP composites exhibited the excellent heat tolerance up to 850 ºC for 3 h with a slight growth of CeO_2 crystallites as compared to the CeO_2 agglomerates. Their long-term thermal stability was estimated through CeO_2 crystallite size changes at 700 ºC. In this experiment, the 0.5/SiO_2–CeO_2 composites were kept in the furnace at 700 ºC for different time intervals varied from 3 to 72 h, respectively. The change of CeO_2 crystallite size and specific surface area at the different calcination time of the 0.5/SiO_2–CeO_2 NP composites were given in Table 3.4. XRD patterns and TEM images of those calcined sample were presented in Figures 3.13 and 3.14, respectively.

As shown in Figure 3.13a, peaks in the XRD profiles of 0.5/SiO_2–CeO_2 NP composites became slightly broader, however no drastic change was observed in TEM images of the calcined SiO_2–CeO_2 NP composites until 72 h of calcination (Figures 3.14a-f). Indeed, the estimated CeO_2 crystallite sizes by both XRD and TEM changed slightly from approximately 2 nm to the 3–4 nm range, even after 72 h calcination at 700 ºC (Table 3.4 and Figure 3.13b). In addition, specific surface area remained at 105 m^2/g, even after 72 h calcination at 700 ºC. Therefore, I succeeded in suppressing the sintering of the CeO_2 NPs using a simple approach of mixing CeO_2 NPs and SiO_2 NPs homogeneously.

Table 3.4. CeO_2 crystallite size and specific surface area of the as-prepared and the calcined 0.5/SiO_2–CeO_2 NP composites.

Calcination time[a] (h)	CeO_2 crystallite size[b] (nm)	Specific surface area[c] (m^2/g)
As-prepared	2.2 (2.7 ± 0.6)	314
3	3.1 (4.0 ± 0.8)	161
6	3.1 (3.7 ± 0.7)	140
12	3.2 (3.5 ± 0.7)	122
24	3.5 (3.7 ± 0.8)	117
72	3.4 (3.3 ± 0.5)	105

[a]Sample was calcined at 700 °C for different time intervals.

[b]The Scherrer equation was used to estimate crystallite size. Mean value from TEM images at least 40 primary particles are given in the parentheses.

[c]Calculated by the BET method.

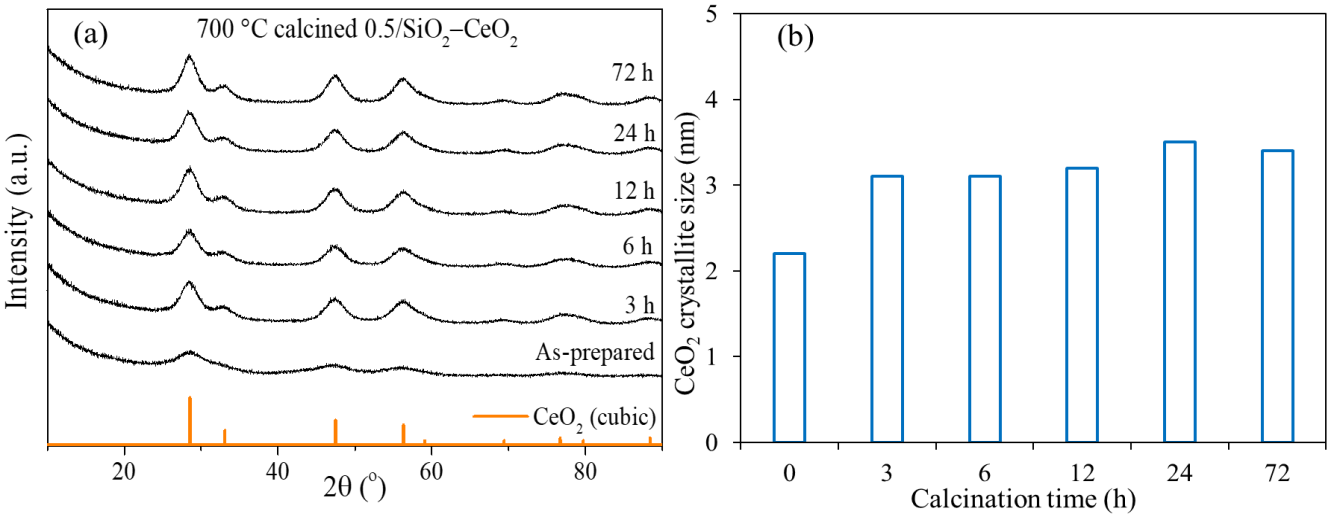

Figure 3.13. (a) XRD patterns and (b) CeO_2 crystallite size of as-prepared and calcined 0.5/SiO_2–CeO_2 NP composites. The reference peaks of JCPDS 00-004-0593 for CeO_2 are shown by the orange line.

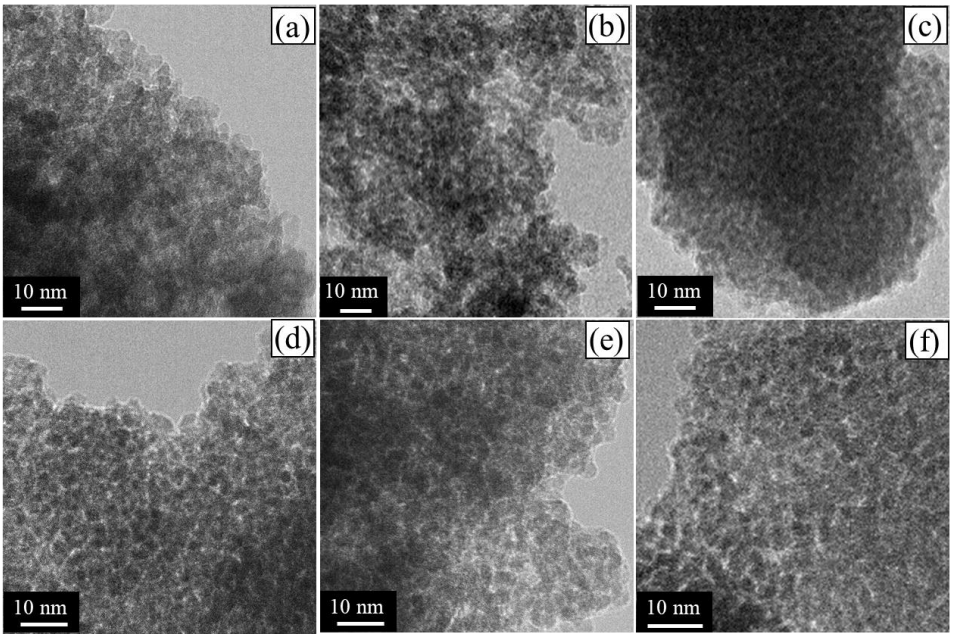

Figure 3.14. TEM images of 0.5/SiO_2–CeO_2 NP composites: (a) as-prepared, and calcined for (b) 3 h, (c) 6 h, (d) 12 h, (e) 24 h, and (f) 72 h at 700 ºC. The reference peaks of JCPDS 00-004-0593 for CeO_2 are shown by the orange line.

3.3.4. A mechanism of high heat tolerance of SiO_2–CeO_2 NP composites

To confirm the high heat tolerance of SiO_2–CeO_2 NP composites, in which primary CeO_2 NPs are embedded in amorphous SiO_2, TEM observations of completely sintered 0.5/SiO_2–CeO_2 NP composites after calcination under harsh conditions at 1000 ºC for 3 h were performed (Figure 3.15). As shown in Figures 3.15a and 3.15b, the calcined 0.5/SiO_2–CeO_2 NP composites consist of inhomogeneous dark and bright areas, forming a domain structure that would be ascribed to CeO_2 NPs and amorphous SiO_2 matrix, respectively. The observation of the inhomogeneous domain structure clearly indicates phase separation of the SiO_2 and CeO_2 domains from the SiO_2–CeO_2 NP composites (Figure 3.16). The size of CeO_2 domains,

corresponding to darker spots, increased to 9.5 nm (TEM) after high-temperature calcination at 1000 ºC for 3 h (Table 3.2). A similar phenomenon was also observed by Dunne et al. when CeO_2–SiO_2 materials were heated up to 900 ºC.[29] Thus, TEM observations strongly support the sintering resistance mechanism of SiO_2–CeO_2 NP composites.

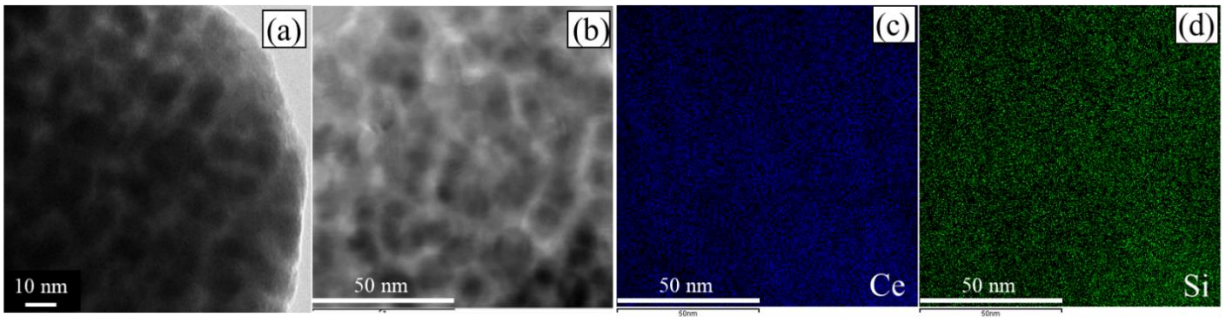

Figure 3.15. (a) TEM image, (b) STEM image, and (c, d) EDX mappings of 0.5/SiO_2–CeO_2 composite NP assemblies calcined at 1000 ºC for 3 h.

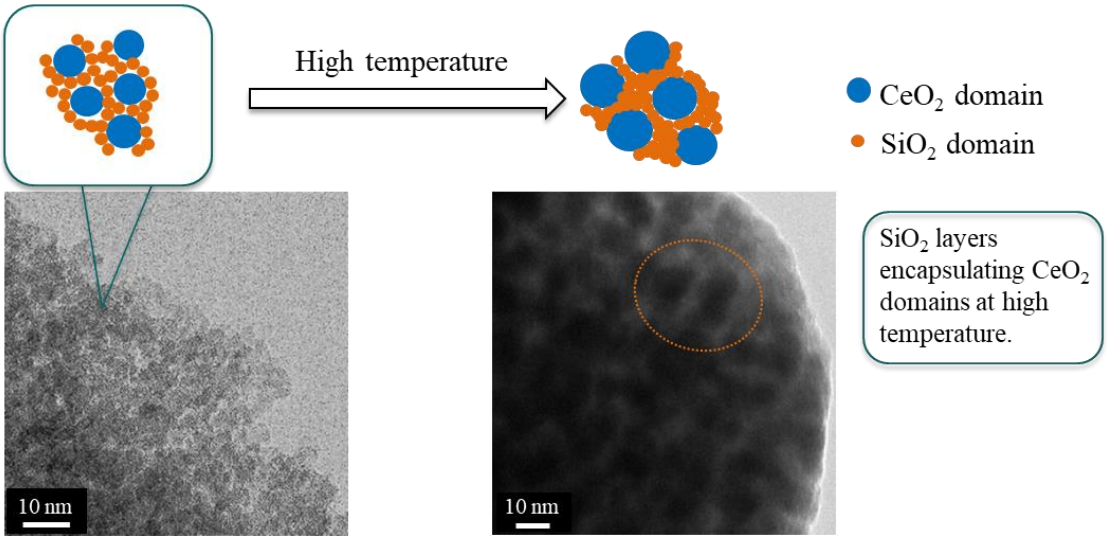

Figure 3.16. Mechanism of high heat tolerance of SiO_2–CeO_2 NP composite. The TEM images of as-prepared and calcined at 1000 ºC 0.5/SiO_2–CeO_2 NP composite.

3.4. Conclusion

We provided a novel solvothermal method to yield ultrafine SiO_2–CeO_2 NP composites with large surface areas and excellent heat tolerance of CeO_2 NPs. The Si:Ce ratios in the SiO_2–CeO_2 NP composites were freely controllable with mole fraction of Si to total mole number of Si and Ce varied from 0 to 0.5 in the precursor solutions. Along with the increase of SiO_2 content in the SiO_2–CeO_2 NP composites, the primary particle size of the resultant CeO_2 NPs became remarkably small, and their specific surface area drastically increased. In the 0.5/SiO_2–CeO_2 NP composites, a 2.2 nm (XRD) primary particle size of the resultant CeO_2 NPs and 314 m^2/g in the specific surface area were achieved. Heat tolerance of the primary CeO_2 NPs was dramatically enhanced by mixing with SiO_2, where only slight enlargement of the primary CeO_2 NPs was observed, even after calcination under the harsh high-temperature conditions of 850 ºC for 3 h and at 700 ºC for 72 h.

Reference

[1] M. Manto, P. Xie, C. Wang, Catalytic dephosphorylation using ceria nanocrystals, *ACS Catal.* **2017,** *7*, 1931–1938.

[2] I. Soykal, H. Sohn, D. Singh, J. Miller, U. Ozkan, Reduction Characteristics of Ceria under Ethanol Steam Reforming Conditions: Effect of the Particle Size, *ACS Catal.* **2014,** *4*, 585–592.

[3] C. Sun, H. Li, L. Chen, Nanostructured ceria-based materials: synthesis, properties, and applications, *Energy Environ. Sci.* **2012**, *5*, 8475–8505.

[4] K. Suzuki, A. Sinha, Monodisperse, bimodal mesoporous ceria catalysts and adsorbents for air purification, *J. Mater. Chem.* **2007**, *17*, 2547–2551.

[5] L. Zhong, J. Hu, A. Cao, Q. Liu, W.G. Song, L. Wan, 3D flowerlike Ceria micro/nanocomposite structure and its application for water treatment and CO removal, *Chem. Mater.* **2007**, *19*, 1648–1655.

[6] C. Walkey, S. Das, S. Seal, J. Erlichman, K. Heckman, L. Ghibelli, E. Traversa, J. McGinnis, W. Self, Catalytic properties and biomedical applications of cerium oxide nanoparticles, *Environ. Sci.: Nano* **2015**, *2*, 33–53.

[7] G. Mullen, E. Evans, I. Sabzevari, B. Long, K. Alhazmi, B. Chandler, C. Mullins, Water influences the activity and selectivity of ceria-supported gold catalysts for oxidative dehydrogenation and esterification of ethanol, *ACS Catal.* **2017**, *7*, 1216–1226.

[8] N. Nelson, S. Manzano, A. Sadow, S. Overbury, I. Slowing, Selective hydrogenation of phenol catalyzed by palladium on high-surface-area ceria at room temperature and ambient pressure, *ACS Catal.* **2015**, *5*, 2051–2061.

[9] M. Tamura, T. Kitanaka, Y. Nakagawa, K. Tomishige, Cu sub-nanoparticles on Cu/CeO_2 as an effective catalyst for methanol synthesis from organic carbonate by hydrogenation, *ACS Catal.* **2016**, *6*, 376–380.

[10] P. Dutta, M. Seehra, Y. Shi, E.M. Eyring, R. Ernst, Concentration of Ce^{3+} and oxygen vacancies in cerium oxide nanoparticles, *Chem. Mater.* **2006**, *18*, 5144–5146.

[11] Y. Li, Q. Sun, M. Kong, W. Shi, J. Huang, J. Tang, X. Zhao, Coupling oxygen ion conduction to photocatalysis in mesoporous nanorod-like ceria significantly improves photocatalytic efficiency, *J. Phys. Chem. C* **2011**, *115*, 14050–14057.

[12] N. Sutradhar, A. Sinhamahapatra, S. Pahari, M. Jayachandran, B. Subramanian, H. Bajaj, A. Panda, Facile low-temperature synthesis of ceria and samarium-doped ceria nanoparticles and catalytic allylic oxidation of cyclohexene, *J. Phys. Chem. C* **2011**, *115*, 7628–7637.

[13] T. Montini, M. Melchionna, M. Monai, P. Fornasiero, Fundamentals and catalytic

applications of CeO_2-based materials, *Chem. Rev.* **2016**, *116*, 5987–6041.

[14] B. Choudhury, P. Chetri, A. Choudhury, Oxygen defects and formation of Ce3+ affecting the photocatalytic performance of CeO_2 nanoparticles *RSC Adv.* **2014**, *4*, 4663–4671.

[15] J. Wang, J. Wen, M. Shen, Effect of interaction between $Ce_{0.7}Zr_{0.3}O_2$ and Al_2O_3 on structural characteristics, thermal stability, and oxygen storage capacity, *J. Phys. Chem. C* **2008,** *112*, 5113–5122.

[16] Z. Ying, X. Chenjun, S. Yeqing, Z. Qiuliang, C. Yinfei, L. Hanfeng, Thermal stability of M_nO_x–CeO_2 mixed oxide for soot combustion: influence of Al_2O_3, TiO_2, and ZrO_2 carriers, *RSC Adv.* **2015**, *5*, 91734–91741.

[17] S. Lee, J. Seo, W. Jung, Sintering-resistant Pt@CeO_2 nanoparticles for high-temperature oxidation catalysis, *Nanoscale* **2016**, *8*, 10219–10228.

[18] K. Yoon, Y. Yang, P. Lu, D. Wan, H. Peng, K. Masias, P. Fanson, C. Campbell, Y. Xia, A highly reactive and sinter-resistant catalytic system based on platinum nanoparticles embedded in the inner surfaces of CeO_2 hollow fibers, *Angew. Chem. Int. Ed.* **2012**, *51*, 9543–9546.

[19] M. Asadullah, T. Miyazawa, S. Ito, K. Kunimori, K. Tomishige, Catalyst performance of Rh/CeO_2/SiO_2 in the pyrogasification of biomass, *Energy Fuels* **2003**, *17*, 842–849.

[20] G. Bouala, N. Clavier, S. Martin, J. Léchelle, J. Favrichon, H.P. Brau, N. Dacheux, R. Podor, From in situ HT-ESEM observations to simulation: how does polycrystallinity affects the sintering of CeO_2 microspheres?, *J. Phys. Chem. C* **2016**, *120*, 386–395.

[21] J. Li, T. Ikegami, J. Lee, T. Mori, Characterization and sintering of nanocrystalline CeO_2 powder synthesized by a mimic alkoxide method, *Acta. Mater.* **2001**, *49*, 419–426.

[22] S.J. Schmieg, D.N. Belton, Effect of hydrothermal aging on oxygen storage/release and activity in a commercial automotive catalyst, *Appl. Catal. B-Environ.* **1995**, *6*, 127–144.

[23] P. Wang, K. Ueno, H. Takigawa, K. Kobiro, Versatility of one-pot, single-step synthetic

approach for spherical porous (metal) oxide nanoparticles using supercritical alcohols, *J. Supercrit. Fluid* **2013**, *78*, 124–131.

[24] P. Wang, K. Yokoyama, T. Konishi, N. Nishiwaki, K. Kobiro, Ultimately simple one-pot single-step synthesis of rare earth doped spherical mesoporous metal oxide nanospheres with upconversion emission ability in supercritical methanol, *J. Supercrit. Fluid* **2013**, *80*, 71–77.

[25] P. Wang, K. Kobiro, Synthetic versatility of nanoparticles: A new, rapid, one-pot, single-step synthetic approach to spherical mesoporous (metal) oxide nanoparticles using supercritical alcohols, *Pure Appl. Chem.* **2014**, *86*, 785–800.

[26] E. K. C. Pradeep, M. Ohtani, K. Kobiro, A simple synthetic approach to Al_2O_3–TiO_2 and ZnO–TiO_2 mesoporous hollow composite assemblies consisting of homogeneously mixed primary particles at the nano level, *Eur. J. Inorg. Chem.* **2015**, *2015*, 5621–5627.

[27] E. K. C. Pradeep, T. Habu, H. Tooriyama, M. Ohtani, K. Kobiro, Ultra-simple synthetic approach to the fabrication of CeO_2–ZrO_2 mixed nanoparticles into homogeneous, domain, and core–shell structures in mesoporous spherical morphologies using supercritical alcohols, *J. Supercrit. Fluid* **2015**, *97*, 217–223.

[28] H. T. T. Nguyen, T. Habu, M. Ohtani, K. Kobiro, One-step direct synthesis of SiO_2–TiO_2 composite nanoparticle assemblies with hollow spherical morphology, *Eur. J. Inorg. Chem.* **2017**, *2017*, 3017–3023.

[29] P. Dunne, A. Carnerup, A. Węgrzyn, S. Witkowski, R.I. Walton, Hierarchically structured ceria-silica: synthesis and thermal properties, *J. Phys. Chem. C* **2012**, *116*, 13435–13445.

[30] B. Reddy, A. Khan, Y. Yamada, T. Kobayashi, S. Loridant, J.C. Volta, Surface Characterization of CeO_2/SiO_2 and $V_2O_5/CeO_2/SiO_2$ catalysts by Raman, XPS, and other techniques, *J. Phys. Chem. B* **2002**, *106*, 10964–10972.

[31] N. Pal, E. Cho, D. Kim, Synthesis of ordered mesoporous silica/ceria–silica composites and their high catalytic performance for solvent-free oxidation of benzyl alcohol at room temperature, *RSC Adv.* **2014**, *4*, 9213–9222.

[32] E. Cho, S. Yim, D. Kim, M. Jaroniec, Surfactant-assisted synthesis of mesoporous silica/ceria–silica composites with high cerium content under basic conditions, *J. Mater. Chem. A* **2013**, *1*, 12595–12605.

[33] B. Reddy, A. Khan, P. Lakshmanan, M. Aouine, S. Loridant, J.C. Volta, Structural characterization of nanosized CeO_2–SiO_2, CeO_2–TiO_2, and CeO_2–ZrO_2 catalysts by XRD, Raman, and HREM techniques, *J. Phys. Chem. B* **2005**, *109*, 3355–3363.

[34] A. Patterson, The Scherrer formula for X-ray particle size determination, *Phys. Rev.* **1939**, *56*, 978–982.

[35] M. Lin, Z. Fu, H. Tan, J. Tan, E. Teo, Hydrothermal synthesis of CeO_2 nanocrystals: Ostwald ripening or oriented attachment, *Cryst. Growth Des.* **2012**, *12*, 3296–3303.

[36] J. Mao, Y. Bai, L. Gu, P.A. Aken, M.J. Tu, Preparation and characterization of size-controlled CeO_2 nanoparticles coated with SiO_2, *J. Nanopart. Res.* **2010**, *12*, 2045–2049.

CHAPTER IV.

CeO_2 Nanocomposites for Sintering-Resistant Catalyst Supports

4.1. Introduction

A number of studies have been focused on utilizing various kinds of metal oxide and mixed oxide nanomaterials for catalytic processes due to the excellent catalytic activity of these materials. In the catalytic systems, active metal NPs dispersed on the oxides or mixed oxide supports are widely used for a wide variety of reactions. However, as a critical issue of the catalysts, a loss of catalytic activity of the catalysts over time occurs certainly for most catalytic processes. Among those reasons of catalyst activity loss/deactivation, thermal sintering of metal NPs and the thermal deformation of catalyst supports in supported catalysts are critical issues in practice, especially when catalysts are applied to high-temperature catalytic processes.[1–3] In general, nano-sized metal particles and their supports tend to migrate under severe reaction conditions, such as high temperature, generating enlarged agglomerates with a morphological change as well as losing their surface area and catalytic activity.[4–7] Therefore, it is crucial to retain the original size and morphology of both metal nanoparticles and catalyst supports. Several anti-sintering strategies in both chemical and physical approaches, for example, alloying, ligand-assisted pinning, encapsulation (e.g., core-shell and core-sheath), and fixing metal nanoparticles on defects of catalyst supports, have been investigated.[8–14] These strategies, however, are still in progress.

Considering the long-term usability of the supported catalysts, not only the catalytic activity and tolerance of the active metal catalysts but those of the oxide supports should be considered as important factors. As previously mentioned, the NP assemblies of mono-component oxides as well as their mixed oxides were prepared by the one-pot and single-step

solvothermal approach. The obtained MARIMO assemblies consist of an ultrafine nano-concave–convex surface with a huge surface area.[15–17] For example, the TiO_2 MARIMO assembly consists of numerous primary nanoparticles with ca. 5 nm diameter, and the specific surface area exceeds 200 m^2/g and reaches 400 m^2/g. Therefore, the TiO_2 MARIMO assembly with its large specific surface area and nano-concave–convex surface structure is expected to be an excellent support for catalyst metal nanoparticles, because the nano-concave–convex surface structure can disperse metal nanoparticles well and prevent metal nanoparticles from migrating to aggregates. Indeed, the use of the TiO_2 MARIMO assembly as a catalyst support successfully enhanced the dispersion of Au nanoparticles on the surface and suppressed the sintering of Au nanoparticles during highly exothermic CO oxidation.[18] However, the heat tolerance of the TiO_2 support turned out to be insufficient in this reaction, and the support gradually started to be sintered, which impelled us to study better supports with higher heat tolerance.

Among metal oxides utilized for catalytic applications, CeO_2 is an attractive material because of its high and unique catalytic activity derived from Ce^{3+}/Ce^{4+} redox change.[19–26] Additionally, a possible strong interaction between CeO_2 and metal nanoparticles such as Ru, Pd, and Pt would enhance metal dispersion, catalytic efficiency, and suppression of migration of active metal nanoparticles.[27–33] Moreover, the properties of CeO_2 can be tuned or enhanced by mixing with other metal oxides at a nano-level to yield CeO_2 nanocomposites. In chapter III, I mentioned that the SiO_2–CeO_2 nanocomposites with a 1 : 1 Si:Ce mole ratio exhibited a large specific surface area exceeding 300 m^2/g, as well as excellent heat tolerance with almost no serious damage under heating at either 700 °C for 24 h or 850 °C for 3 h, compared to monocomponent CeO_2.[34] With these advantages, CeO_2 assemblies and CeO_2 nanocomposites with ultrafine surface roughness, which are synthesized by our original solvothermal synthesis method, are highly expected to be effective and sintering-resistant catalyst supports, especially

when the reaction is performed at an elevated temperature (Figure 4.1).

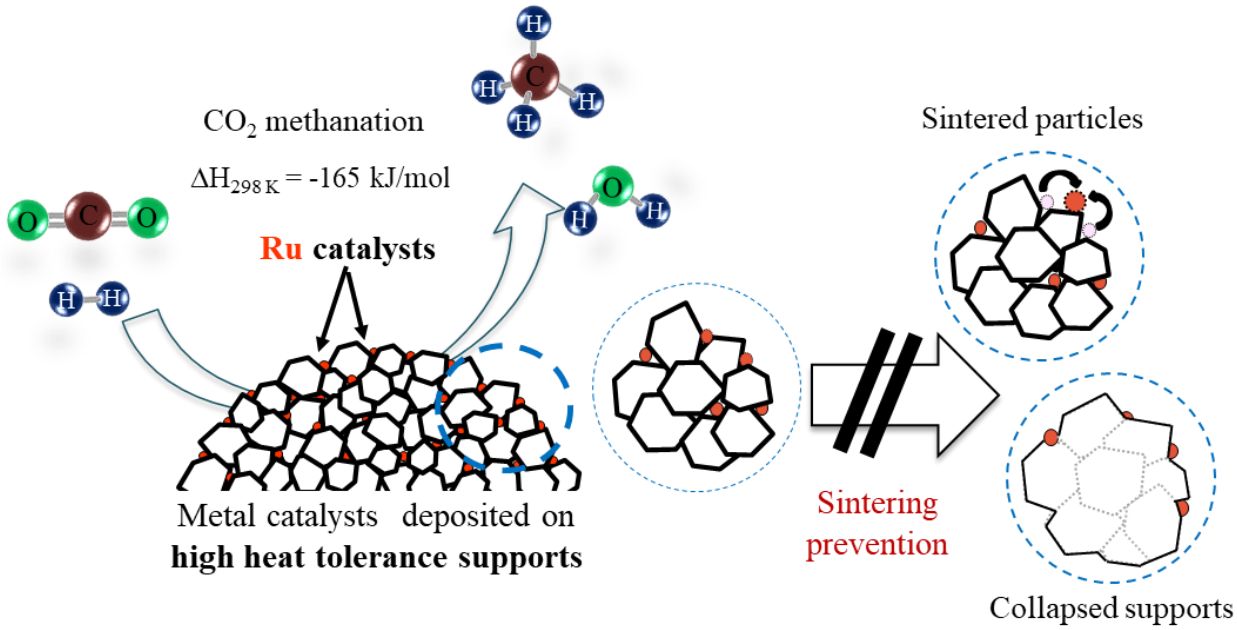

Figure 4.1. A proposed sintering-prevention of the supported catalyst on large surface area and high heat tolerance supports.

In this Chapter, we report the heat tolerance of the prepared CeO_2-based materials, as sintering-resistant supports, including CeO_2 assemblies, SiO_2–CeO_2 nanocomposites, and TiO_2–CeO_2 nanocomposites. Methanation of CO_2 by H_2 catalyzed by Ru, which is one of the most important reactions for CO_2 recycling.[35–37] was selected as a probe reaction to estimate sintering resistance of the catalysts, since the reaction is known as a highly exothermic reaction (Eq.1).

$$CO_2 + 4H_2 \longrightarrow CH_4 + 2H_2O \quad \Delta H_{298K} = -165 \text{ kJ/mol} \qquad \text{(Eq.1)}$$

When the methanation is performed in a small scale, temperature control of the catalyst bed is relatively easy because of small amount of generated reaction heat from the exothermic

reaction. However, in the case of large scale reaction, such as bench-top scale or more, total amount of the reaction heat is quite much. In this case, temperature control of the catalyst bed becomes seriously important. If the methanation reaction meet “runaway (out of control)” accidentally, the catalysts will be exposed to high temperature, which surely leads to sintering of the catalyst Ru nanoparticles. Once sintering of the Ru nanoparticles occurs, catalytic activity will be lost and no recovery can be expected even after the catalyst bed temperature is lowered. In order to avoid such catastrophic situation, the reactant gases are sometimes diluted by inert gas or the reactor is cooled from the outside not to reach such high temperature, which need more cost practically. Then, if the catalysts for the exothermic reactions could tolerate such accidental and/or unexpected temperature jump, it would be very meaningful to realize sintering-resistant catalytic systems. Thus, for exothermic CO_2 methanation, sintering suppression of the supported metal nanoparticle catalyst under unexpected high temperature conditions is extremely important in order to keep the catalysts stable.

4.2. Experimental Section

4.2.1. Materials

Methanol, cerium nitrate hexahydrate ($Ce(NO_3)_3 \cdot 6H_2O$), tetraethyl orthosilicate ($Si(OEt)_4$), titanium tetraisopropoxide ($Ti(O^iPr)_4$), sodium hydroxide (NaOH), ruthenium chloride trihydrate ($RuCl_3 \cdot 3H_2O$), *N,N,N′,N′*-tetramethylethylenediamine ($(CH_3)_2NCH_2CH_2N(CH_3)_2$, TMEDA), commercial cerium oxide (commercial CeO_2), and washed sea sand (425~850 μm) were purchased from FUJIFILM Wako Pure Chemical Corporation. All chemicals were used as received without further purification.

4.2.2. Preparation of the CeO_2 Assembly, SiO_2-CeO_2 Nanocomposite, and TiO_2-CeO_2 Nanocomposite

Synthesis of the CeO_2 assembly and SiO_2−CeO_2 nanocomposite was carried out by the solvothermal reaction of a precursor solution including $Ce(NO_3)_3 \cdot 6H_2O$ (0.1 mol/L), $Si(OEt)_4$ (0.1 mol/L), and TMEDA (0.2 mol/L) in methanol (3.5 mL) at 300 °C according to a similar procedure described in Chapter III. The TiO_2–CeO_2 nanocomposite with a 1:1 molar ratio of Ti/Ce was prepared by a similar procedure using $Ti(O^iPr)_4$ instead of $Si(OEt)_4$.

4.2.3. Preparation of Ru Catalysts

Supported Ru catalysts were prepared by the precipitation–deposition method with an intended Ru amount of 3 wt%. The powdery support (1 g, commercially available and solvothermally prepared) was dispersed in 27 mL of reverse osmosis water prior to the addition of 80 mg of $RuCl_3 \cdot 3H_2O$. NaOH solution (0.1 mol/L) was added slowly to the suspension with vigorous stirring to adjust the pH to 8.0~8.5. The mixture was vigorously stirred for another 3 h, and then the mixture was centrifuged. The obtained precipitate was collected and washed three times with water and dried at 60 °C for 12 h in an oven. The obtained powdery product was reduced in a mixed gas stream of H_2 and N_2 (40% H_2 and 60% N_2) at 200 °C for 3 h. The obtained 3 wt% Ru catalysts supported on the commercial CeO_2 assembly, solvothermally prepared CeO_2 assembly, solvothermally prepared SiO_2–CeO_2 nanocomposite, and solvothermally prepared TiO_2–CeO_2 nanocomposite are denoted as Ru/commercial CeO_2, Ru/CeO_2, Ru/SiO_2–CeO_2, and Ru/TiO_2–CeO_2, respectively.

4.2.4. Characterization

Transmission electron microscopy (TEM) images were taken using a JEOL JEM-2100F

microscope. High-angle annular dark-field scanning TEM (HAADF-STEM) and energy-dispersive X-ray spectroscopy (EDX) were performed on an Oxford INCA X-Max 80 EDX spectrometer with the above TEM instrument. Nitrogen (N_2) adsorption/desorption experiments were conducted on a MicrotracBEL BELSORP-mini II. The specific surface area was calculated using the Brunauer–Emmett–Teller (BET) method through obtained N_2 adsorption–desorption isotherms. The crystalline phases of the resultant nanoparticle nanocomposites were identified by X-ray diffraction (XRD) on a Rigaku SmartLab diffractometer using graphite-monochromated Cu Kα radiation. Hard X-ray photoelectron spectroscopy (HAXPES) measurements were performed at BL15XU of SPring-8. The excitation photon energy was fixed to 5.95 keV, and the total energy resolution was set to 240 meV.

The reducibility of these prepared catalysts was studied by temperature-programmed reduction of hydrogen (H_2-TPR) with a flow-type reactor (BELCAT II; MicrotracBEL). The catalysts (50 mg) were pretreated in a mixed gas flow of O_2/Ar (20% O_2 and 80% Ar) at 300 °C for 30 min prior to H_2-TPR. The H_2-TPR experiment was executed in a temperature range of 40–900 °C, with a ramping rate of 10 °C/min, in a mixed gas of 6% H_2 in Ar.

Pulsed chemisorption using CO gas (CO chemisorption) was carried out to characterize the Ru active sites of the catalysts. 100 mg of the catalysts was pretreated by H_2 at 120 °C for 15 min prior to CO adsorption with a mixed stream of 5% CO in He at room temperature.

4.2.5. Evaluation of Catalytic Activity

The catalytic activity of the Ru catalysts for CO_2 methanation was tested using the flow-type reactor (BELCAT II; MicrotracBEL). Before performing the reaction, the catalyst sample (100 mg) diluted by the washed sea sand (100 mg) was packed into the reactor and then

pretreated under a H_2 stream at 120 °C for 15 min. Then, CO_2 methanation was conducted by feeding an inlet gas stream of $CO_2/H_2/Ar$ (5% CO_2, 20% H_2, and 75% Ar) at a total flow rate of 20 mL/min. The outlet gases were analyzed by a gas chromatograph (GC3200; GL Sciences) using a thermal conductivity detector.

The stability and durability of the catalysts against sintering were evaluated through three different experiments: three-run test, 10-cycle test, and long-term stability test. In these catalytic tests, the reaction processes were sequentially repeated several times or constantly kept under high temperature conditions. For the three-run test, the whole CO_2 methanation process in a temperature range of 150–600 °C was sequentially repeated three times. The temperature step and the reaction time at each temperature were kept at 50 °C and for 30 min, respectively. The 10-cycle test was carried out by repeating CO_2 methanation 10 times at a low temperature of 50 °C and a high temperature of 300 °C alternately (Figure 4.2). In each cycle of the 10-cycle test, the reaction time was kept at 30 min at each temperature. The long-term stability test was performed over a period of 24 h at a constant temperature of 400 °C. In the cases of the three-run test and the 10 cycle test, 100 mg of catalysts were used, while 25 mg of catalysts were used in the long-term stability test in expectation of earlier activity loss of the catalysts.

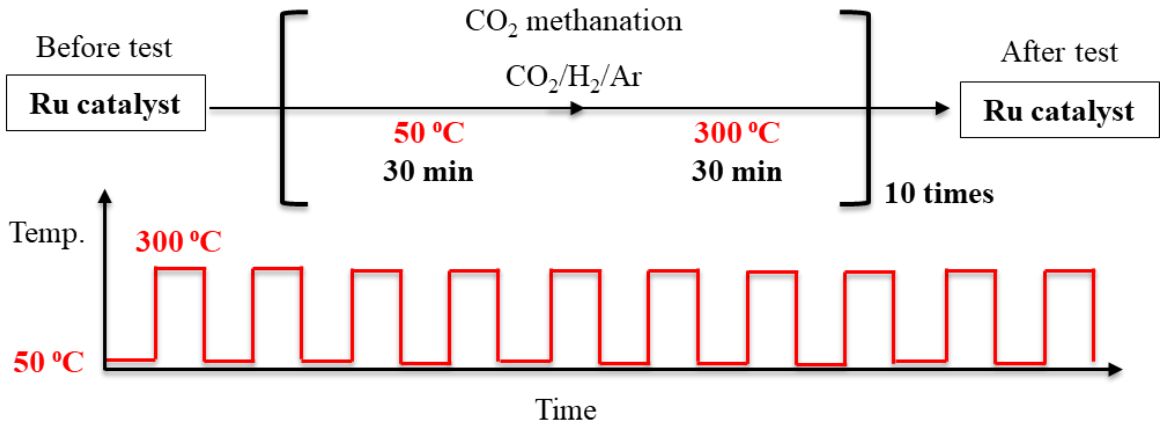

Figure 4.2. Schematic of the ten-cycle CO_2 methanation test.

Table 4.1. Properties of CeO_2 assemblies and CeO_2 nanocomposites supported Ru catalysts.

Sample[a]		Ru particle size (nm)		Ru dispersivity[c] (%)	Ru content[d] (wt%)	CeO_2 crystallite size[e] (nm)	Specific surface area[f] (m^2/g)
		From TEM[b]	From CO chemisorption[c]				
As-prepared	Ru/commercial CeO_2	7.7 ± 3.2	15.0	9.0	1.2	49	4.0
	Ru/CeO_2	—[g]	1.6	83.4	4.2	6.1	93
	Ru/SiO_2–CeO_2	0.6 ± 0.3	2.6	52.3	4.0	1.7	180
	Ru/TiO_2–CeO_2	1.0 ± 0.2	1.6	81.2	3.1	2.2	177
After a three-run test	Ru/commercial CeO_2	9.6 ± 4.8	—	—	1.9	48.7	3.9
	Ru/CeO_2	—[g]	—	—	4.2	10.3	39.6
	Ru/SiO_2–CeO_2	1.2 ± 0.4	—	—	4.5	1.7	61.1
	Ru/TiO_2–CeO_2	1.4 ± 03	—	—	3.2	2.1	68.3

[a]The Ru catalysts (3 wt%) deposited on commercial CeO_2, prepared CeO_2, SiO_2–CeO_2, and TiO_2–CeO_2 supports.

[b]Estimated by TEM images from at least 50 Ru particles.

[c]Calculated from CO adsorption measurements.

[d]Quantified by STEM/EDX analysis on TEM.

[e]The Scherrer equation was used.

[f]The BET method was used.

[g]Too small to be estimated by TEM.

4.3. Results and Discussion

4.3.1. Properties of Ru Catalysts Supported on CeO_2-Based Materials

Due to the fact that the large specific surface area and excellent heat tolerance of catalyst supports are quite suitable for good dispersion and stabilization of catalyst metals, our reported SiO_2–CeO_2 nanocomposites are potential supports to suppress the sintering of catalyst metals. I also selected the TiO_2–CeO_2 nanocomposite as a different type of support here, because some interactions between catalyst metals and TiO_2 supports can be expected.[38,39]

Dispersion of metal nanoparticles on supports is an essential factor that directly influences the catalytic activity in supported catalysts. The properties of the as-prepared catalysts were investigated using TEM, HAADF-STEM, EDX, CO chemisorption, XRD, and HAXPES measurements (Table 4.1, Figures 4.3–4.8). The TEM observations and CO chemisorption of the as-prepared catalysts reveal that the Ru particle size on commercial CeO_2 (Ru/commercial CeO_2) was quite large (7.7 nm by TEM) as compared to those of Ru on the prepared CeO_2 (Ru/CeO_2), the SiO_2–CeO_2 nanocomposite (Ru/SiO_2–CeO_2), and the TiO_2–CeO_2 nanocomposite (Ru/TiO_2–CeO_2) (Figure 4.3). In the case of Ru/CeO_2, the Ru nanoparticles were too small to be recognized in the TEM image. In the cases of Ru/SiO_2–CeO_2 and Ru/TiO_2–CeO_2, the average Ru nanoparticle sizes were measured to be so small, 0.6 and 1.0 nm, respectively.

The average crystallite sizes of CeO_2 in Ru/CeO_2 (6.1 nm, Scherrer equation), Ru/SiO_2–CeO_2 (1.7 nm), and Ru/TiO_2–CeO_2 (2.2 nm) are much smaller than that in Ru/commercial CeO_2 (49 nm), resulting in a much larger specific surface area of Ru/CeO_2 (93 m^2/g), Ru/SiO_2–CeO_2 (180 m^2/g), and Ru/TiO_2–CeO_2 (177 m^2/g) than that of Ru/commercial CeO_2 (4.0 m^2/g). In addition, the Ru dispersivity of Ru/CeO_2, Ru/SiO_2–CeO_2, and Ru/TiO_2–CeO_2 determined by CO pulse experiment is much better than that of Ru/commercial CeO_2. Homogeneous

distribution of Ru nanoparticles was also confirmed by STEM/EDX measurement of the supported Ru catalysts. The Ru contents were 1.2, 4.2, 4.0, and 3.1 wt% for Ru/commercial CeO_2, Ru/CeO_2, Ru/SiO_2–CeO_2, and Ru/TiO_2–CeO_2, respectively. Thus, the Ru nanoparticle and CeO_2 crystallite sizes of the prepared Ru/CeO_2, Ru/SiO_2–CeO_2, and Ru/TiO_2–CeO_2 are much smaller than those of Ru/commercial CeO_2.

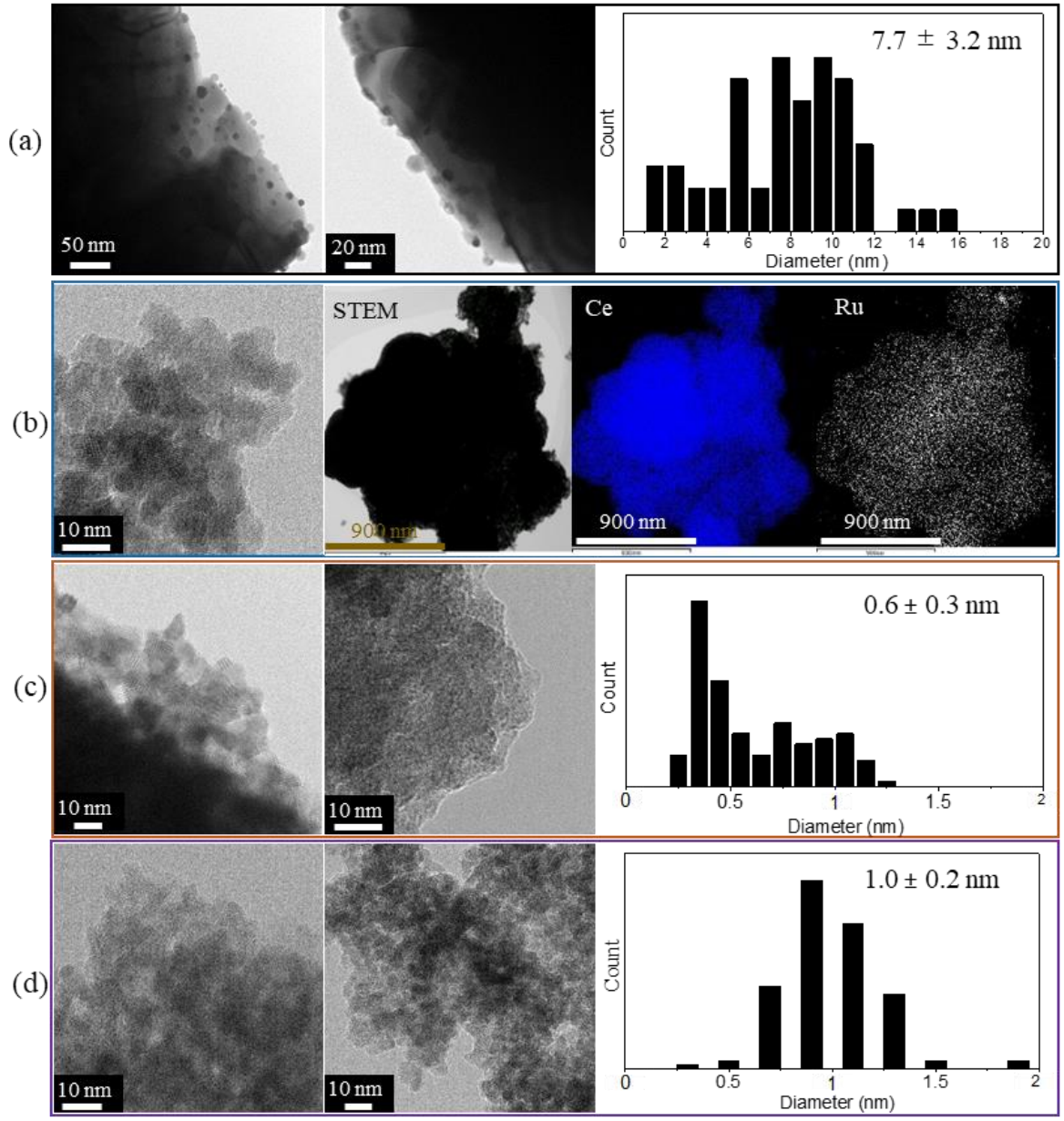

Figure 4.3. TEM and/or STEM/EDX images and Ru size distribution on the prepared catalysts: (a) Ru/commercial CeO_2, (b) Ru/CeO_2, (c) Ru/SiO_2–CeO_2, and (d) Ru/TiO_2–CeO_2.

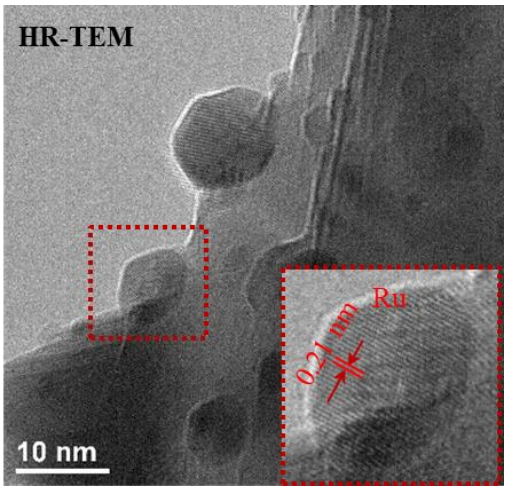

Figure 4.4. HR-TEM image of the as-prepared Ru/commercial CeO_2 catalyst.

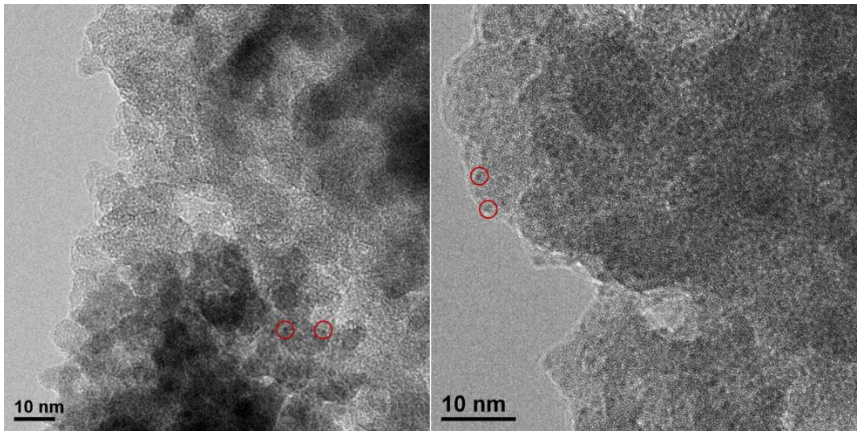

Figure 4.5. TEM images of the Ru/SiO_2–CeO_2 catalyst.

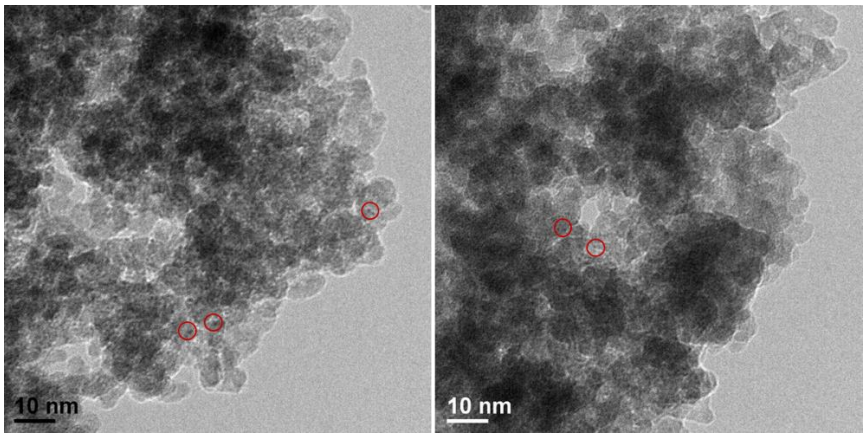

Figure 4.6. TEM images of the Ru/TiO_2–CeO_2 catalyst.

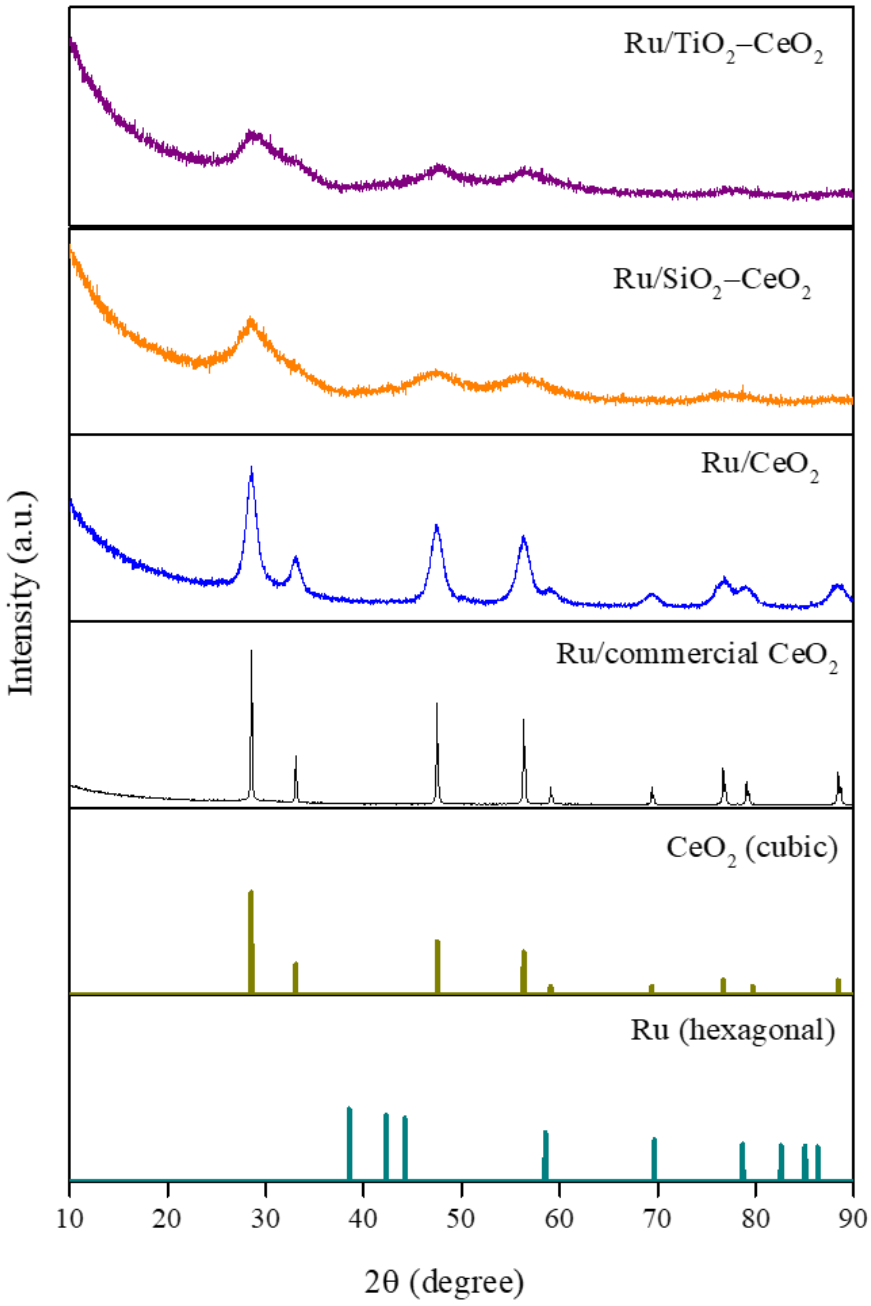

Figure 4.7. XRD patterns of the as-prepared catalysts. The reference peaks of JCPDS 00-004-0593 for CeO_2 cubic and JCPDS 01-073-7011 for Ru metal were shown in the khaki and cyan lines.

Next, the XRD patterns of the prepared catalysts Ru/CeO_2, $Ru/SiO_2–CeO_2$, and $Ru/TiO_2–CeO_2$ showed only reflection peaks ascribed to cubic CeO_2, whereas no peaks derived from Ru, SiO_2, and/or TiO_2 were detected (Figure 4.7), indicating that SiO_2 and TiO_2 in the

nanocomposites existed in amorphous phases. The existence of Ru on the CeO_2 and SiO_2–CeO_2 supports was also confirmed by HAXPES measurements (Figure 4.8).

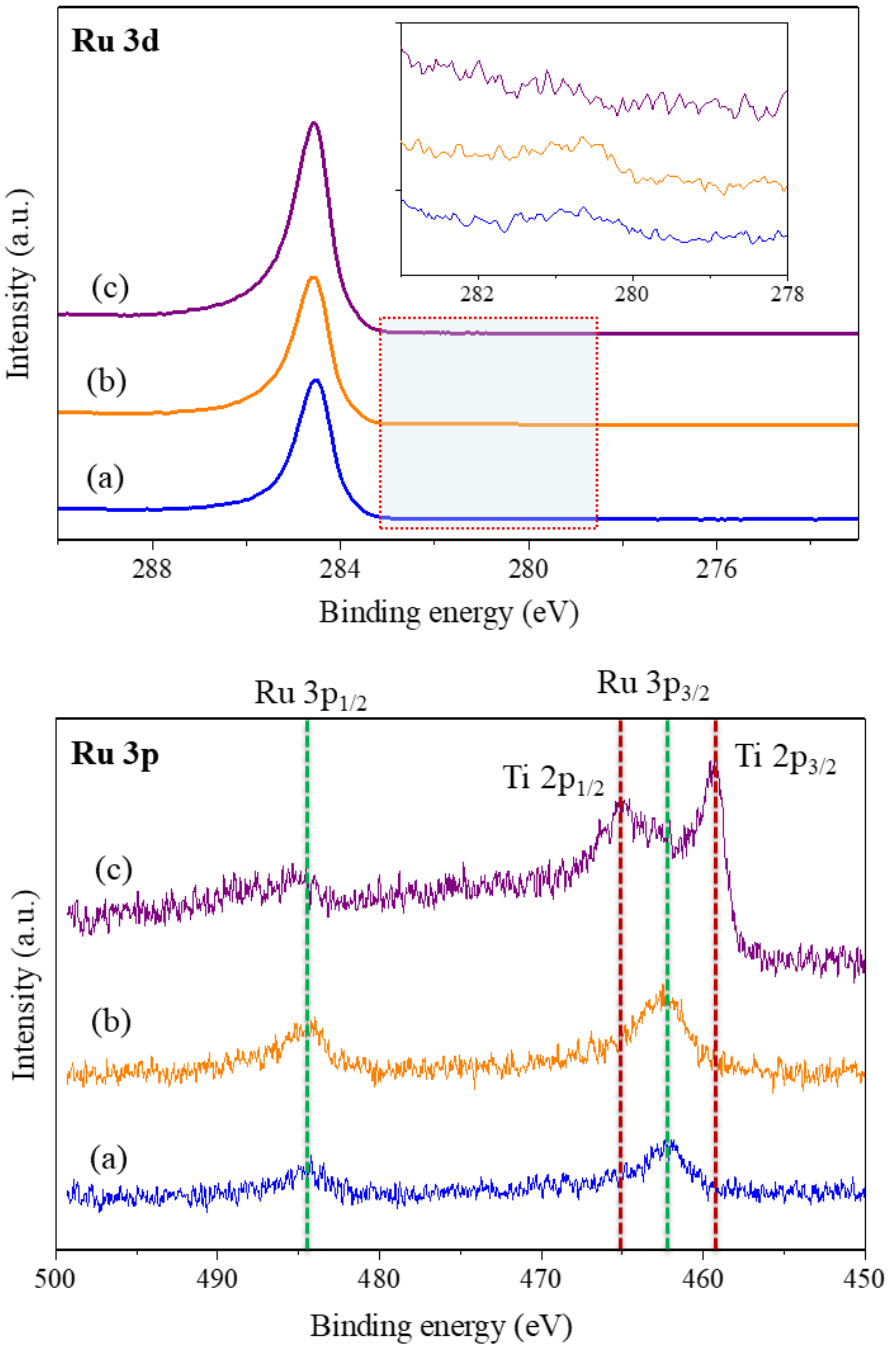

Figure 4.8. HAXPES Ru 3d and Ru 3p spectra of the as-prepared catalysts: (a) Ru/CeO_2, (b) Ru/SiO_2–CeO_2 and (c) Ru/TiO_2–CeO_2.

The H_2-TPR experiments were performed in order to clarify the surface properties of the catalyst supports and Ru nanoparticles on the supports (Figure 4.9). As a result, three types of responses were mainly observed for the prepared Ru/CeO_2, Ru/SiO_2–CeO_2, and Ru/TiO_2–CeO_2 (Figures 4.9b–4.9d), whereas two responses were found for Ru/commercial CeO_2 (Figure 4.9a). The peak that appeared at 100–200 °C can be attributed to the reduction of ruthenium oxides.[40,41] The peaks at 250–350 °C and around 800 °C can be ascribed to the reduction of the surface and the bulk of CeO_2, respectively.[27,42–44]. In addition, a peak was observed at 550–600 °C only in the case of Ru/TiO_2–CeO_2, which can be assigned to the reduction of TiO_2.[45] Therefore, the surface oxidation states of the prepared Ru/CeO_2, Ru/SiO_2–CeO_2, and Ru/TiO_2–CeO_2 are different from that of Ru/commercial CeO_2. Moreover, in the case of the prepared Ru/CeO_2, Ru/SiO_2–CeO_2, and Ru/TiO_2–CeO_2, the reduction of Ru species around 100–200 °C initiated at a lower temperature range, suggesting the existence of some interactions between Ru and the supports favorable to H_2 reduction.

Notably, H_2 uptakes of 2.90 mmol/g for Ru/SiO_2–CeO_2 and 1.99 mmol/g for Ru/TiO_2–CeO_2 at below 250°C were considerably higher than those of the Ru catalysts on the monocomponent CeO_2, which would indicate their greater reduction of Ru species (Table 4.2). Moreover, those values remarkably exceeded the theoretically required H_2 amount of 0.59 mmol/g to convert RuO_2 to metallic Ru, suggesting that a partial reduction of the composite supports are included.

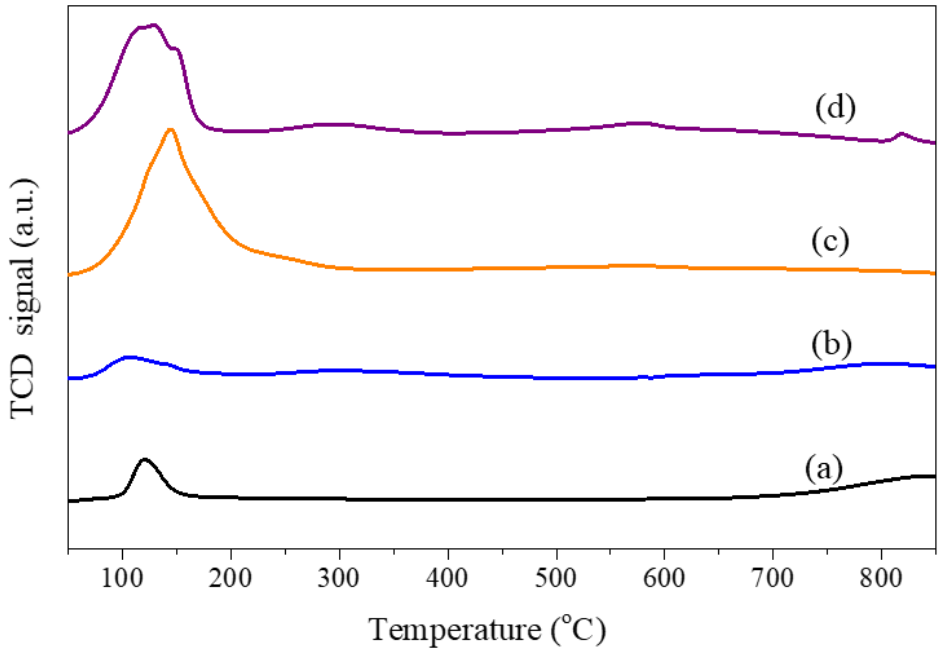

Figure 4.9. H_2-TPR profiles of the prepared catalysts: (a) Ru/commercial CeO_2, (b) Ru/CeO_2, (c) Ru/SiO_2–CeO_2, and (d) Ru/TiO_2–CeO_2.

Table 4.2. H_2 consumptions during the H_2-TPR experiments over the Ru catalysts.

Catalysts	H_2 uptake (mmol/g) at different temperature range		
	50 – 250 (°C)	250 – 350 (°C)	550 – 650 (°C)
Ru/commercial CeO_2	0.32[a]	-	-
Ru/CeO_2	0.35[a]	0.19	-
Ru/SiO_2–CeO_2	2.90[a]	-	-
Ru/TiO_2–CeO_2	1.99[a]	0.19	0.13

[a] Theoretical H_2 uptake for reduction of RuO_2 to metallic Ru^0 is 0.59 mmol/g catalyst.

4.3.2. Catalytic activity and durability of Ru catalysts supported on CeO_2-Based Materials

The prevention of sintering is an important requirement for catalysts to achieve a long lifetime. Here highly exothermic CO_2 methanation was selected as a probe reaction in order to check the sintering resistance of the catalysts. The catalytic activity and durability of the prepared catalysts were studied by a three-run experiment in a temperature range of 150–600 °C. The obtained CH_4 yields in the range of 100–400 °C are given in Figure 4.10. The detailed CO_2 consumption, CH_4 yield, and CO formation over the catalysts are shown in Figure 4.11.

When Ru/commercial CeO_2 was used as a catalyst, the maximum CH_4 yield was achieved at 350 °C to reach 55% (Figure 4.10a). However, when the prepared Ru/CeO_2, Ru/SiO_2–CeO_2, and Ru/TiO_2–CeO_2 catalysts were used, higher yields of ca. 80% were obtained (Figures 4.10b–4.10d).

The biggest advantage of my composite catalysts was seen in repeated reactions. When the reaction was repeated twice in the case of Ru/commercial CeO_2, the CH_4 yield profile drastically shifted to a higher temperature; namely, the catalytic activity clearly decreased (Figure 4.10a). On the contrary, almost no deactivation was observed in the prepared Ru/CeO_2 even after the third run of the reaction (Figure 4.10b). Interestingly, the low temperature activity at 150–200 °C was obviously improved in the cases of Ru/SiO_2–CeO_2 and Ru/TiO_2–CeO_2 nanocomposites when the reactions were repeated (Figures 4.10c and 4.10d). It is difficult to put forward a conclusive discussion. However, this could be ascribed to the enhanced interactions between the support nanoparticles and the Ru metal particles under high temperature conditions. A similar positive effect of heating on the catalytic activity of supports was reported for calcined Ru/CeO_2 and Ru/TiO_2 catalysts with strengthened interactions

between Ru and ceria supports as well as between Ru and titania supports.[32,46,47]

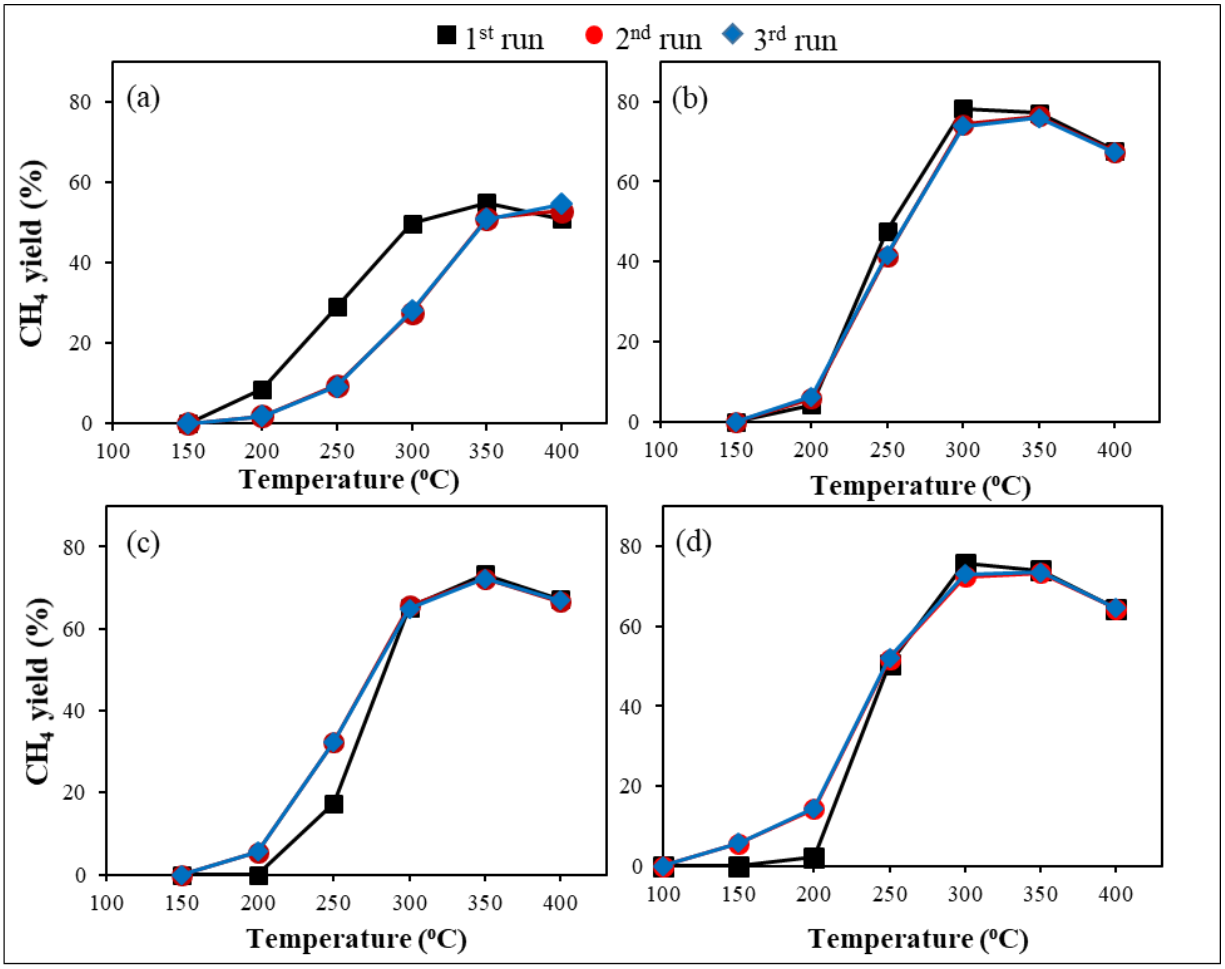

Figure 4.10. CH_4 production of a three-run test over the catalysts: (a) Ru/commercial CeO_2, (b) Ru/CeO_2, (c) Ru/SiO_2–CeO_2, and (d) Ru/TiO_2–CeO_2. The reaction process for each run was carried out in a temperature range of 150–600 °C at a gas flow rate of 20 mL/min (5% CO_2, 20% H_2, and 75% Ar). The described process of each run was then sequentially repeated three times. For ease of recognition of the efficiency difference in catalysis, a small amount of catalyst (100 mg) was used for this experiment. When a larger amount of catalyst (1 g) was used, 100% conversion of CO_2 and 100% yield of CH_4 were easily achieved at 250 °C.

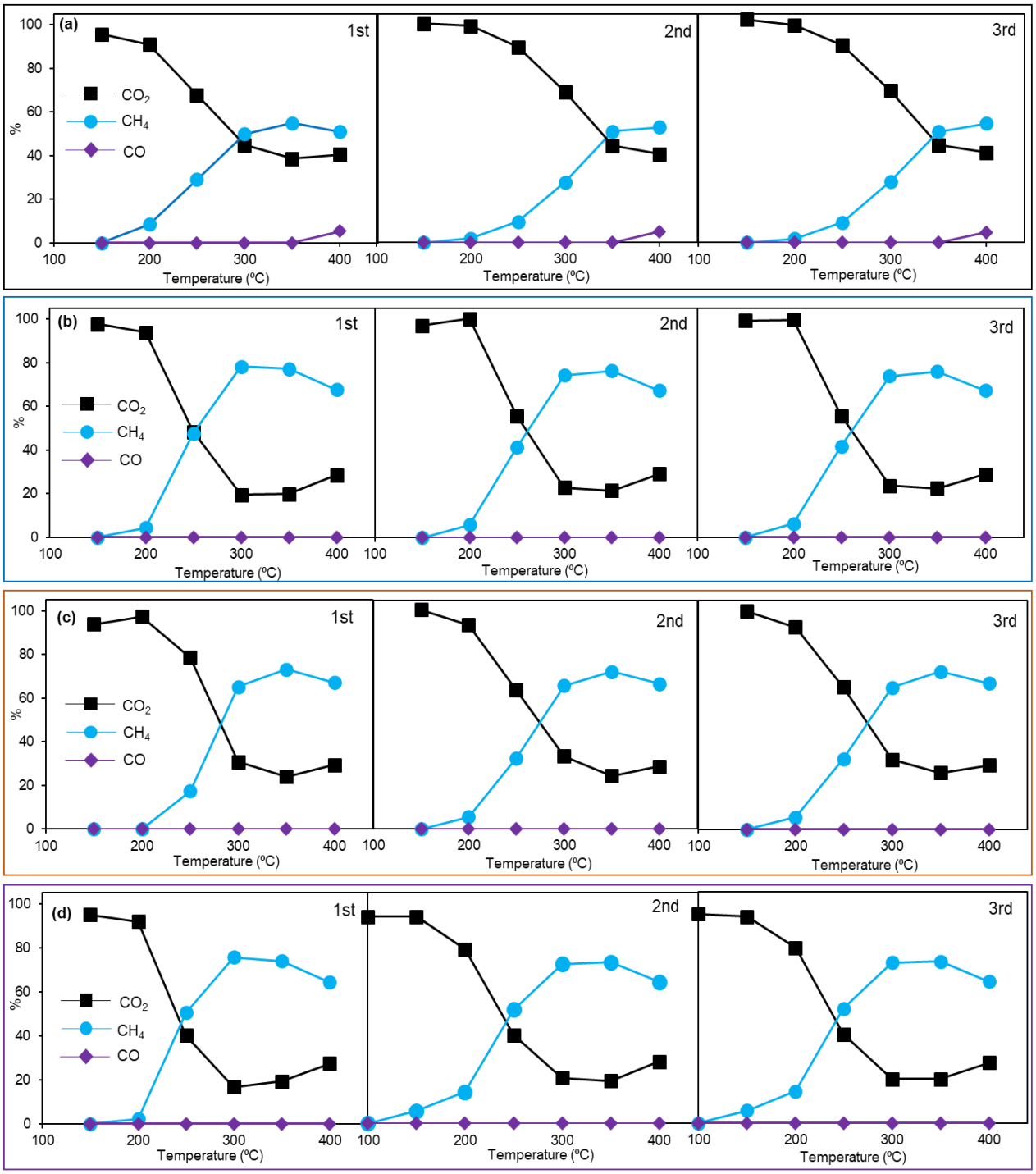

Figure 4.11. CO_2 consumption, CH_4 yield, and CO formation (%) in the 3-run test of (a) Ru/commercial CeO_2, (b) Ru/CeO_2, (c) Ru/SiO_2–CeO_2, and (d)Ru/TiO_2–CeO_2.

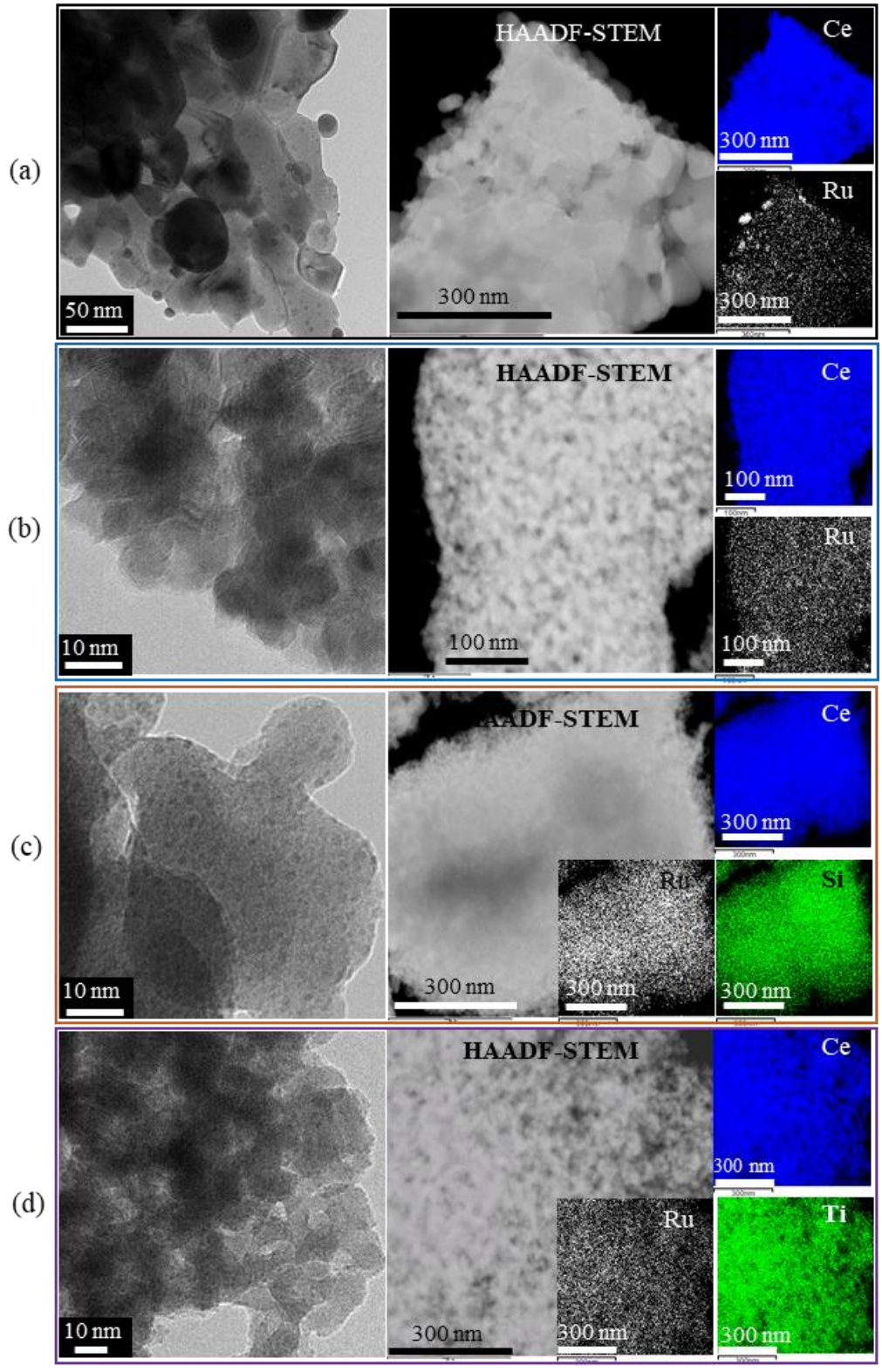

Figure 4.12. TEM images, HAADF-STEM images, and EDX mappings of Ce, Si, and Ru elements of the catalysts: (a) Ru/commercial CeO_2, (b) Ru/CeO_2, (c) Ru/SiO_2–CeO_2, and (d) Ru/TiO_2–CeO_2 after the three-run test.

In order to clarify the sintered structure of both metal particles and supports, the morphological changes of the catalysts after the three-run test were directly investigated by TEM and HAADF-STEM observations (Figure 4.12), and the estimated Ru mean diameters are listed in Table 4.1.

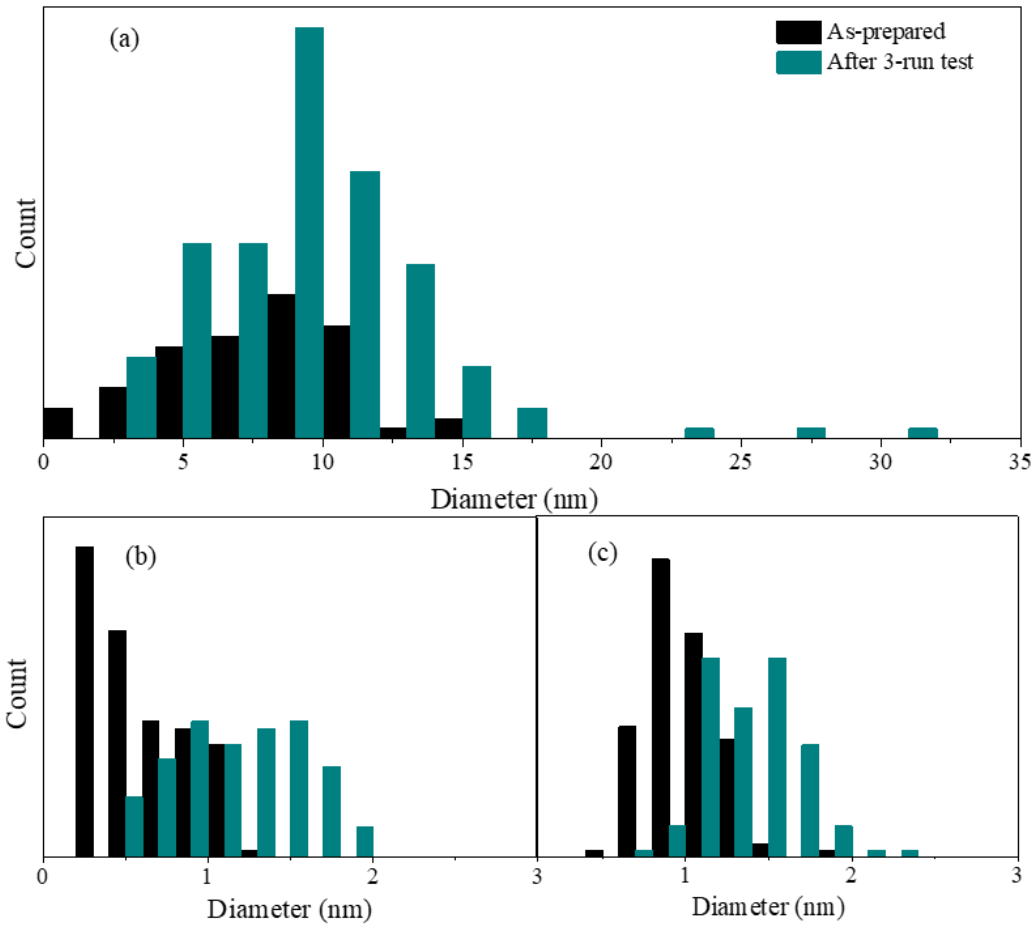

Figure 4.13. Ru particle size distributions in the as-prepared state and after the three-run test of the catalysts: (a) Ru/commercial CeO_2, (b) Ru/SiO_2–CeO_2, and (c) Ru/TiO_2–CeO_2.

Figure 4.12a shows the existence of large-sized Ru nanoparticles deposited on the commercial CeO_2 support, whose particle size changed from 7.7 to 9.6 nm (Table 4.1). However, the existence of a small amount of much larger Ru nanoparticles (20–30 nm) was confirmed (Figure 4.13a), indicating that the conditions of the three-run test were so severe

for the Ru/commercial CeO_2 catalyst to cause sintering. In contrast, uniform Ru dispersions on CeO_2, SiO_2–CeO_2, and TiO_2–CeO_2 were retained after the three-run test, as demonstrated by HAADF-STEM images and EDX mappings, where no Ru agglomerations were observed (Figures 4.12b–4.12d). The growth of only small Ru nanoparticles was observed in the cases of Ru/SiO_2–CeO_2 and Ru/TiO_2–CeO_2, and the particle size still remained 1–2 nm (Table 4.1, Figures 4.13b and 4.13c). Moreover, no enlargement of the CeO_2 crystallites was observed even after the three-run test (Table 4.1), revealing the effective sintering suppression of Ru nanoparticles as well as CeO_2 crystallites on/in both SiO_2–CeO_2 and TiO_2–CeO_2 supports. These discussed results indicate that remained good dispersion of Ru nanoparticles on the prepared CeO_2-based supports during CO_2 methanation could be a reason for maintained activity of the catalysts.

As a result, the Ru/TiO_2–CeO_2 nanocomposite exhibited the best performance of not only the low temperature activity and the maximum yield, but also the sintering resistance of Ru nanoparticles and CeO_2 crystallite in CO_2 methanation. As presented in Figure 4.14, the Ce3d HAXPES spectra of the supports showed Ce^{3+}/Ce^{4+} coexistence in the prepared CeO_2 composite supports, whereas only the Ce^{4+} oxidation state was formed in the case of the commercial CeO_2. The peak positions of Ce^{4+} and Ce^{3+} marked by yellow and green in Figure 6, respectively, were obtained from the literatures.[38,48] Moreover, it is noted that the TiO_2–CeO_2 composite exhibited a favored Ce^{3+} formation that could be responsible for its higher catalytic activity as compared to the prepared monocomponent CeO_2. These results agree well with the previous literature where the Ce–Ti interface was reported to strongly promote the Ce^{3+} existence because of the electron contact.[38] It is reported that Ce^{3+} sites created on the CeO_2 surface are involved in activation of CO_2, contributing to a better activity of catalysts.[19,27,49,50] Indeed, Ce^{3+} sites act as active sites for adsorption and dissociation of CO_2 to form carbonaceous intermediates which are rapidly hydrogenated into CH_4 molecules.

Therefore, the abundant Ce^{3+} formation on the surface of the CeO_2-based catalysts is advantage in promoting CO_2 methanation. Thus, the prepared CeO_2, SiO_2–CeO_2, and TiO_2–CeO_2 nanocomposites turned out to be promising sintering-resistant catalyst supports for the elevated temperature process of CO_2 methanation.

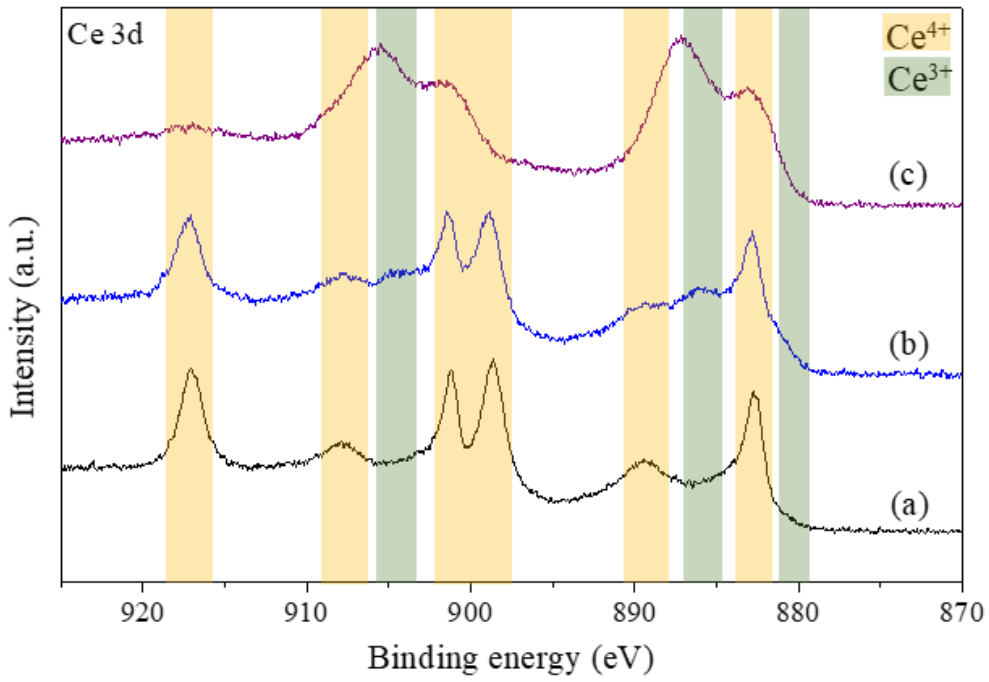

Figure 4.14. HAXPES Ce3d spectra of (a) commercial CeO_2, (b) prepared CeO_2, and (c) prepared TiO_2–CeO_2. The peak positions of Ce^{4+} and Ce^{3+} marked by yellow and green in Figure 6, respectively, were obtained from the literatures.[38,48]

Calcined Catalysts

According to the above-mentioned activity enhancement of Ru catalysts supported on CeO_2-based materials after the three-run test, CeO_2, SiO_2–CeO_2, and TiO_2–CeO_2 were calcined at 500 °C for 2 h prior to Ru deposition in the expectation of catalytic activity enhancement, yielding Ru/calcined CeO_2, Ru/calcined SiO_2–CeO_2, and Ru/calcined TiO_2–

CeO_2, respectively. The crystallite sizes of CeO_2 in Ru/CeO_2, Ru/calcined SiO_2–CeO_2, and Ru/calcined TiO_2–CeO_2 (Table 4.3) are quite comparable to those after the three-run test (Table 4.1). The specific surface areas of the calcined catalysts are a little bit larger than those after the three-run test. When the calcined catalysts were used for CO_2 methanation, Ru/calcined CeO_2 and Ru/calcined TiO_2–CeO_2 exhibited higher activities than that of Ru/calcined SiO_2–CeO_2 (Figure 4.15). The low-temperature catalytic activity of Ru/calcined CeO_2 (150–250 °C) towards CO_2 methanation in the present study is comparable with those in the literatures.[19,27] Notably, an obvious enhancement of low temperature activity at 150–200 °C was observed in the case of Ru/calcined TiO_2–CeO_2.

Table 4.3. Ru content, Ru dispersion, CeO_2 crystallite size, and specific surface area of the fresh Ru catalysts prepared on the different calcined nanocomposites.

Sample[a]	CeO_2 crystallite size[b] (nm)	Specific surface area[c] (m^2/g)
Ru/calcined CeO_2	8.9	63.5
Ru/calcined SiO_2–CeO_2	2.6	120
Ru/calcined TiO_2–CeO_2	2.3	119

[a]The Ru catalysts (3 wt%) deposited on the supports calcined at 500 °C for 2 h.

[b]Estimated by Scherrer equation.

[c]The BET method was used.

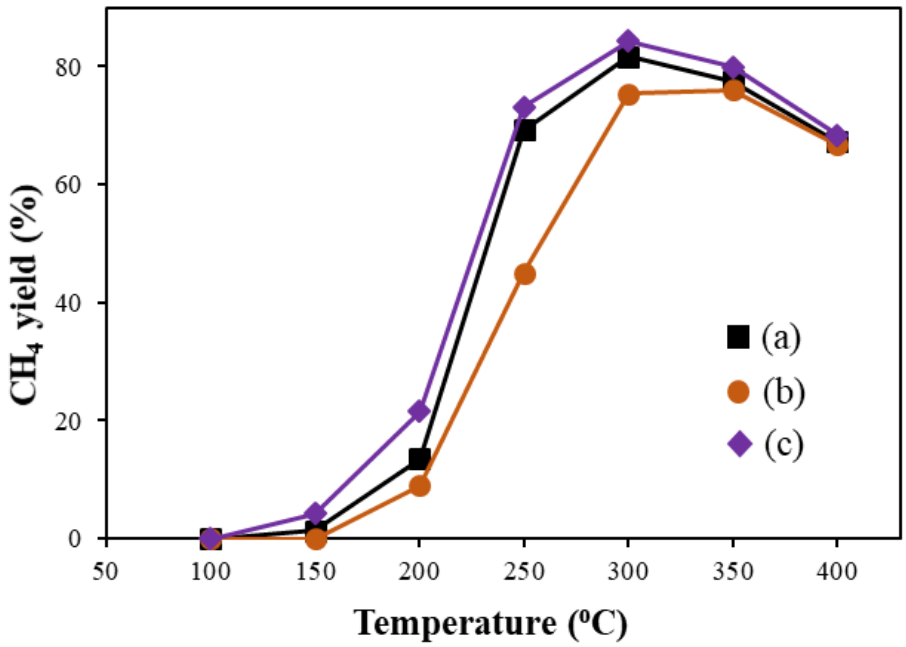

Figure 4.15. CH_4 production of CO_2 methanation over (a) Ru/calcined CeO_2, (b) Ru/calcined SiO_2–CeO_2, and (c) Ru/calcined TiO_2–CeO_2. The CO_2 methanation test was carried out in the temperature range of 150–600 °C at a gas flow rate of 20 mL/min (5% CO_2, 20% H_2, and 75% Ar). The reaction time for each temperature step was kept at 30 min.

4.3.3. Long-Term Stability Test of the Ru Catalysts

As mentioned in the former section, the prepared CeO_2, SiO_2–CeO_2, and TiO_2–CeO_2 supports led to a high activity and high sintering resistance for Ru catalysts as compared to the commercial CeO_2 support. In order to further support the aforementioned discussions, the stability and durability of the catalysts were investigated through two different experiments: a 10-cycle test and a long-term experiment. In the 10-cycle test, severe heat stress was placed on the catalysts, where CO_2 methanation was repeated 10 times at a low temperature (50 °C) and a high temperature (300 °C) alternatively. In each cycle, the reaction time was 30 min at each reaction temperature. Figure 4.16a clearly shows stable CH_4 production over Ru/CeO_2

during the 10-cycle experiment. Likewise, a stable catalytic performance with almost no change in the CH_4 yield between the 1st and the 10th cycles was observed when the Ru/TiO_2–CeO_2 nanocomposite was used (Figure 4.16c). However, under similar conditions, the catalytic performance over Ru/commercial CeO_2 decreased gradually by each cycle, clearly indicating catalytic activity loss by thermal sintering (Figure 4.17).

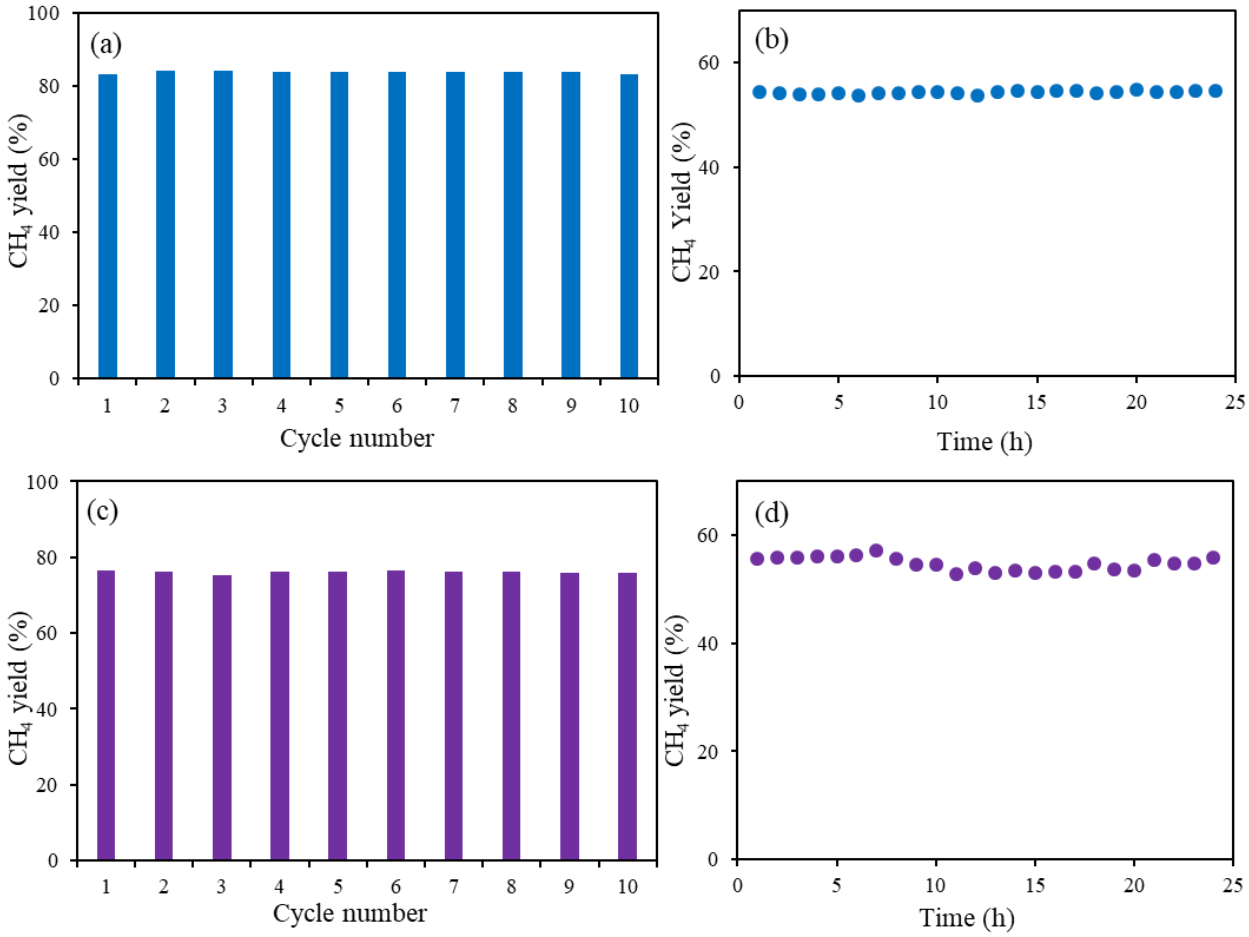

Figure 4.16. CH_4 yield of CO_2 methanation using (a, b) Ru/CeO_2 and (c, d) Ru/TiO_2–CeO_2 in the 10-cycle test at 50 °C and 300 °C (the graph represents only the results at 300 °C) and for 24 h at 400 °C, respectively. In each cycle of the 10-cycle test, the reaction time was 30 min at each reaction temperature of 50 °C and 300 °C. In the cases of (a) and (c), 100 mg of catalysts were used, while 25 mg of catalysts were used in the cases of (b) and (d) in expectation of earlier activity loss of the catalysts in the long-term stability tests.

In addition, the long-term stability of Ru/CeO_2 was confirmed by a constant CH_4 yield as the time-on-stream increased to 24 h (Figures 4.16b and 4.16d) at 400 °C. In contrast, the long-term stability test for 24 h at 400 °C with the use of Ru/commercial CeO_2 catalyst resulted in 2% initial yield of CH_4, but the yield reduced gradually to 0% within 10 h (Figure 4.18). Thus, the three prepared CeO_2, SiO_2–CeO_2, and TiO_2–CeO_2 nanocomposites were effective supports in enhancing the catalyst activity and durability of Ru catalysts for CO_2 methanation. Their further applications in other high temperature systems are highly expected.

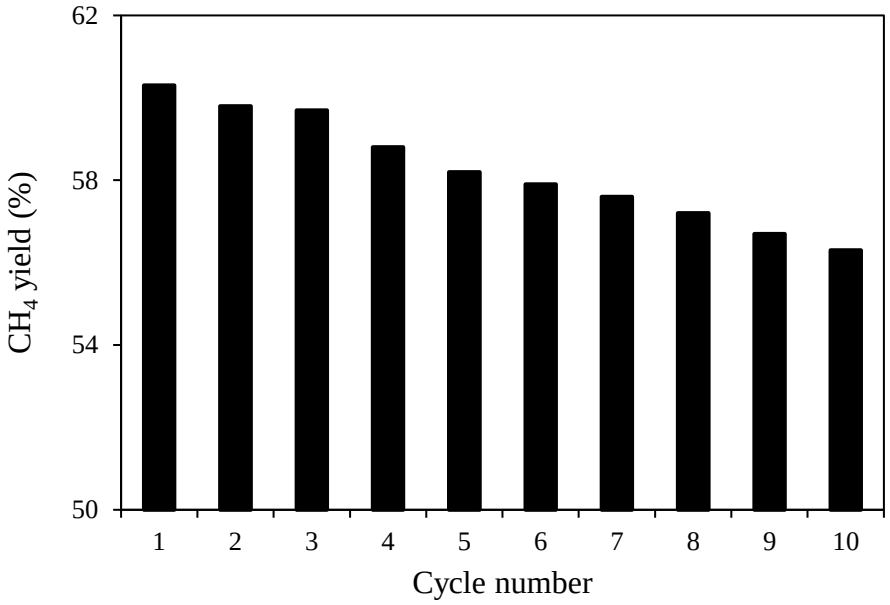

Figure 4.17. CH_4 yield for CO_2 methanation over Ru/commercial CeO_2 in 10-cycle test at 50 °C and 300 °C (graph represents only the results at 300 °C). The reaction time at each temperature was kept at 30 min and the total gas flow was 20 mL/min (5% CO_2, 20% H_2, and 75% Ar).

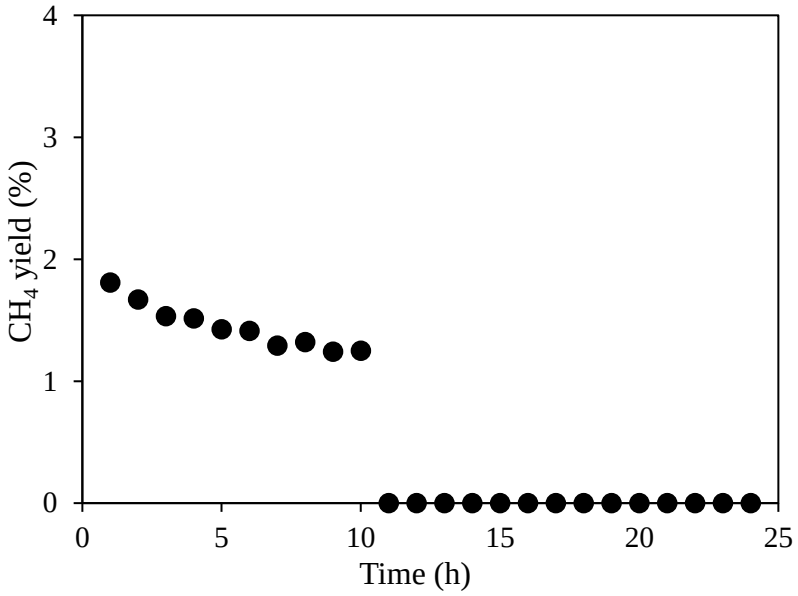

Figure 4.18. CH_4 yield for CO_2 methanation over Ru/commercial CeO_2 in long-term stability test at 400 °C. The reaction time was kept at 30 min and the total gas flow was 20 mL/min (5% CO_2, 20% H_2, and 75% Ar). An amount of 25 mg of catalysts was used in expectation of earlier activity loss of the catalysts in the long-term stability tests.

4.4. Conclusions

A porous CeO_2 aggregate, SiO_2–CeO_2 nanocomposite, and TiO_2–CeO_2 nanocomposite, all of which consisted of a number of small primary particles (<5 nm) with a huge surface area, were solvothermally prepared as catalyst supports for highly exothermic reactions. Ru nanoparticles were deposited on the support surface by the precipitation–deposition method. The prepared catalyst supports of CeO_2 aggregate, SiO_2–CeO_2 nanocomposite, and TiO_2–CeO_2 nanocomposite dispersed Ru nanoparticles very well on the surface. When they were used as catalysts for CO_2 methanation by H_2, the Ru catalysts on the prepared CeO_2 aggregate and TiO_2–CeO_2 exhibited a better low temperature (150–200 °C) activity and long-term stability (400 °C, 24 h) than those on the commercial CeO_2 aggregate. Thus, we succeeded in

preparing sintering-resistant catalyst supports for high temperature reactions.

References

[1] E. Goodman, J. Schwalbe, M. Cargnello, Mechanistic understanding and the rational design of sinter-resistant heterogeneous catalysts, *ACS Catal.* **2017**, *7*, 7156−7173.

[2] T. Hansen, A. Delariva, S. Challa, A. Datye, Sintering of catalytic nanoparticles: particle migration or Ostwald ripening?, *Acc. Chem. Res.* **2013**, *46*, 1720−1730.

[3] G. Busca in *Heterogeneous Catalytic Materials Solid State Chemistry*, *Surface Chemistry and Catalytic Behaviour*, Chapter 4, Elsevier, Oxford, **2014**, pp. 37−55.

[4] E. Bayram, J. Lu, C. Aydin, N. D. Browning, S. Ozkar, E. Finney, B. C. Gates, R. G. Finke, Agglomerative sintering of an atomically dispersed Ir1/Zeolite Y catalyst: compelling evidence against Ostwald ripening but for bimolecular and autocatalytic agglomeration catalyst sintering steps, *ACS Catal.* **2015**, *5*, 3514−3527.

[5] Q. Xu, K. C. Kharas, B. J. Croley, A. K. Datye, The sintering of supported Pd automotive catalysts, *ChemCatChem* **2011**, *3*, 1004−1014.

[6] C. H. Bartholomew, Mechanisms of catalyst deactivation, *Appl. Catal., A* **2001**, *212*, 17−60.

[7] Ali M. Abdel-Mageed, D. Widmann, S. E. Olesen, I. Chorkendorf, R. J. Behm, Selective CO methanation on highly active Ru/TiO_2 catalysts: identifying the physical origin of the observed activation/deactivation and loss in selectivity, *ACS Catal.* **2018**, *8*, 5399−5414.

[8] J. Im, M. Choi, Physicochemical stabilization of Pt against sintering for a dehydrogenation catalyst with high activity, selectivity, and durability, *ACS Catal.* **2016**, 6, 2819−2826.

[9] B. Mutz, M. Belimov, W. Wang, P. Sprenger, M. Serrer, D. Wang, P. Pfeifer, W. Kleist, J. Grunwaldt, Potential of an alumina-supported Ni_3Fe catalyst in the methanation of CO_2:

impact of alloy formation on activity and stability, *ACS Catal.* **2017**, 7, 6802−6814.

[10] L. Adijanto, D. A. Bennett, C. Chen, A. S. Yu, M. Cargnello, P. Fornasiero, R. J. Gorte, J. M. Vohs, Exceptional thermal stability of Pd@CeO_2 core−shell catalyst nanostructures grafted onto an oxide surface*, Nano Lett.* **2013**, *13*, 2252−2257.

[11] P. M. Arnal, M. Comotti, F. Schuth, High-temperature stable catalysts by hollow sphere encapsulation, *Angew. Chem. Int. Ed.* **2006**, 45, 8224−8227.

[12] S. Lee, J. Seo, W. Jung, Sintering-resistant Pt@CeO_2 nanoparticles for high-temperature oxidation catalysis, *Nanoscale* **2016**, 8, 10219−10228.

[13] G. Prieto, J. Zecevic, H. Friedrich, K. P. d. Jong, P. E. Jongh, Towards stable catalysts by controlling collective properties of supported metal nanoparticles, *Nat. Mater.* **2013**, 12, 34−39.

[14] K. Yoon, Y. Yang, P. Lu, D. Wan, H.C. Peng, K. S. Masias, P. T. Fanson, C. T. Campbell, Y. Xia, A highly reactive and sinter-resistant catalytic system based on platinum nanoparticles embedded in the inner surfaces of CeO_2 hollow fibers, *Angew. Chem. Int. Ed.* **2012**, *51*, 9543−9546.

[15] P. Wang, K. Ueno, H. Takigawa, K. Kobiro, Versatility of one-pot, single-step synthetic approach for spherical porous (metal) oxide nanoparticles using supercritical alcohols, *J. Supercrit. Fluid* **2013**, *78*, 124–131.

[16] P. Wang, K. Kobiro, Synthetic versatility of nanoparticles: A new, rapid, one-pot, single-step synthetic approach to spherical mesoporous (metal) oxide nanoparticles using supercritical alcohols, *Pure Appl. Chem.* **2014**, *86*, 785–800.

[17] E. K. C. Pradeep, T. Habu, H. Tooriyama, M. Ohtani, K. Kobiro, Ultra-simple synthetic approach to the fabrication of CeO_2–ZrO_2 mixed nanoparticles into homogeneous, domain, and core–shell structures in mesoporous spherical morphologies using supercritical alcohols, *J. Supercrit. Fluid* **2015**, *97*, 217–223.

[18] F. Duriyasart, A. Irizawa, K. Hayashi, Masataka Ohtani, K. Kobiro, Sintering-resistant metal catalysts supported on concave-convex surface of TiO_2 nanoparticle assemblies, *ChemCatChem* **2018**, *10*, 3392−3396.

[19] F. Wang, S. He, H. Chen, B. Wang, L. Zheng, D. G. Evans, X. Duan, Active site dependent reaction mechanism over Ru/CeO_2 catalyst toward CO_2 methanation, *J. Am. Chem. Soc.* **2016**, *138*, 6298−6305.

[20] F. Wang, C. Li, X. Zhang, M. Wei, D. G. Evans, X. Duan, Catalytic behavior of supported Ru nanoparticles on the {100}, {110}, and {111} facet of CeO_2, *J. Catal.* **2015**, *329*, 177−186.

[21] S. Dutta, M. Seehra, Y. Shi, E. Eyring, R. Ernst, Concentration of Ce^{3+} and oxygen vacancies in cerium oxide nanoparticles, *Chem. Mater.* **2006**, *18*, 5144−5146.

[22] E. Aneggi, D. Wiater, C. Leitenburg, J. Llorca, A. Trovarelli, Shape-dependent activity of ceria in soot combustion, *ACS Catal.* **2014**, *4*, 172−181.

[23] J. Li, G. Lu, G. Wu, D. Mao, Y. Wang, Y. Guo, Promotional role of ceria on cobaltosic oxide catalyst for low-temperature CO oxidation, *Catal. Sci. Technol.* **2012**, *2*, 1865−1871.

[24] J. Li, Z. Zhang, W. Gao, S. Zhang, Y. Ma, Y. Qu, Pressure regulations on the surface properties of CeO_2 nanorods and their catalytic activity for CO oxidation and nitrile hydrolysis reactions, *ACS Appl. Mater. Interfaces* **2016**, *8*, 22988−22996.

[25] Y. Li, Q. Sun, M. Kong, W. Shi, J. Huang, J. Tang, X. Zhao, Coupling oxygen ion conduction to photocatalysis in mesoporous nanorod-like ceria significantly improves photocatalytic efficiency, *J. Phys. Chem. C* **2011**, *115*, 14050–14057.

[26] T. Montini, M. Melchionna, M. Monai, P. Fornasiero, Fundamentals and catalytic applications of CeO_2-based materials, *Chem. Rev.* **2016**, *116*, 5987−6041.

[27] Y. Guo, S. Mei, K. Yuan, D. Wang, H. Liu, C. H. Yan, Y. Zhang, Low-temperature CO_2

methanation over CeO_2-supported Ru single atoms, nanoclusters, and nanoparticles competitively tuned by strong metal−support interactions and H-spillover effect, *ACS Catal.* **2018**, *8*, 6203−6215.

[28] P. Concepcion, A. Corma, J. Silvestre Albero, V. Franco, J. Y. Chane-Ching, Chemoselective hydrogenation catalysts: Pt on mesostructured CeO_2 nanoparticles embedded within ultrathin layers of SiO_2 binder, *J. Am. Chem. Soc.* **2004**, *126*, 5523−5532.

[29] S. Gatla, D. Aubert, G. Agostini, O. Mathon, S. Pascarelli, T. Lunkenbein, M. Willinger, H. Kaper, Room-temperature CO oxidation catalyst: low-temperature metal−support interaction between platinum nanoparticles and nanosized ceria, *ACS Catal.* **2016**, *6,* 6151−6155.

[30] P. Lustemberg, P. J. Ramírez, Z. Liu, R. A. Gutiérrez, D. G. Grinter, J. Carrasco, S. D. Senanayake, J. A. Rodriguez, M. V. Ganduglia Pirovano, Room-temperature activation of methane and dry re-forming with CO_2 on Ni-CeO_2 (111) surfaces: effect of Ce^{3+} sites and metal−support interactions on C−H bond cleavage, *ACS Catal.* **2016**, *6*, 8184−8191.

[31] M. Tamura, T. Kitanaka, Y. Nakagawa, K. Tomishige, Cu sub-nanoparticles on Cu/CeO_2 as an effective catalyst for methanol synthesis from organic carbonate by hydrogenation, *ACS Catal.* **2016**, *6,* 376−380.

[32] S. Hosokawa, M. Taniguchi, K. Utani, H. Kanai, S. Imamura, Affinity order among noble metals and CeO_2, *Appl. Catal., A* **2005**, *289*, 115−120.

[33] K. R. Priolkar, P. Bera, P. R. Sarode, M. S. Hegde, S. Emura, R. Kumashiro, N. P. Lalla, Formation of $Ce_{1-x}Pd_xO_{2-\delta}$ solid solution in combustion-synthesized Pd/CeO_2 catalyst: XRD, XPS, and EXAFS investigation, *Chem. Mater.* **2002**, *14,* 2120−2128.

[34] H. T. T. Nguyen, M. Ohtani, K. Kobiro, One-pot synthesis of SiO_2–CeO_2 nanoparticle composites with enhanced heat tolerance, *Microporous Mesoporous Mat.* **2019**, *273,*

35−40.

[35] J. Gao, Q. Liu, F. Gu, B. Liu, Z. Zhong, F. Su, Recent advances in methanation catalysts for the production of synthetic natural gas, *RSC Adv.* **2015**, *5*, 22759−22776.

[36] S. Rönsch, J. Schneider, S. Matthischke, M. Schlüter, M. Götz, J. Lefebvre, P. Prabhakaran, S. Bajohr, Review on methanation–From fundamentals to current projects, *Fuel* **2016**, *166*, 276−296.

[37] J. Gao, J. Wang, Y. Ping, D. Hu, G. Xu, F. Gu, F. Su, A thermodynamic analysis of methanation reactions of carbon oxides for the production of synthetic natural gas, *RSC Adv.* **2012**, 2, 2358−2368.

[38] M. J. Muñoz-Batista, M. N. Gomez-Cerezo, A. Kubacka, D. Tudela, M. Fernandez-García, Role of interface contact in CeO_2−TiO_2 photocatalytic composite materials, *ACS Catal.* **2014**, *4,* 63−72.

[39] A. Abdel-Mageed, D. Widmann, S. Olesen, I. Chorkendorff, J. Biskupek, R. Behm, Selective CO methanation on Ru/TiO_2 catalysts: role and influence of metal−support interactions, *ACS Catal.* **2015**, *5*, 6753−6763.

[40] X. Liao, K. Li, X. Xiang, S. G. Wang, X. She, Y. Zhu, Y. Li, Mediatory role of K, Cu and Mo over Ru/SiO_2 catalysts for glycerol hydrogenolysis, *J. Ind. Eng. Chem.* **2012**, *18*, 818−821.

[41] N. Hamzah, N. M. Nordinc, A. H. A. Nadzri, Y. A. Nik, M. B. Kassim, M. A. Yarmo, Enhanced activity of Ru/TiO_2 catalyst using bisupport, bentonite-TiO_2 for hydrogenolysis of glycerol in aqueous media, *Appl. Catal. A-Gen.* **2012**, *419−420*, 133−141.

[42] J. Okal, M. Zawadzki, P. Kraszkiewicz, K. Adamska, Ru/CeO_2 catalysts for combustion of mixture of light hydrocarbons: effect of preparation method and metal salt precursors, *Appl. Catal. A-Gen.* **2018**, *549*, 161−169.

[43] Z. Hu, X. Liu, D. Meng, Y. Guo, Y. Guo, G. Lu, Effect of ceria crystal plane on the

physicochemical and catalytic properties of Pd/ceria for CO and propane oxidation, *ACS Catal.* **2016**, *6*, 2265−2279.

[44] Z. Ma, S. Zhao, X. Pei, X. Xiong, B. Hu, New insights into the support morphology-dependent ammonia synthesis activity of Ru/CeO_2 catalysts, *Catal. Sci. Technol.* **2017**, *7*, 191−199.

[45] H. Zhu, Z. Qin, W. Shan, W. Shen, J. Wang, Pd/CeO_2–TiO_2 catalyst for CO oxidation at low temperature: a TPR study with H_2 and CO as reducing agents, *J. Catal.* **2004**, *7*, 267−277.

[46] S. Hosokawa, H. Kanai, K. Utani, Y. Taniguchi, Y. Saito, S. Imamura, State of Ru on CeO_2 and its catalytic activity in wet oxidation of acetic acid, *Appl. Catal. B-Environ.* **2003**, *45*, 181−187.

[47] A. Kim, D. Debecker, F. Devred, V. Dubois, C. Sanchez, C. Sassoye, CO_2 methanation on Ru/TiO_2 catalysts: on the effect of mixing anatase and rutile TiO_2 supports, *Appl. Catal. B-Environ* **2018**, *220*, 615−625.

[48] C. Barth, C. Laffon, R. Olbrich, A. Ranguis, P. Parent, M. Reichling, A perfectly toichiometric and flat CeO_2 (111) surface on a bulk-like ceria film, *Sci. Rep.* **2016**, *6*, 21165.

[49] C. Leitenburg, A. Trovarelli, J. Kaspar, A temperature-programmed and transient kinetic study of CO_2 activation and methanation over CeO_2 supported noble metals, *J. Catal.* **1997**, *166*, 98−107.

[50] P. A. Ussa Aldana, F. Ocampo, K. Kobl, B. Louis, F. Thibault-Starzyk, M. Daturi, P. Bazin, S. Thomas, A.C. Roger, Catalytic CO_2 valorization into CH_4 on Ni-based ceria-zirconia. Reaction mechanism by operando IR spectroscopy, *Catal. Today* 2013, *215*, 201−207.

CHAPTER V.

Conclusions and Future Outlooks

Conclusion

My study focused on the simple preparation of the mixed oxides at homogeneous mixing level by the facile and controllable solvothermal approach, and the application of the solvothemally prepared materials as catalyst supports. The achievements of the study are briefly summarized in two major points (Figure 5.1).

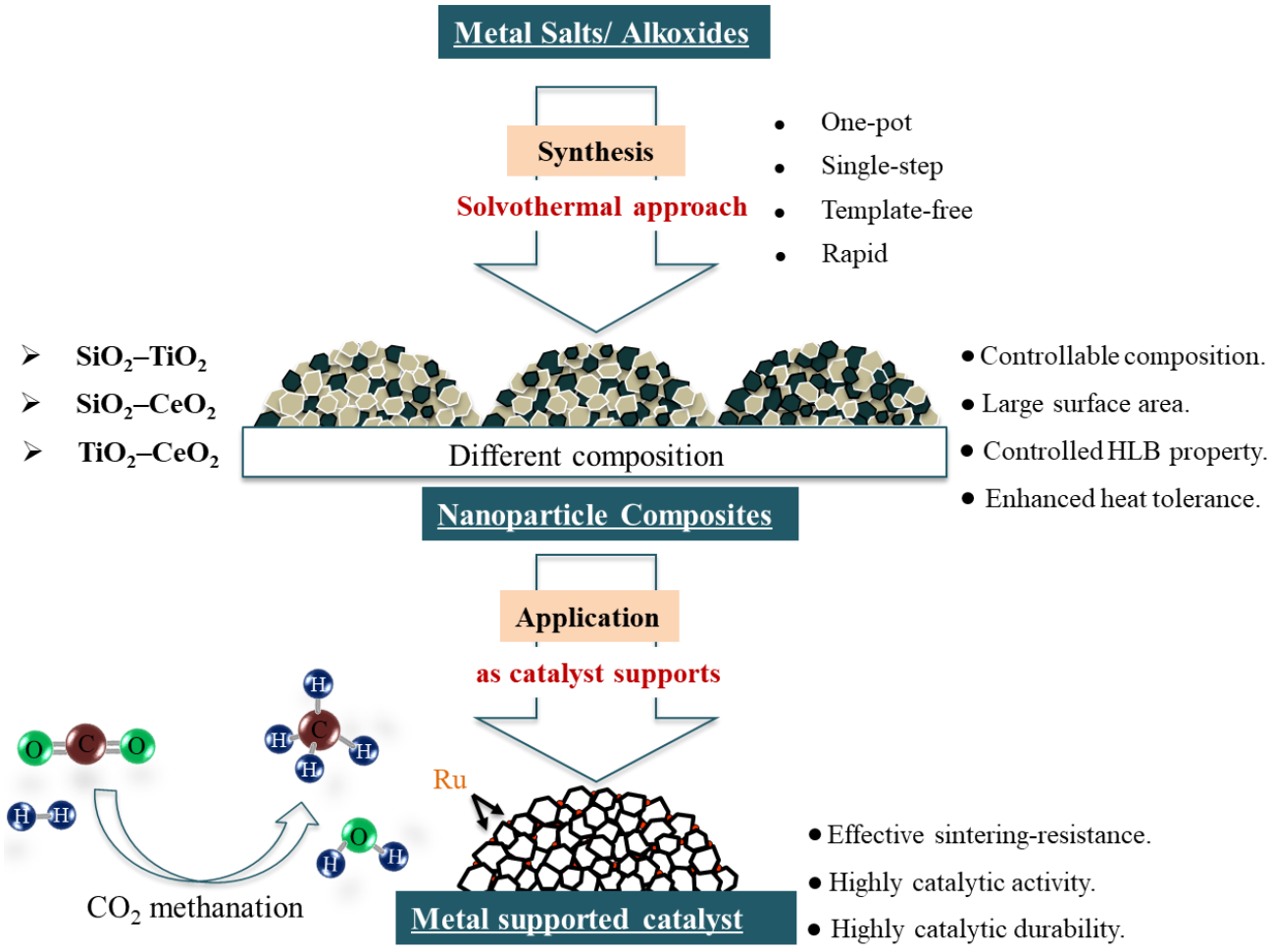

Figure 5.1. A summary of the research.

Synthesis of the mixed oxides:

- ✓ The facile one-pot and single-step solvothermal approach was successfully applied to prepare the homogeneously mixed assemblies of SiO_2–TiO_2, SiO_2–CeO_2, and TiO_2–CeO_2.
- ✓ The solvothermal reaction conditions were optimized appropriately by using the different additives.
- ✓ The chemical compositions of the prepared nanocomposites were effectively controlled by adjusting the precursor ratios in the precursor solutions.
- ✓ The obtained nanocomposite assemblies exhibited the expected properties of large specific surface area and high heat tolerance. In addition, the HLB control of the TiO_2 assemblies was simply modulated by using the functional silane coupling reagent as the precursor.

Application of the solvothermally prepared composites in catalysis:

- ✓ The prepared materials including CeO_2, SiO_2–CeO_2, and TiO_2–CeO_2 were used as supports for Ru catalysts.
- ✓ The well-dispersed Ru metal catalysts were deposited on the rough surface of the prepared nanocomposites by the precipitation-deposition method.
- ✓ Those Ru supported catalysts exhibited the higher catalytic activity for extremely exothermic CO_2 methanation as compared to the Ru catalyst deposited on the commercial-CeO_2.
- ✓ The sintering-resistant ability of CeO_2, SiO_2–CeO_2, and TiO_2–CeO_2 were confirmed by stable catalytic performance and almost remained catalyst state through the three-run test, long-term stability test, and ten-cycle test under severe conditions.

The combination of SiO_2 with the other oxides in nanoparticle assemblies has been recognized as relatively difficult because of their different crystal structures. However, this study provided the optimal solvothermal conditions to afford the mixed SiO_2–TiO_2 and SiO_2–CeO_2 with the high homogeneity, adjustable chemical compositions, HLB control, high heat tolerance, and large specific surface area. The solvothermally prepared nanocomposites presented high catalytic activity and the sinter-stable ability for exothermic CO_2 methanation at the elevated-temperature conditions.

Future Outlooks

As mentioned above, our solvothermal strategy is versatile to prepare various kinds of mono-component metal oxides as well as their nanocomposite assemblies. From successful preparation of the homogeneously mixed of SiO_2 assemblies, other designedly advanced materials are expected. Since a large-scale preparation of those prepared nanocomposites by autoclave was successfully performed, the industrial production of these materials is practicable. Also, the synthesized MARIMO assemblies with the advantages of the unique ultrafine nano convex/concave surface, huge surface area, and high heat tolerance are potential candidates for further catalytic applications.

LIST OF PUBLICATIONS

1. Hien Thi Thu Nguyen, Teppei Habu, Masataka Ohtani, Kazuya Kobiro, One-Step Direct Synthesis of SiO_2–TiO_2 Composite Nanoparticle Assemblies with Hollow Spherical Morphology, *Eur. J. Inorg. Chem.* **2017**, *2017,* 3017–3023.
2. Hien Thi Thu Nguyen, Masataka Ohtani, Kazuya Kobiro, One-pot synthesis of SiO_2–CeO_2 nanoparticle composites with enhanced heat tolerance, *Microporous Mesoporous Mat.* **2019**, *273,* 35−40.
3. Hien Thi Thu Nguyen, Yoshitaka Kumabe, Shigenori Ueda, Kai Kan, Masataka Ohtani, Kazuya Kobiro, Highly durable Ru catalysts supported on CeO_2 nanocomposites for CO_2 methanation, submitted.

International Conference

1. Hien Thi Thu Nguyen, Masataka Ohtani, and Kazuya Kobiro, "One-Step Direct Synthesis of SiO_2–TiO_2 Composite Nanoparticle Assemblies with Hollow Spherical Morphology", The 17th Asian Pacific Confederation of Chemical Engineering, August 2017, Hong Kong (Poster).
2. Hien Thi Thu Nguyen, Masataka Ohtani, and Kazuya Kobiro, "Direct Fabrication of SiO_2–TiO_2 Spherical Nanocomposites with Hollow Cavity and Porous Shell", The 6th International Symposium on Frontier Technology, November 2017, Kochi University of Technology, Japan (Oral).
3. Hien Thi Thu Nguyen, Masataka Ohtani, and Kazuya Kobiro, "Simple Fabrication with Excellent Control of Hollow Spherical SiO_2–TiO_2 Composite Nanomaterials", The 10th International Conference on Supercritical Fluids, December 2017, Nagoya, Japan (Oral).
4. Hien Thi Thu Nguyen, Masataka Ohtani, and Kazuya Kobiro, "A Facile Solvothermal

Strategy for Designed Silica Nanocomposites", The 6th International Solvothermal Hydrothermal Association Conference, August 2018, Sendai, Japan (Oral).

5. Hien Thi Thu Nguyen, Masataka Ohtani, and Kazuya Kobiro, "Simple Solvothermal Preparation of Silica-Ceria Nanocomposite", The 6th International Solvothermal Hydrothermal Association Conference, August 2018, Sendai, Japan (Poster).

Domestic conferences and symposiums

1. Hien Thi Thu Nguyen, Teppei Habu, Yuna Umemoto, Yukino Masaoka, Masataka Ohtani, and Kazuya Kobiro, "Synthesis of MARIMO TiO_2/SiO_2 assemblies and their surface modification", The Chemical Society of Kochi, August 2016, Kochi University (Poster).
2. Hien Thi Thu Nguyen, Masataka Ohtani, and Kazuya Kobiro, Nanotechnology Symposium, November 2016, Kochi University of Technology (Poster).
3. Hien Thi Thu Nguyen, Teppei Habu, Yuna Umemoto, Yukino Masaoka, Masataka Ohtani, and Kazuya Kobiro, "Synthesis of hollow spherical titania-silica composite nanoparticle assemblies with controllable composition and their surface modification", The 97th CSJ Annual Meeting, March 2017, Yokohama, Japan (Oral).
4. Hien Thi Thu Nguyen, Masataka Ohtani, and Kazuya Kobiro, "Easy Preparation of Submicron Size Silica–TitaniaComposite Porous Spheres with Hollow Morphology", 第 11 回触媒道場**,** September 2017, Kochi, Japan (Poster).
5. Hien Thi Thu Nguyen, Masataka Ohtani, and Kazuya Kobiro, "Fabrication of Ceria Nanoparticle Assemblies by One-step Solvothermal Method", Nanotechnology Symposium, November 2017, Kochi University of Technology (Poster).
6. Hien Thi Thu Nguyen, Masataka Ohtani, and Kazuya Kobiro, "A new approach to higher heat tolerance of CeO_2 nanoparticles by mixing with SiO_2 in nano-level through one-pot

solvothermal method", The 98th CSJ Annual Meeting, March 2018, Chiba, Japan (Oral).

7. Hien Thi Thu Nguyen, Masataka Ohtani, and Kazuya Kobiro, "A facile solvothermal synthesis of Ceria nanocomposites", The Chemical Society of Kochi, October 2018, Kochi University of Technology (Poster).
8. Hien Thi Thu Nguyen, Ryochiro Sakamoto, Kai Kan, Masataka Ohtani, and Kazuya Kobiro, A simple preparation of nano-sized Ceria composites, Nanosymposium, November 2018, Kochi University of Technology (Poster).

Awards

1. Poster Award 2017, Hien Thi Thu Nguyen, Masataka Ohtani, and Kazuya Kobiro, "Easy Preparation of Submicron Size Silica–Titania Composite Porous Spheres with Hollow Morphology", *第11回触媒道場,* September 2017, Kochi, Japan.
2. Graduate Student Award 2018, Hien Thi Thu Nguyen, Masataka Ohtani, and Kazuya Kobiro, "Simple Solvothermal Preparation of Silica-Ceria Nanocomposite", The 6th International Solvothermal Hydrothermal Association Conference, August 2018, Sendai, Japan.

ACKNOWLEDGEMENT

Firstly, I would like to express my sincere gratitude to my advisor Prof. Kobiro who has dedicatedly guided and supported my Ph.D research. He inspired me to believe in myself and to learn new things in all the time of research. Besides that, I am deeply grateful for his encouragement in difficult moments.

I am particularly grateful to Associate Prof. Ohtani for giving me the invaluable advices, for enlightening me the research, and for encouraging me to reach my goal.

Besides my advisor, I would like to thank my thesis committee: Prof. Sugimoto, Prof. Nishiwaki, and Prof. Makino whose insightful comments and questions helped me to widen my research from various prospects.

My sincere appreciations also go to my lab-mates who have supported generously me for my research. I also thank them for taking care of me and for sharing with me all the fun moments during last three years. I am so grateful to the university staffs for their dedicated supports and helps.

Many thanks to all of my friends, both Vietnamese friends and foreign friends, who have supported me in doing the research, shared life with me, and cheered me up during my three-year in Kochi.

And finally, last but not the least, a special thanks to my beloved family. Nothing can fully express how grateful I am to my parents and my two brothers for all of the love, sacrifices and supports in my life.

Thanks for your all supports and encouragements.

APPENDICES

Appendix 1 (Chapter II)

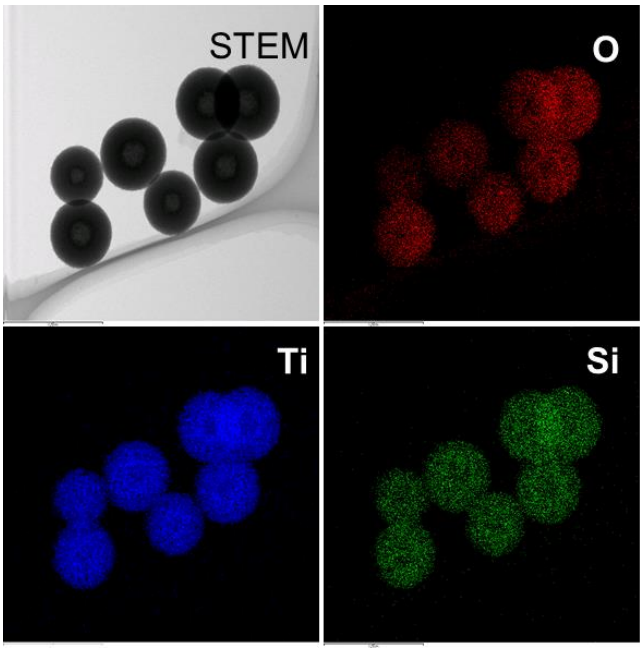

Figure A1.1. STEM image and EDX mappings of SiO_2–TiO_2 NP assemblies at Si mole fraction of 0.5.

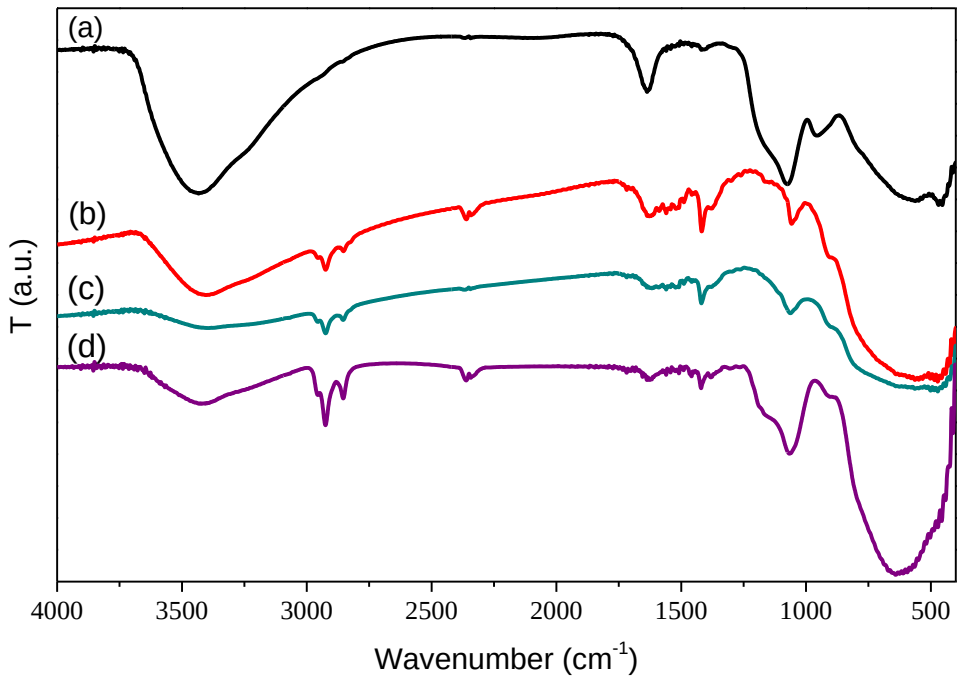

Figure A1.2. IR spectra of (a) SiO_2–TiO_2 NP assemblies and *n*-octyl-SiO_2–TiO_2 NP assemblies synthesized at (b) 300 ^{0}C, (c) 350 ^{0}C, and (d) 400 ^{0}C.

Appendix 2 (Chapter III)

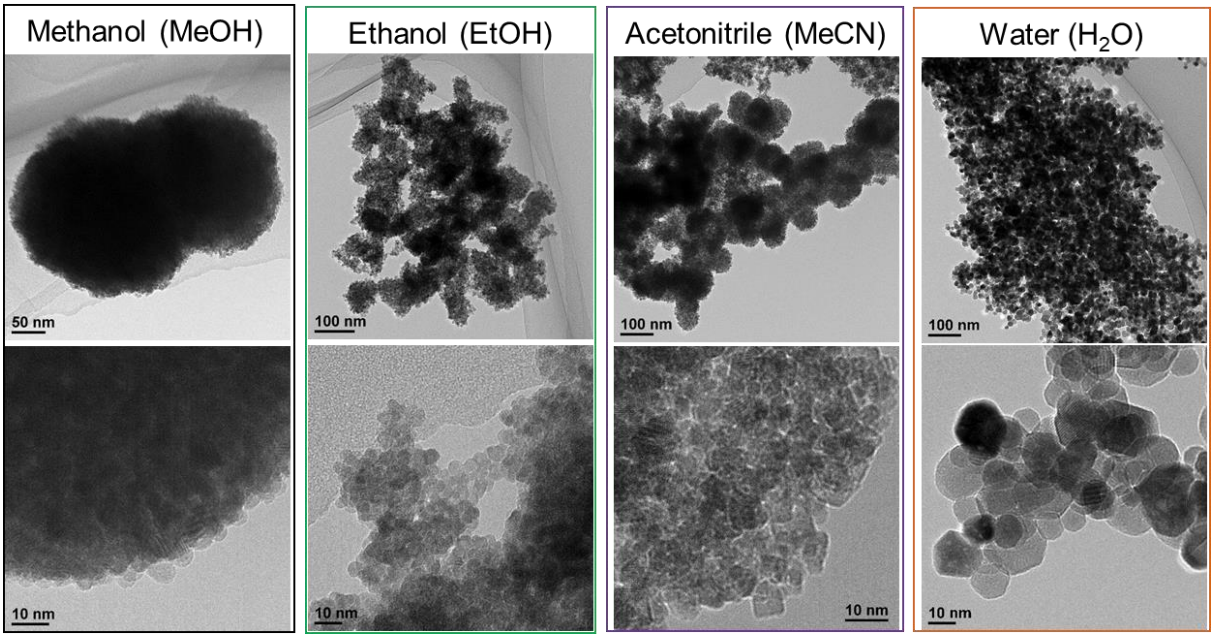

Figure A2.1. TEM images of CeO_2 NP assemblies synthesized at 300 °C for 10 min using *N,N,N',N'*-tetramethylethylenediamine (TMEDA) as additive in different solvents of methanol (MeOH), ethanol (EtOH), acetonitrile (MeCN), and water (H_2O).

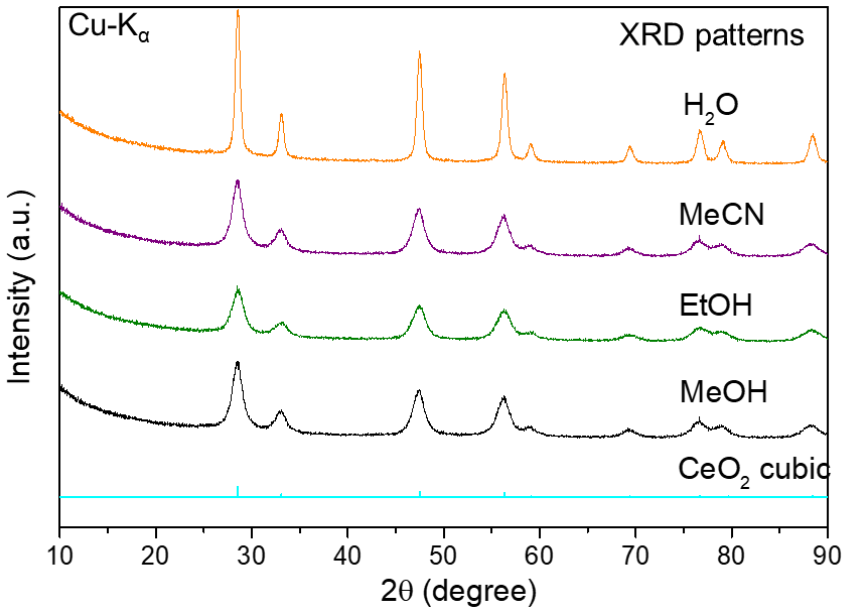

Figure A2.2. XRD patterns of CeO_2 NP assemblies synthesized using *N,N,N',N'*-tetramethylethylenediamine (TMEDA) as amine additive in different solvents.

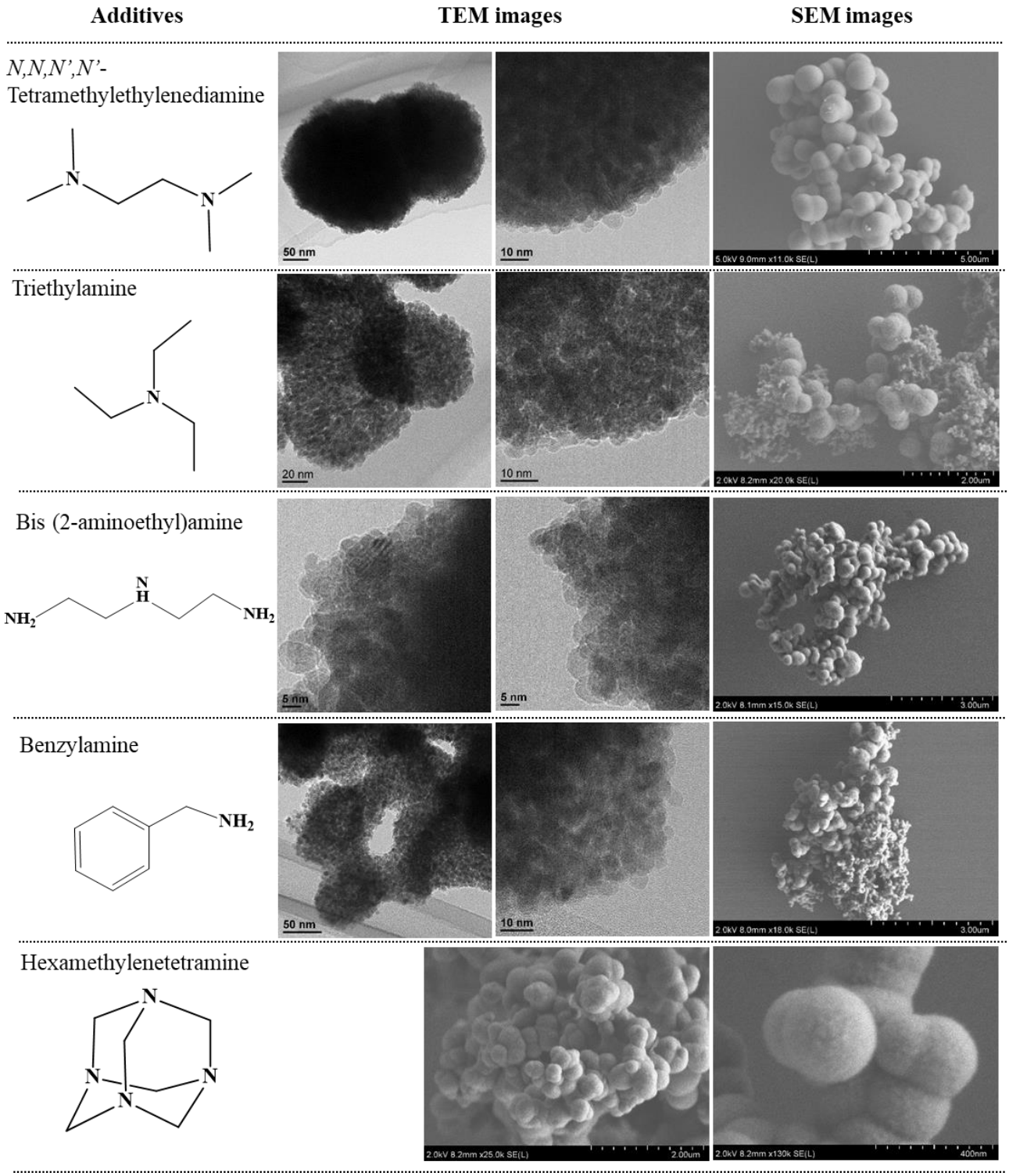

Figure A2.3. TEM and SEM images of CeO_2 NP assemblies synthesized using different kinds of amines in methanol.

Appendix 3 (Chapter IV)

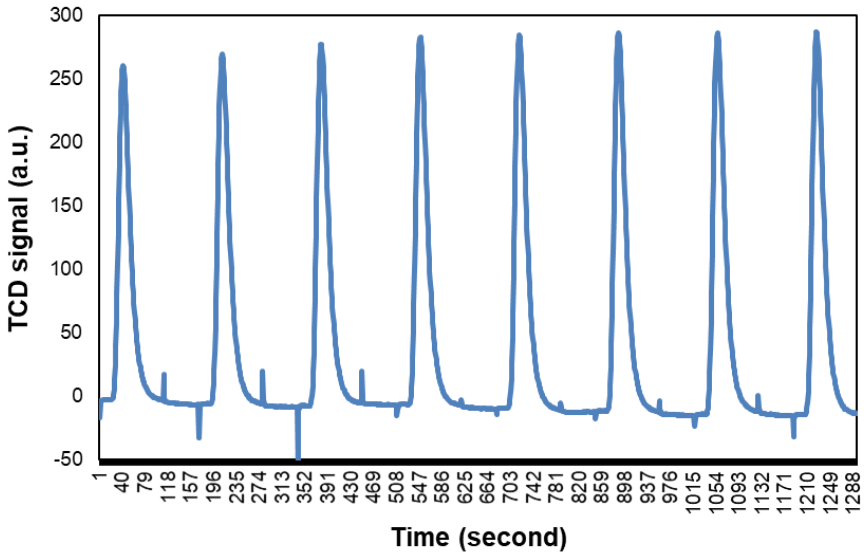

Figure A3.1. CO chemical adsoptions of the prepared CeO_2 support.

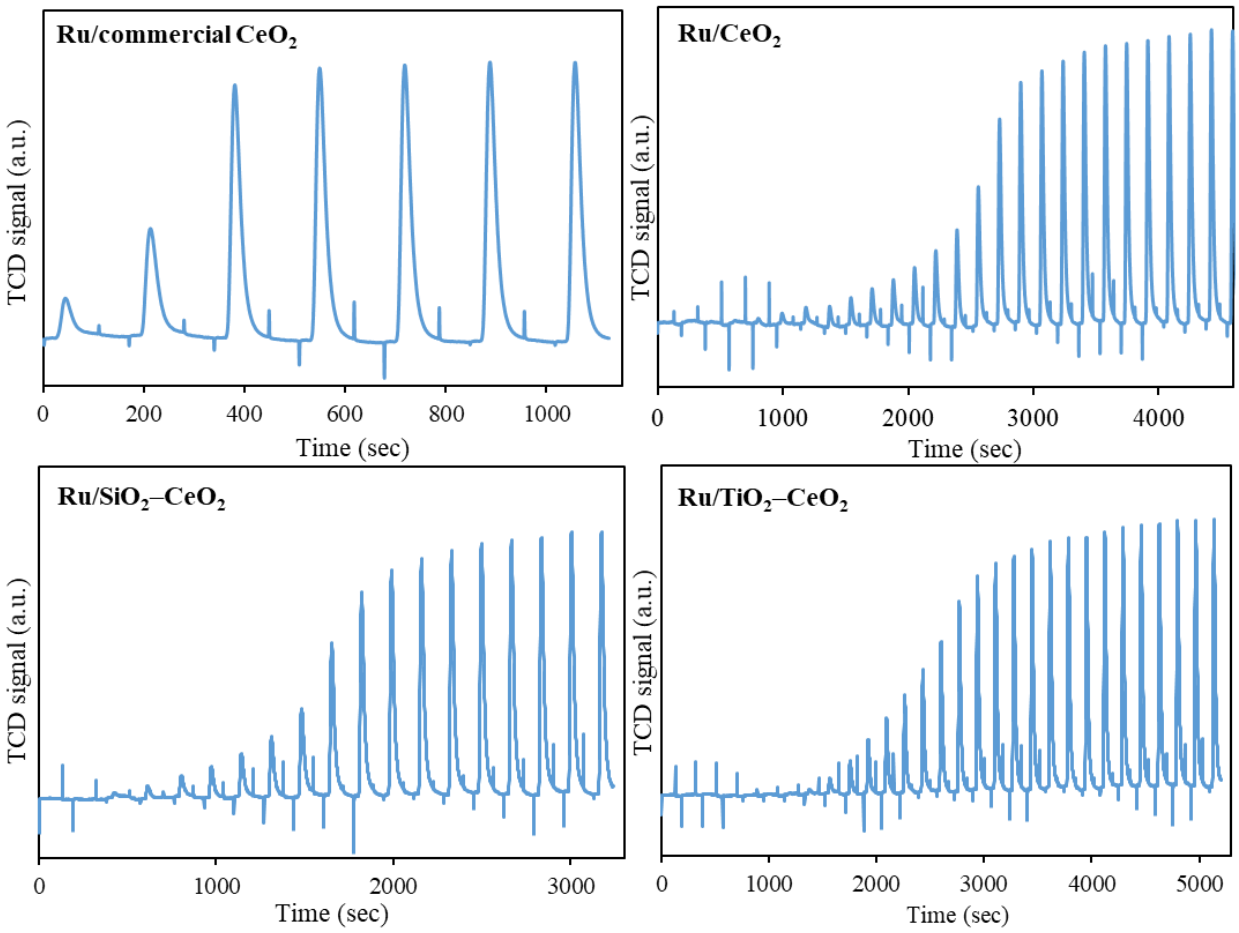

Figure A3.2. CO chemical adsoptions of the prepared catalysts.

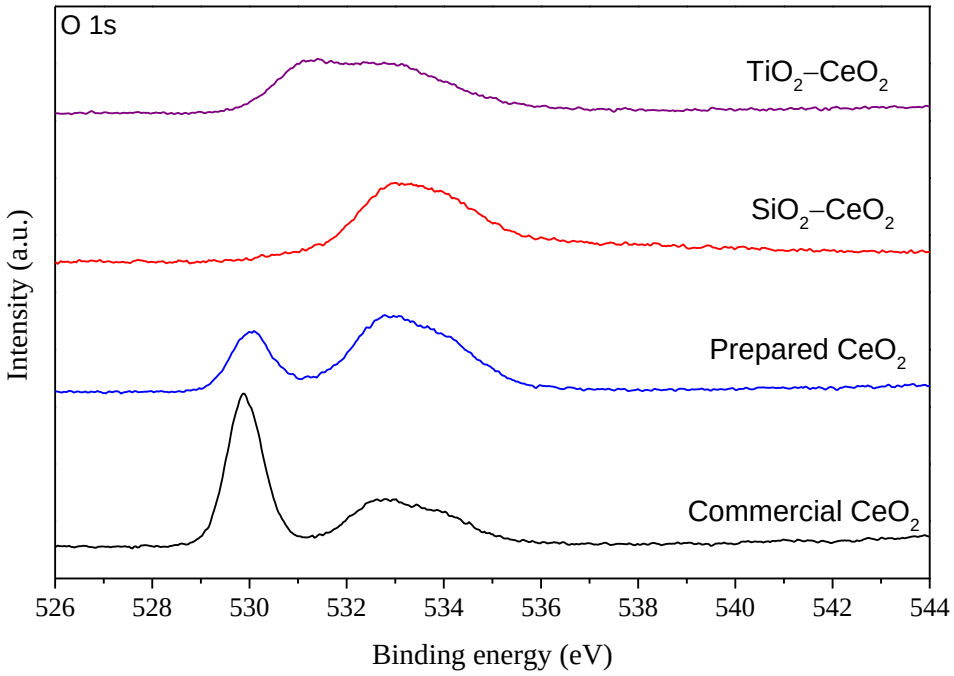

Figure A3.3. HAXPES O1s spectra of the supports.

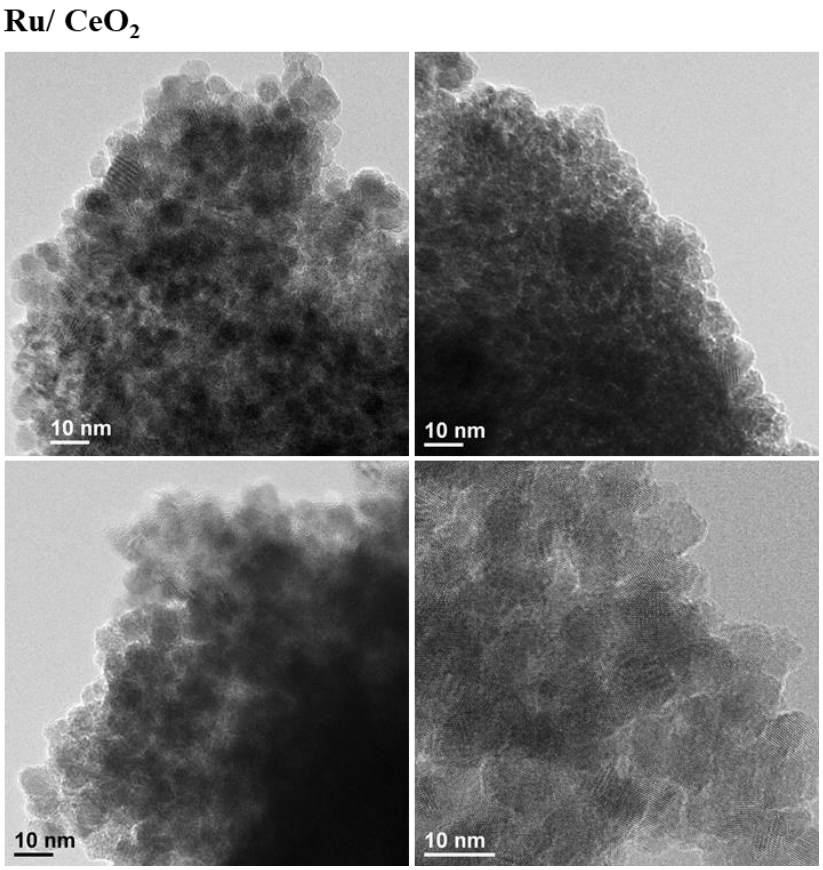

Figure A3.4. TEM images of the Ru/CeO_2 catalyst.

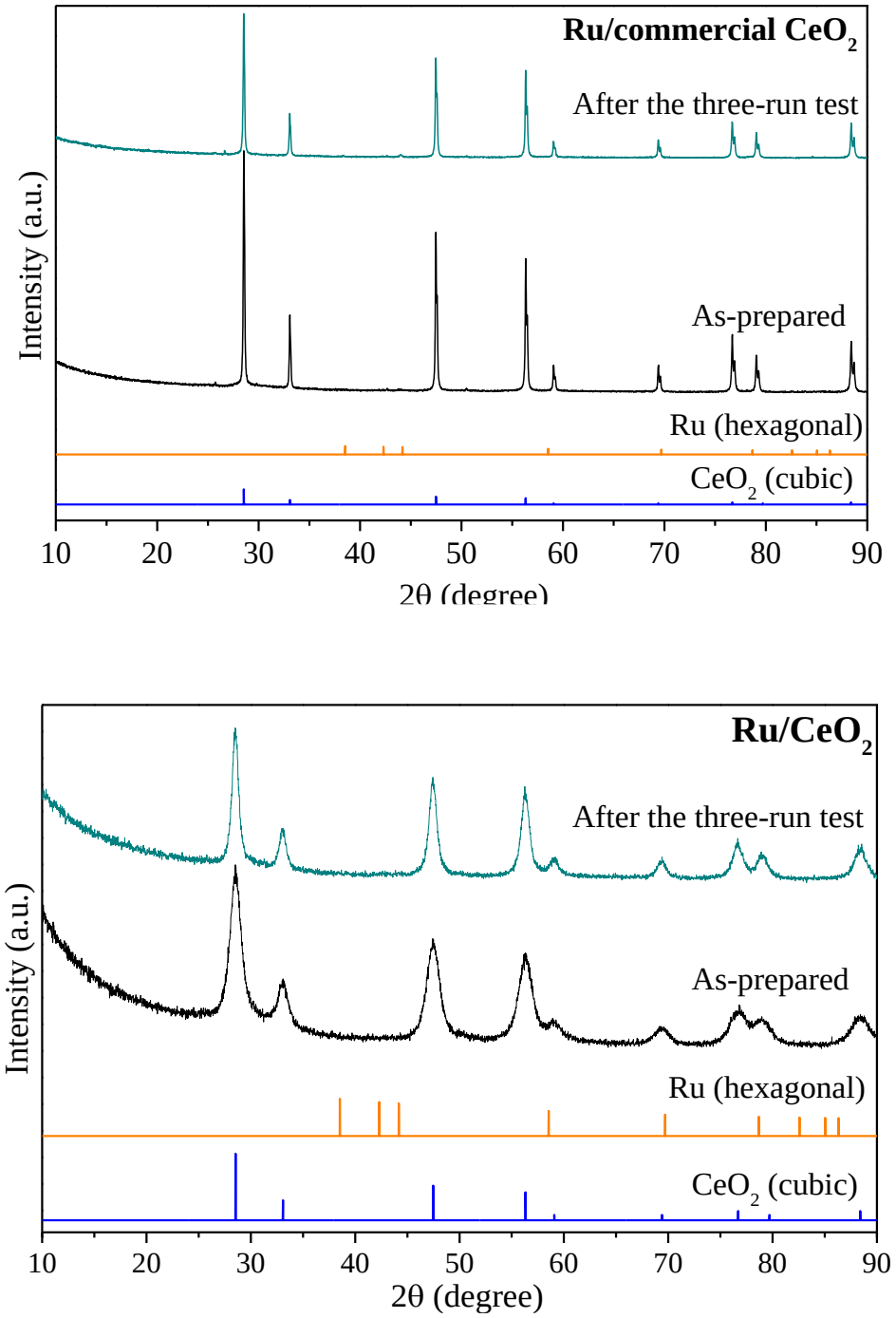

Figure A3.5. XRD spectra of the Ru/commercial CeO_2 and Ru/CeO_2 before and after the three-run test.

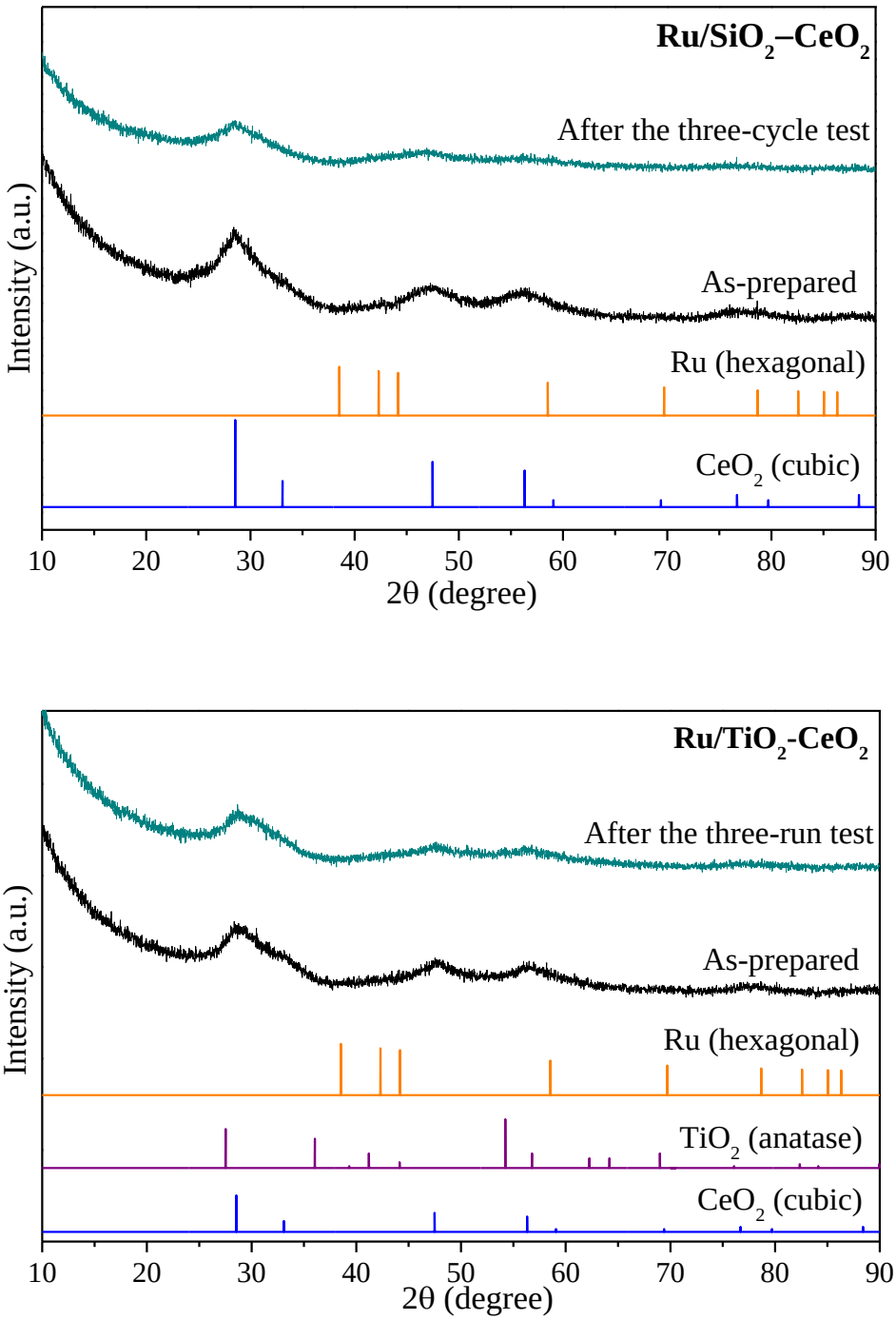

Figure A3.6. XRD spectra of the Ru catalysts on prepared composite supports before and after the three-run test.

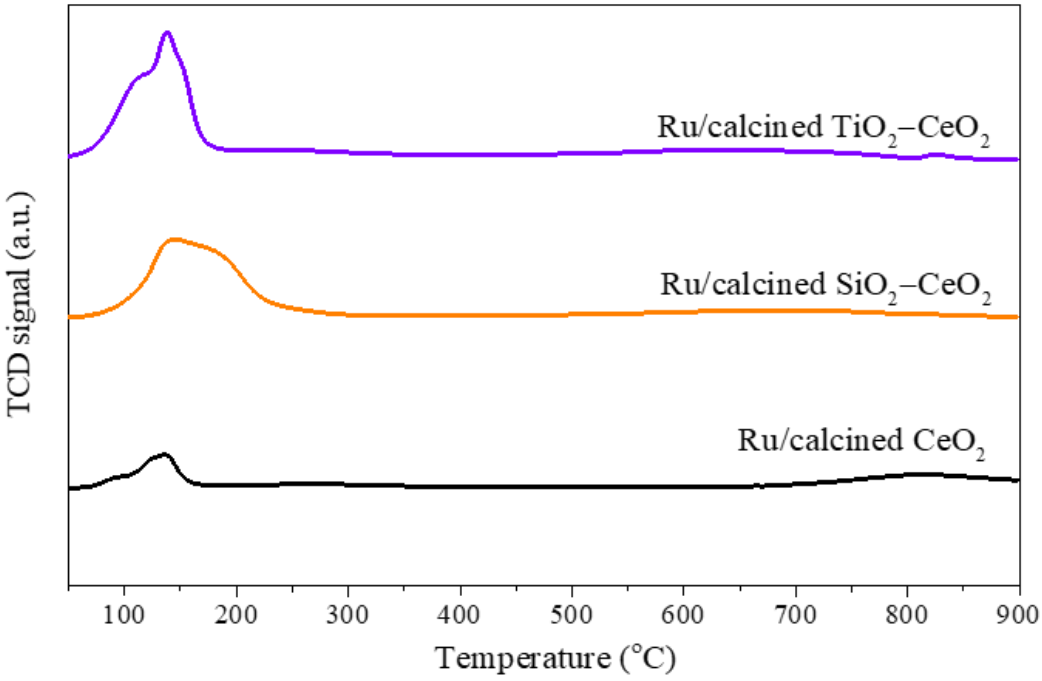

Figure A3.7. H_2-TPR profiles of the Ru supported catalysts on the calcined supports.

Table A3.1. H_2 consumptions during the H_2-TPR experiments over the Ru catalysts on calcined supports.

Catalysts	H_2 uptake (mmol/g) in temperature range of 50 – 250 (°C)
Ru/calcined CeO_2	0.49[a]
Ru/calcined SiO_2–CeO_2	2.49[a]
Ru/calcined TiO_2–CeO_2	2.20[a]

[a] Theoretical H_2 uptake for reduction of RuO_2 to metallic Ru^0 is 0.59 mmol/g catalyst.

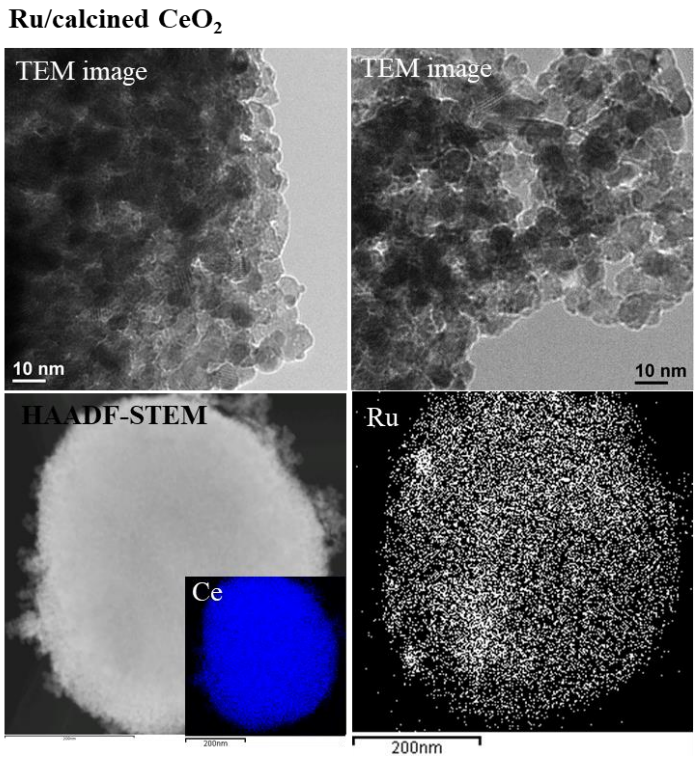

Figure A3.8. TEM images, HAADF-STEM images, and EDX mappings of Ce, Si, and Ru elements of the catalysts.

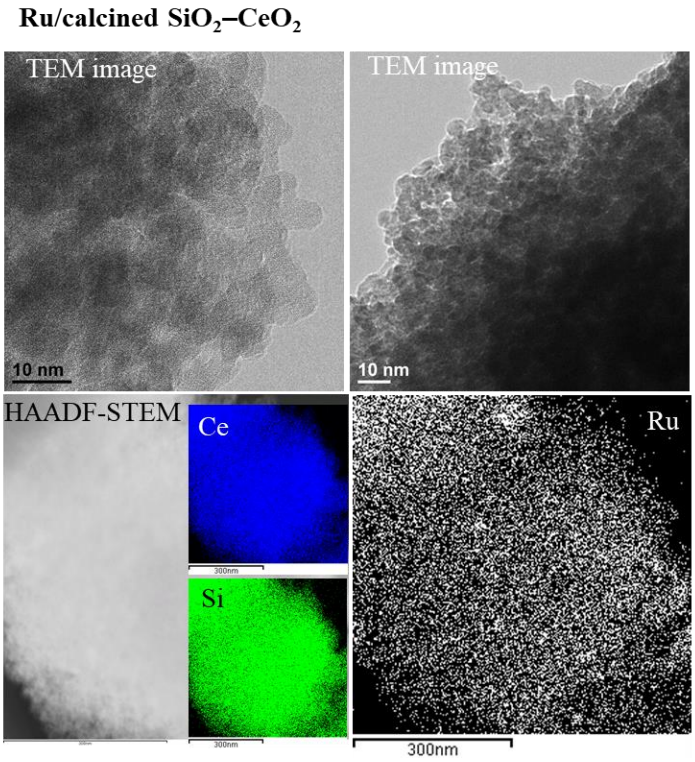

Figure A3.9. TEM images, HAADF-STEM images, and EDX mappings of Ce, Si, and Ru elements of the catalysts.

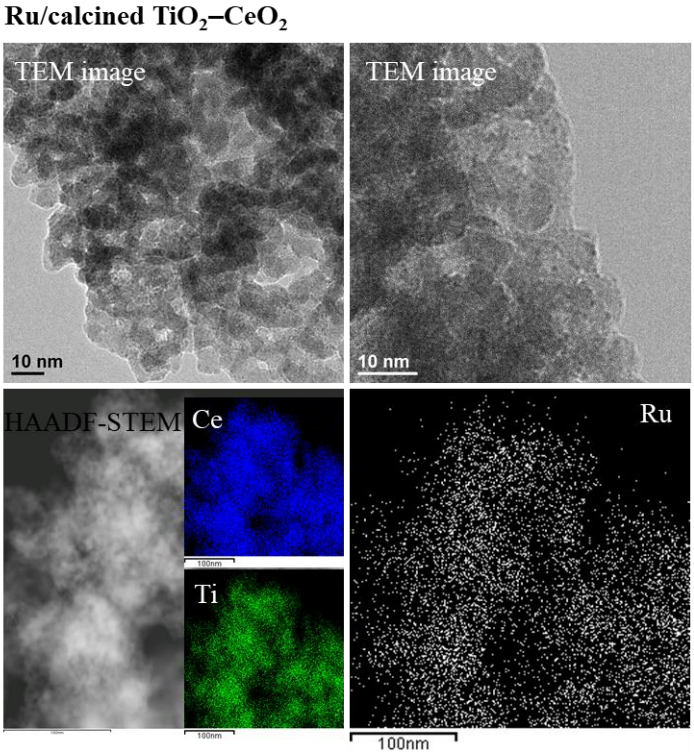

Figure A3.10. TEM images, HAADF-STEM images, and EDX mappings of Ce, Si, and Ru elements of the catalysts.

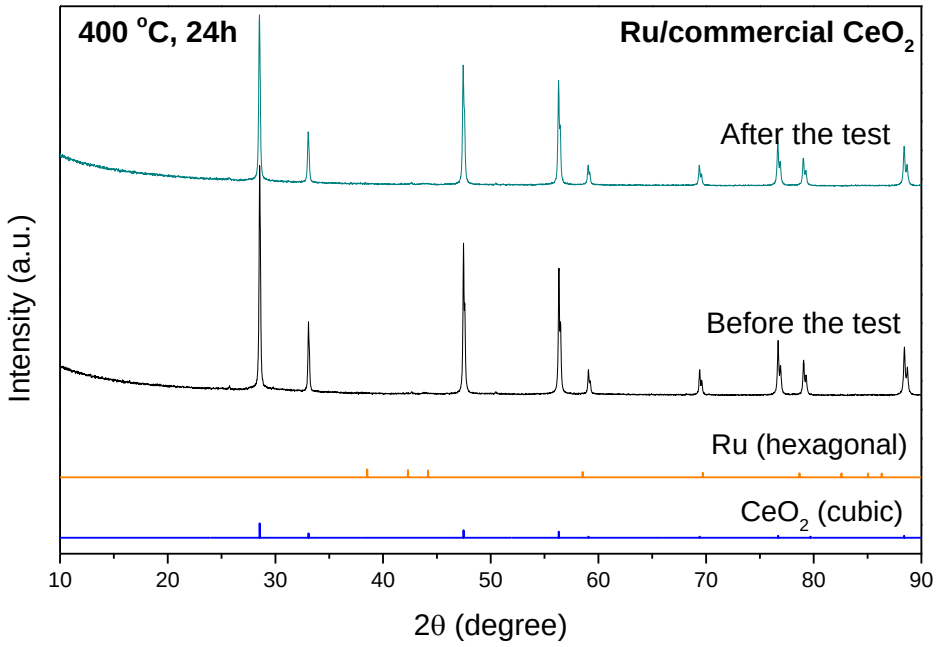

Figure A3.11. XRD spectra of the Ru/commercial CeO_2 before and after the long-term stability test at 400 °C for 24 h.

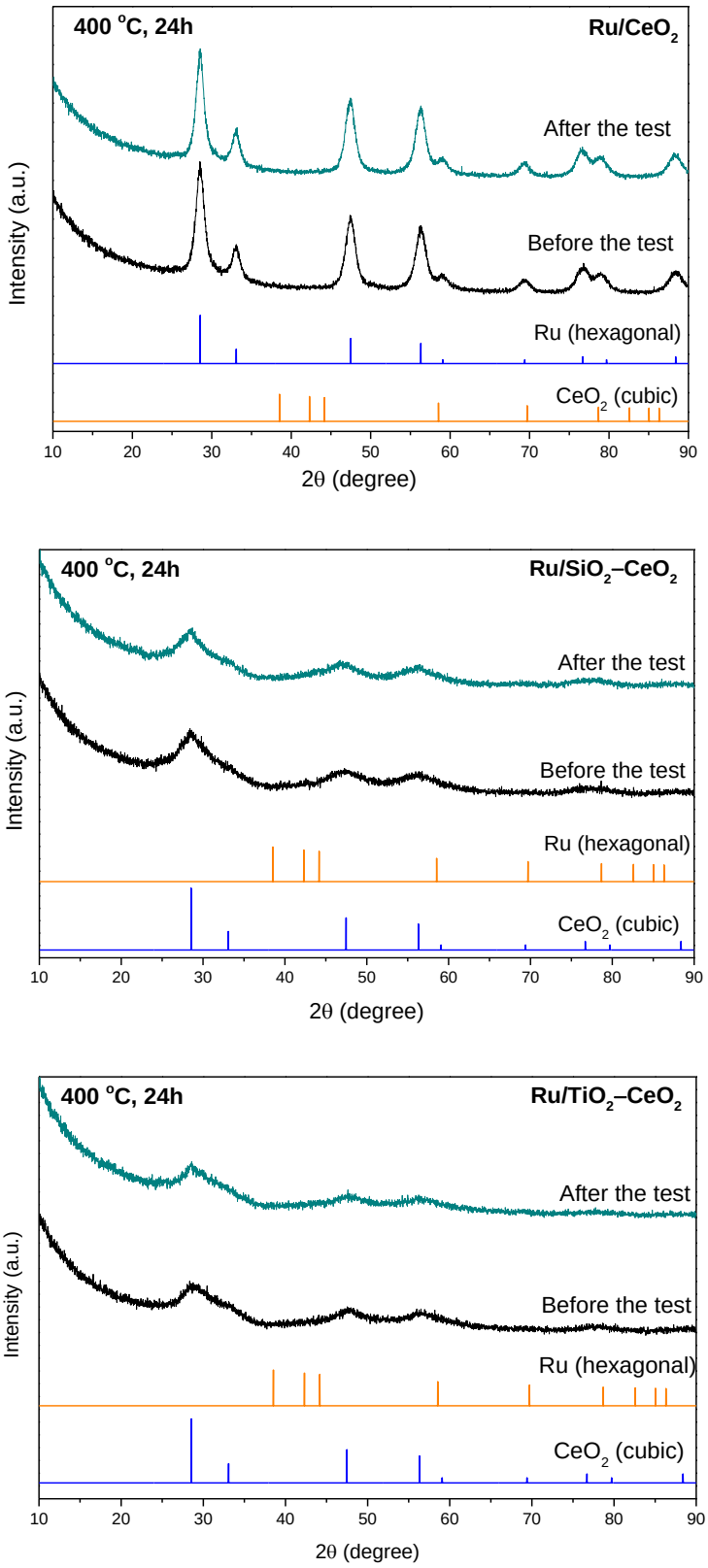

Figure A3.12. XRD spectra of the Ru catalysts on the prepared supports before and after the long-term stability test at 400 °C for 24 h.

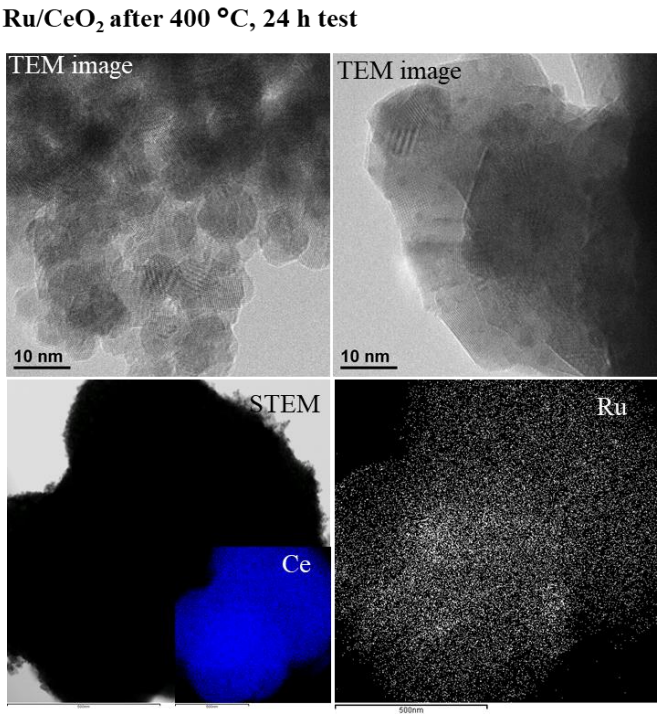

Figure A3.13. TEM images, HAADF-STEM images, and EDX mappings of Ru/CeO_2 after the long-term stability test.

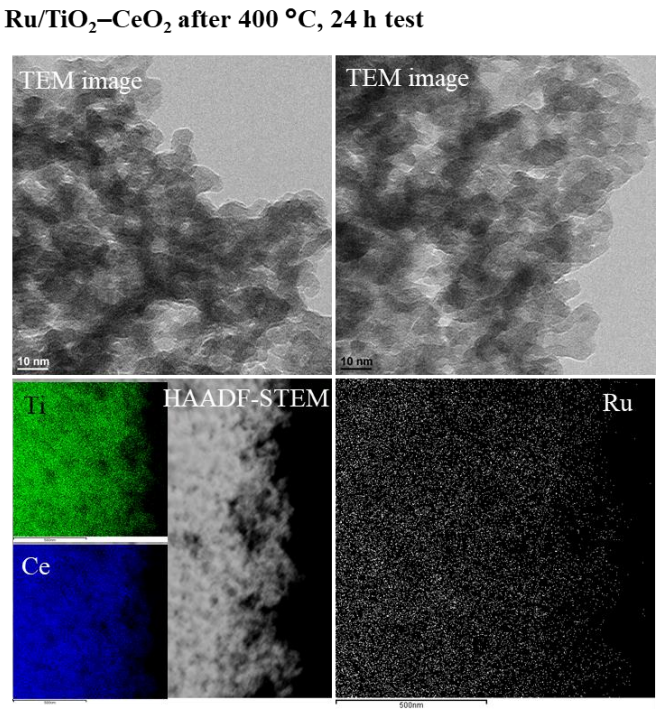

Figure A3.14. TEM images, HAADF-STEM images, and EDX mappings of $Ru/TiO_2–CeO_2$ after the long-term stability test.

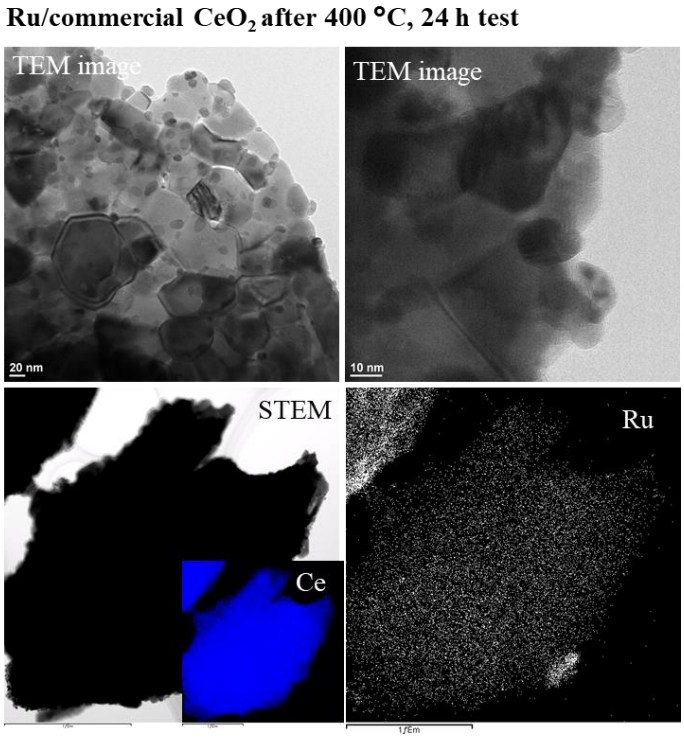

Figure A3.15. TEM images, HAADF-STEM images, and EDX mappings of Ru/commercial CeO_2 after the long-term stability test.

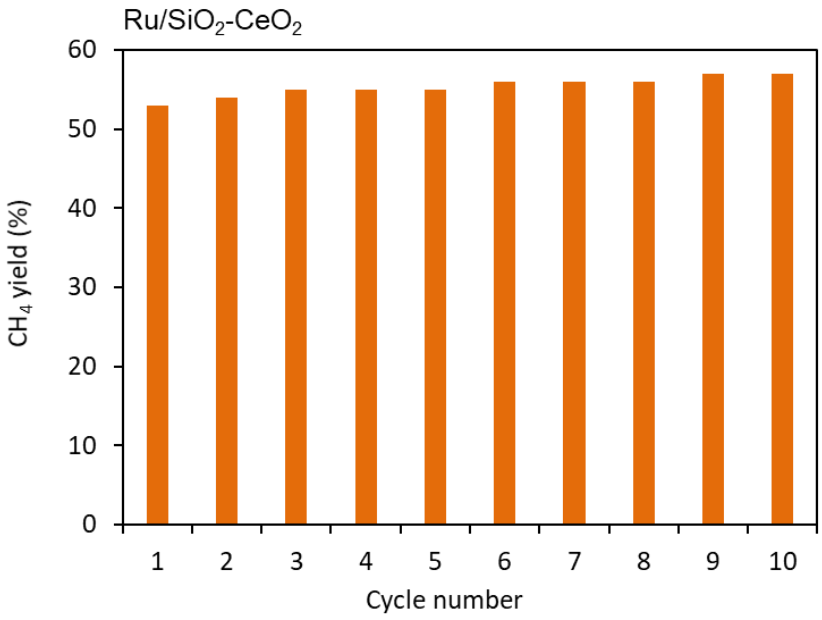

Figure A3.16. CH_4 yield for CO_2 methanation over Ru/SiO_2–CeO_2 in 10-cycle test at 50 °C and 300 °C (graph represents only the results at 300 °C). The reaction time at each temperature was kept at 30 min and the total gas flow was 20 mL/min (5% CO_2, 20% H_2, and 75% Ar).

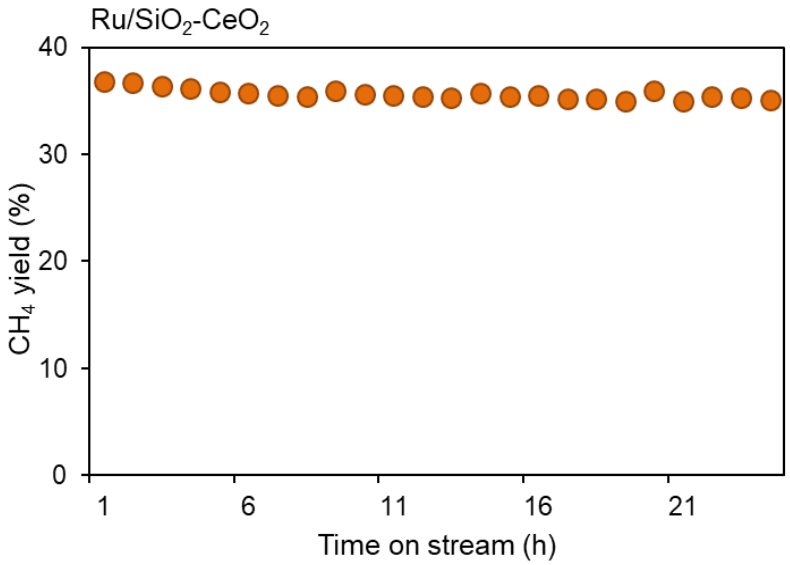

Figure A3.17. CH_4 yield for CO_2 methanation over $Ru/SiO_2–CeO_2$ in the long-term stability test. The total gas flow was 20 mL/min (5% CO_2, 20% H_2, and 75% Ar). The amount of catalyst of 25 mg was used in the experiment.

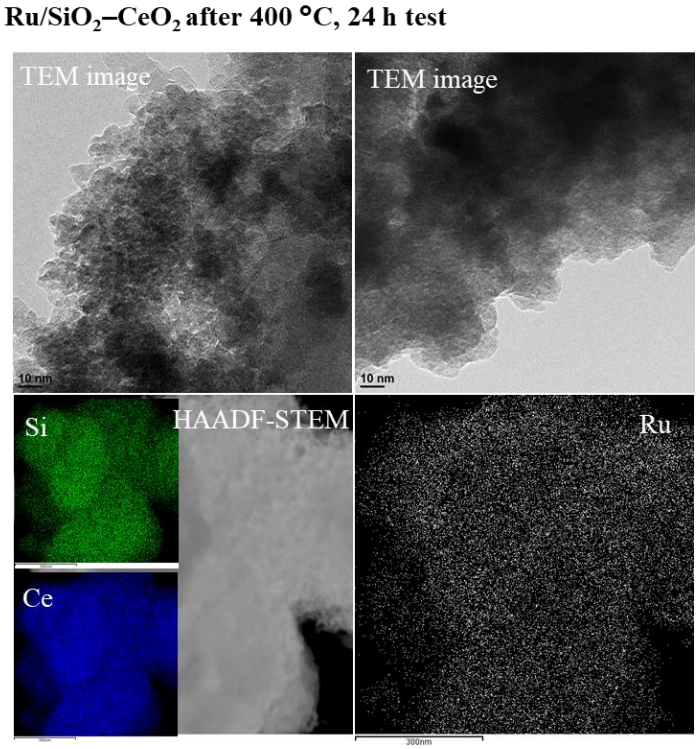

Figure A3.18. TEM images, HAADF-STEM images, and EDX mappings elements of $Ru/SiO_2–CeO_2$ after the long-term stability test.

Table SA.2. Turnover frequency (TOF) for the Ru catalysts at different reaction temperatures.

Catalysts	TOF (s^{-1}) at different temperatures		
	150 °C	200 °C	250 °C
Ru/commercial CeO_2	0	2.9×10^{-2}	9.9×10^{-2}
Ru/CeO_2	0	1.6×10^{-3}	1.7×10^{-2}
Ru/SiO_2–CeO_2	0	0	1.0×10^{-2}
Ru/TiO_2–CeO_2	0	9.0×10^{-4}	1.8×10^{-2}
Ru/calcined CeO_2	0	4.7×10^{-3}	2.0×10^{-2}
Ru/calcined TiO_2–CeO_2	6.0×10^{-4}	8.2×10^{-3}	2.5×10^{-2}

Calculation of TOF (s^{-1}), referred from reference [1], was given:

$$\text{TOF } (s^{-1}) = \frac{F_{CO2} X_{CH4} M}{WDx}$$

where F_{CO_2} : mole number of CO_2 at reaction temperature per unit time (mol s^{-1}).

X_{CH_4} : proportion of CH_4 molecules in the outflow.

M: atomic mass of Ru (101.07 g/mol).

D: Ru dispersion of Ru on the support.

W: weight of catalyst (g).

x: loading amount of Ru (quantified by STEM/EDX analysis).

Reference

[1] Y. Guo, S. Mei, K. Yuan, D.J. Wang, H.C. Liu, C.H. Yan, Y.W. Zang, *ACS Catal.* **2018**, *8*, 6203–6215.